Western Graduate&PostdoctoralStudies

Western University

Scholarship@Western

Electronic Thesis and Dissertation Repository

12-1-2016 12:00 AM

Development and Optimization of 19F-MRI for Tracking Cellular Therapeutics

Jeffrey M. Gaudet
The University of Western Ontario

Supervisor
Paula J. Foster
The University of Western Ontario

Graduate Program in Medical Biophysics
A thesis submitted in partial fulfillment of the requirements for the degree in Doctor of Philosophy
© Jeffrey M. Gaudet 2016

Follow this and additional works at: https://ir.lib.uwo.ca/etd

Part of the Other Analytical, Diagnostic and Therapeutic Techniques and Equipment Commons

Recommended Citation

Gaudet, Jeffrey M., "Development and Optimization of 19F-MRI for Tracking Cellular Therapeutics" (2016). *Electronic Thesis and Dissertation Repository*. 4250.
https://ir.lib.uwo.ca/etd/4250

This Dissertation/Thesis is brought to you for free and open access by Scholarship@Western. It has been accepted for inclusion in Electronic Thesis and Dissertation Repository by an authorized administrator of Scholarship@Western. For more information, please contact wlswadmin@uwo.ca.

Abstract

Introduction: This thesis aims to advance magnetic resonance imaging (MRI) for imaging cellular therapeutics. Traditional, proton-based, MRI provides detailed anatomical images, particularly of soft tissue. However, in order to obtain information at a cellular level specialized imaging agents are required to detect the cells of interest. Perfluorocarbons containing non-radioactive fluorine-19 (^{19}F) are both biologically safe and MR sensitive. **Methods:** Pre-clinical ^{19}F-MRI was implemented on a Varian 9.4T MRI scanner, using a dual ^{19}F/^{1}H-tuned birdcage volume coil. Mesenchymal stromal cells (MSC) were pre-labeled with a commercial, FDA approved ^{19}F-perfluorocarbon emulsion, then implanted intramuscularly into the mouse hindlimb. To track the inflammation resulting from transplantation, a dual-agent cellular MRI technique was developed. This technique utilizes ^{19}F to track MSC and superparamagnetic iron oxide nanoparticles (SPIO) to image macrophages, through signal quenching. A clinical imaging protocol was developed to translate ^{19}F-MRI to a 3T GE MR750 scanner with a dual ^{19}F/^{1}H-tuned surface coil. Peripheral blood mononuclear cells (PBMC) were labeled with a FDA-approved ^{19}F-agent and injected into a ham shank phantom for protocol optimization. **Results:** The balanced steady-state free precession pulse sequence was chosen for all studies due to the high signal-to-noise per unit time. Image acquisition was optimized for ^{19}F detection sensitivity, accuracy of quantification, and compatibility with isoflurane. *In vivo* quantification of MSC on the day of implantation was in strong agreement with the expected number of cells. The change in ^{19}F-signal was quantified over time and compared between two murine transplantation models. When iron oxide was administered *i.v.,* the migration of immune cells could be tracked to the injection site. The presence of SPIO decreased both the ^{1}H and ^{19}F signal, indicating that transplant rejection was occurring. On a clinical system, as few as 4×10^6 PBMC could be imaged following both surface and subcutaneous injection. The minimum number of detectable cells was strongly influenced by intracellular ^{19}F uptake. **Conclusions:** ^{19}F-MRI is a promising tool for imaging cellular therapeutics. By pre-labeling cells of interest, they can be localized and the change in signal can be quantified over time. The technique shows promise for both pre-clinical and clinical applications.

Keywords

MRI, fluorine-19, cell tracking, cellular MRI, mice, super paramagnetic iron oxide (SPIO), bSSFP, cellular therapy, mesenchymal stem cells (MSC), transplant rejection, peripheral blood mononuclear cells (PBMC)

Co-Authorship Statement

Chapter 1 contains material from 2 previously published review papers. AV Makela*, DH Murrell*, KM Parkins, J Kara, JM Gaudet and PJ Foster (2016) *Cellular Imaging with MRI* published in Topics in Magnetic Resonance Imaging, 25(5): 177-186. AVM, DHM, KMP, JK, JMG, PJF contributed to drafting of the manuscript. AVM, DHM, and PJF edited the manuscript. The second review, MS Fox, JM Gaudet and PJ Foster (2015) *Fluorine-19 MRI Contrast Agents for Cell Tracking and Lung Imaging* published in Magnetic Resonance Insight 8(S1):1-15. MSF drafted the manuscript with JMG and PJF contributing sections. MSF, JMG, and PJF edited the manuscript.

Chapter 2 contains previously unpublished data. JM Gaudet participated in experimental design, data collection and analysis and drafted the chapter. PJ Foster contributed to experimental design and chapter editing.

Chapter 3 is reprinted from: JM Gaudet, EJ Ribot, Y Chen, KM Gilbert, and PJ Foster (2015) *Mesenchymal stem cell transplant rejection monitored with ^{19}F-MRI* published in PLoS ONE 10(3): e0118544. JMG participated in experimental design, data collection and analysis, and drafted the manuscript. YC performed cell culture, histology and immunohistochemistry. KMG designed and manufactured hardware for the study. EJR and PJF contributed to experimental design and manuscript preparation.

Chapter 4 is reprinted from: JM Gaudet, A Hamilton, Y Chen, MS Fox, and PJ Foster (2016) *Application of dual ^{19}F and iron cellular MRI agents to track the infiltration of immune cells to a site of a rejected stem cell transplant* published in Journal of Magnetic Resonance in Medicine, Early view. JMG participated in experimental design, data collection and analysis, and drafted the manuscript. AH performed cell culture. AH and YC performed histology and immunohistochemistry. MSF and PJF contributed to experimental design and manuscript preparation.

Chapter 5 contains sections from a paper currently under review at PLoS ONE: C Fink, JM Gaudet, MS Fox, S Bhatt, S Viswanathan, M Smith, J Chin, PJ Foster, and GA Dekaban. *^{19}F-perfluorocarbon-labeled human peripheral blood mononuclear cells can be detected in vivo using clinical MRI parameters in a therapeutic cell setting*. CF, JMG carried out experiments and data analysis, participated in study design, and drafted the manuscript. CF & MS performed all cell work, safety testing, and animal handling. JMG performed all 9.4T imaging, and along with MSF developed 3T imaging protocols. SB, SV, JC, PJF, and GAD contributed to experimental design and writing the manuscript.

Acknowledgments

To my supervisor, Dr. Paula Foster, thank you for everything you've taught me and for making these last four years so enjoyable. Whether it was providing me opportunities to present around the world or introducing me to your peers, you've consistently gone above and beyond to mentor me. I can't imagine a better supervisor.

I'd like to thank all the members, past and present, of the Foster lab for their help and friendship over the past four years. I'd especially like to thank the post-doctoral fellows, Drs. Amanda Hamilton, Emeline Ribot, and Matthew Fox. Without their expertise and guidance fluorine-MRI wouldn't be where it is today at Robarts.

To Dr. Donna Murrell - we started on the same day and went through each step of grad school together. It's been amazing to always have someone to work through problems with and bounce ideas off of. From the late nights in the lab, to our conference adventures around the world, thank you for your exceptional friendship over all these years.

Whether its talking science in the lab or over a pitcher, or two; thank you Ashley Makela and Kate Parkins for all the great times. I look forwarding to seeing where you two bring the field of Cellular MRI in the next couple of years! The amazing figures used in publications and this thesis were produced by Chelsey Gareau, thanks for never hesitating to help make a figure perfect.

Special thanks to our close collaborators, Dr. Gregory Dekaban and (soon to be Dr.) Corby Fink for their help and advice. They are the driving force behind the clinical translation of fluorine MRI at Robarts. Without the extensive safety and cell biology validation performed by Corby Fink this work would never have been possible. Our collaboration allowed us to each specialize and focus on tackling important issues in the field of ^{19}F-MRI.

As a member of my advisor committee, thank you Dr. Giles Santyr for helping to shape this thesis. I'd also like to thank the thesis examination committee, Drs. Savita Dhavantari, Robert Bartha, Steven Kerfoot, and T. Kevin Hitchens for their helpful recommendations to polish to this thesis.

Thank you to Dr. Alex Li, Miranda Bellyou, and Joe Gati at the Robarts 9.4T MRI system for all their help and training. I'd also like to thank Kyle Gilbert for developing and maintaining the pre-clinical RF coils. It was amazing having your help to quickly troubleshoot the issues with.

To the Robarts 2nd imaging team, thank you Dr. Tim Scholl, Dr. John Ronald, David Reese and Trevor Szekeres for all your guidance. To Drs. Trevor Wade and Paco Martinez, thank you for always being available to help me with technical questions and troubleshoot the various error messages I caused.

To all my friends in the department, you've made this a great 4 years at Western. I'd particularly like to thank - Justin Peterson, Colin McCurdy, Dr. Damien Pike, and the soon to be Drs., Tom Hrinivich, Patricia Johnson, and Jackie Harris; for their support, both on and off campus. Along with the help of Foster lab I can honestly say my liver will never be the same.

And last but certainly not least, to all my friends and family, thank you for supporting me over the years. To my parents - Sam Gaudet and Betty Wong, and brother - Greg Gaudet; thank you for always believing in my ambitions. Without your positive influence, I wouldn't be where I am today. To my girlfriend, Bethany Jennings, thank you for all the encouragement over the course of my graduate studies.

This work was jointly funded by Ontario Institute for Cancer Research (OICR) – Smarter Imaging Project and Prostate Cancer Canada. JMG received funding from the Translation Breast Cancer Research unit, Cancer Research and Technology Transfer training program, Schulich Dean's award and a Prostate Cancer Canada studentship.

Table of Contents

Abstract ... i

Co-Authorship Statement ... iii

Acknowledgments ... v

Table of Contents ... vii

List of Tables ... xi

List of Figures ... xii

List of Appendices ... xix

List of Abbreviations ... xx

Chapter 1 ... 1

1 Introduction* ... 1

- 1.1 Cellular Therapy ... 1
  - 1.1.1 Regenerative Medicine ... 1
  - 1.1.2 Immunotherapy ... 3
- 1.2 Magnetic Resonance Imaging ... 4
  - 1.2.1 Nuclear Magnetic Resonance ... 5
  - 1.2.2 Generating an Image ... 7
  - 1.2.3 Balanced Steady-State Free Precession ... 8
  - 1.2.4 Iron Oxide-Contrast Agents ... 10
- 1.3 Imaging Cellular Therapeutics ... 10
  - 1.3.1 Cellular MRI ... 11
  - 1.3.2 Labeling Therapeutic Cells for MRI ... 12
  - 1.3.3 Imaging Inflammation ... 14
- 1.4 ^{19}F-MRI Cell Tracking ... 14
  - 1.4.1 Perflurocarbon Imaging Agents ... 17

1.5 Purpose of Thesis 18
1.5.1 Hypotheses 19
1.6 References 20
Chapter 2 33
2 Optimization of Preclinical ^{19}F-imaging Techniques 33
2.1 Equipment 33
2.2 MRI Acquisition Parameters 33
2.2.1 Pulse Sequence 33
2.2.2 ^{19}F Image Resolution 35
2.3 Quantification of Labeled Cells 36
2.3.1 Theory 36
2.3.2 Improving Quantification Accuracy 38
2.4 ^{19}F-Uptake 40
2.5 Anesthesia 41
2.6 Two-colour ^{19}F-MRI 42
2.7 Common Artifacts 43
2.8 References 44
Chapter 3 49
3 Tracking the Fate of Stem cell Implants with Fluorine-19 MRI† 49
3.1 Introduction 49
3.2 Methods 50
3.2.1 MSC Culture and Labeling 50
3.2.2 MSC Implantation 51
3.2.3 MRI 51
3.2.4 Image Analysis and Quantification 52
3.2.5 MSC Immunohistochemistry 52

3.3 Results 53

3.4 Discussion 59

3.5 Conclusions 62

3.6 References 62

Chapter 4 67

4 Application of Dual ^{19}F- and Iron-Cellular MRI Agents to Track the Infiltration of Immune Cells to the Site of a Rejected Stem Cell Transplant‡ 67

4.1 Introduction 67

4.2 Methods 69

4.2.1 hMSC Culture and Labeling 69

4.2.2 hMSC Implantation 70

4.2.3 MRI 70

4.2.4 Image Analysis and Quantification 72

4.2.5 Immunohistochemistry 72

4.3 Results 73

4.4 Discussion 80

4.5 Conclusions 82

4.6 References 82

Chapter 5 89

5 Translation of High-field Fluorine-19 Cell Tracking into the Clinical Realm 89

5.1 Introduction 89

5.2 Methods 91

5.2.1 Labeling of PBMC with Cell Sense 91

5.2.2 Pre-clinical MRI of PBMC Migration 91

5.2.3 Clinical MRI Protocol 92

5.2.4 Cellular Loading Efficiency and Signal Quantification 93

5.3 Results 93

5.4 Discussion 98

5.5 References 101

Chapter 6 104

6 Summary and Future Work 104

6.1 Discussion and Conclusions 104

6.1.1 Chapter 2 & 3 – Development of Pre-clinical ^{19}F-MRI and Tracking the Fate of Stem Cell Implants 104

6.1.2 Chapter 4 – Application of Dual ^{19}F- and Iron-cellular MRI Agents to Track the Infiltration of Immune Cells to the Site of a Rejected Stem Cell Transplant 105

6.1.3 Chapter 5 – Development of a Clinical Protocol for Imaging ^{19}F-labeled PBMC 106

6.2 Limitations 107

6.3 Future Work 109

6.3.1 Application of ^{19}F-MRI to Pre-clinical Disease Models 109

6.3.2 Two-colour ^{19}F-MRI for Imaging Transplant Rejection 109

6.3.3 Phase-I Clinical Trial Investigating Safety and Tolerability of ^{19}F-labeled Human PBMC 110

6.4 References 110

Appendices 112

List of Tables

Table 1: Properties of relevant nuclei 6

Table 2: Comparison of common cell tracking techniques 13

Table 3: PFC relaxation rates vary with agent and field strength... 18

Table 4: Summary of pre-clinical mPBMC migration to popliteal lymph nodes.................. 94

Table 5: Overview of clinical ^{19}F cell tracking protocols published to date 100

List of Figures

Figure 1: Graphs of Longitudinal and Transverse Relaxation rates. In both cases the y-axis is normalized to M_0, the magnetization of the sample induced by the main magnetic field. 6

Figure 2: Balanced steady-state free precession pulse sequence diagram. The time to form an echo (TE) is commonly set to ½ the repetition time (TR). In a single sequence repetition all gradient magnitudes are balanced to produce a net of 0. Figure adapted from "Picture to Proton"[34] 9

Figure 3: (A) Image of the dual tuned birdcage volume coil. The tuning frequency is controlled by driving through one of the two coaxial cable connectors. (B) The Actual Flip angle Image (AFI) shows the field uniformity in the center of the ^{19}F birdcage coil, with each circle representing a 5mm axial slice. The scale on the right indicates the actual flip angle applied to the same following application of a 90° pulse. 34

Figure 4: Cell pellets containing 20,000 (white arrow) and 60,000 (yellow arrow) cells. (A) SNR and image quality is higher, and quantification was found to be more accurate at 2mm^3 resolution, compared to (B) 12mm^3 voxels. 35

Figure 5: In vivo quantification can be performed when labeling cells in culture prior to their administration. Cells are labeled through co-incubation with a ^{19}F-agent overnight to allow for ^{19}F-spins to become internalized within cells. Labeled cells are then split into two separate pellets. The first pellet undergoes process 1, where NMR is used to determine the mean intracellular ^{19}F uptake. The second pellet is administered into the host, either a pre-clinical model or a patient. Process 2 involves conventional ^{1}H imaging of the host to provide the high resolution anatomical images. Then without moving the patient, ^{19}F imaging is performed over the same field of view in process 3. These two images can be overlaid for anatomical context of the ^{19}F signal. An external reference tube of known concentration is imaged alongside the host allowing for the signal from the labeled cells to be converted to number of ^{19}F atoms. By combining this information with the NMR data, the number of cells can be quantified 37

Figure 6: (A) Quantification error from six experiments is expressed as an error multiple from the true value of 1 on a logarithmic graph. The black bars indicate quantification error from raw un-adjusted data sets. (B) An image histogram of this data reveals that all voxels contain some signal value, an assumption that is not taken into account by the quantification software. (C) Improved quantification accuracy is obtained by left-shifting the histogram by subtracting a fixed value, equal to that of the lowest signal voxel, from all voxels as shown in the red bars. 39

Figure 7: (A) Number of mean ^{19}F atoms per cell as measured by NMR was observed to vary by over two orders of magnitude within cell samples. Each data point represents cells prepared for a unique experiment. We found cells from older subjects tended to label less efficiently, in comparison to cells from younger subjects and culture. (B) Incubation concentration of the ^{19}F-agent Cell Sense also influenced cellular uptake. However, at 7.5mg the cell viability was observed to decrease (data not shown). 40

Figure 8: Each isoflurane molecule contains five ^{19}F atoms (A). They are visible in the *in vivo* ^{19}F spectrum of an anesthetized mouse (B, yellow arrow). Here the main CS-1000 peak is visible centered at 0 Hz (white arrow) [-91.5ppm], along with two isoflurane peaks [-86ppm and -81ppm]. 41

Figure 9: (A) Isoflurane signal (red arrow) is visible within the body of the mouse. This signal is spatially offset from its true location in the fat pad (blue arrow) due to the center frequency being locked on Cell Sense. (B) The default truncated sinc pulse is narrower in temporal space then the sinc pulse (D). After fourier transform the wider sinc pulse produces a narrower rectangular shape in frequency space, preventing the excitation of isoflurane (C). 42

Figure 10: By employing the narrow peak selective pulses, the distribution of i.v. Cell Sense (red) can be imaged separately from isoflurane (green). The two ^{19}F images were then combined with an anatomical image 43

Figure 11: Point spread function artifact produced by a region of high intensity signal. The artifact complicates image analysis, particularly when comparing signal between structures in the opposite side of the animal 44

Figure 12: (A) Cellular viability was investigated before and after labeling with the ^{19}F-agent, Cell Sense. Although a statistically significant difference was observed in hMSC after labeling, the viability remained high (>80%) in all experiments. There was no significant difference in mMSC viability. (B) Mean cellular loading was determined by performing NMR spectroscopy on a known number of cells alongside a reference peak with a known number of ^{19}F atoms. We observed variation in cellular loading of both hMSC and mMSC between experimental batches. However, this variation does not affect in vivo ^{19}F quantification since each transplant was only compared to its specific cellular loading........ 54

Figure 13: *in vitro* validation of ^{19}F-MRI quantification accuracy. Quantification was validated in a phantom study using cell pellets ranging from 2x10^5 to 2x10^6 MSC. Pellets were imaged three times, with the error bars representing the standard deviation between scans. The ^{19}F-MRI quantification is in very strong agreement with the true number of cells, and has a Pearson correlation coefficient of 0.99. The red line represents the ideal result of a 1:1 correlation. 55

Figure 14: Comparison of ^{19}F-labeled cell detection in two transplantation models over time (A) Following implantation of 2x10^6 mMSC, ^{19}F-MRI was used to quantify the number of cells remaining over 16 days. By day 16, only 2/7 mice had any detectable signal remaining. A significant difference from day 0 is denoted by ✚, from day 3 by ◆, and from day 9 by ■. (B) The number of detectable cells over a similar time period following a transplant of 1.5x10^6 hMSC. ^{19}F signal was found to decrease at a slower rate, with observable signal in all mice at the endpoint. Statistical significance is denoted in the same way as A. 55

Figure 15: (A, E) Representative MRI from mice receiving either 2x10^6 mMSC or 1.5x10^6 hMSC respectively. The day 0 *in vivo* ^{19}F-MRI quantification correlates very well with the number of implanted cells. The reference tube is marked by “R”. (B) The red fluorescent fluorine agent is clearly visible in the tissue of the immune competent model, (F) as well as in the immune-compromised model. (C) Furthermore, the GFP+ mMSC are observable within the tissue section. (D) Overlaying the two fluorescent images, reveals the ^{19}F agent colocalized with the GFP+ mMSC, as expected. (G, H) H&E stained tissue sections corresponding to the fluorescence microscopy clearly show the implant site of the mMSC and hMSC respectively. Scale bars in all images represent 250µm 57

Figure 16: By day 16, 5/7 immune competent mice had no ^{19}F-MRI signal remaining (A). The reference tube is marked by “R”. (B) Fluorescence microscopy of the muscle agreed with little red fluorescence. No GFP+ mMSC were detectable by fluorescence microscopy, suggesting the original mMSC are no longer present. (C) H&E staining reveals cells at the implant site which correlates with the remaining ^{19}F red fluorescence. (D) Immunohistochemistry staining of adjacent tissue sections with the anti-F4/80 antibody reveals a few macrophages at this location in the immune competent model. (E) At endpoint, all immune compromised mice had detectable ^{19}F-MRI signal remaining. (F) More red fluorescence is visible, and (G)H&E staining again correlates well with the regions of red fluorescence. (H) Macrophage staining reveals many more F4/80 positive cells at the site of implantation corresponding to the regions of red fluorescence. Scale bars represent 250μm.58

Figure 17: Human MSC were labeled with a ^{19}F agent prior to being implanted into the mouse hindlimb muscle. Quantification of the ^{19}F signal performed at this timepoint shows a strong correspondence with the expected number of cells. 2) One day after implantation, iron nanoparticles were administered i.v. These nanoparticles are scavenged from the bloodstream by macrophages and monocytes, rendering them MRI detectable. 3) Two days after implantation, iron labeled macrophages have migrated to the site of implant. The labeled macrophages are visible in MR images as signal voids at the site. ^{19}F-MRI signal is also significantly decreased as the iron quenches the signal. 71

Figure 18: Representative images at each time point from Group A and B. Images were produced by overlaying ^{19}F signal onto proton images for anatomical context. Mice were imaged over 14 days following intramuscular injection of ^{19}F agent labeled hMSC on Day 0 (A,F). Detected ^{19}F signal from the hMSC implant is denoted by a yellow arrow in each image. Quantification of the apparent number of hMSC from ^{19}F signal was calculated using reference tubes of known ^{19}F concentration. The reference tube is visible in panels I & J, and partially visible in panel F. Mice in group A (A-E), received no further treatment besides imaging. Group B mice (F-J) received i.v. iron on Day 1 following fluorine-labelled stem cell transplant. The i.v. iron is taken up by macrophages and monocytes in the bloodstream. On Day 2 (G), a large region of signal void is visible at the implant site. The presence of signal void indicates iron labeled immune cells have migrated to the implant site. This signal void region persists at each time point until endpoint on day 14 (G-J). No signal loss was observed in the muscle of the untreated leg. In addition to the implant site; voids were also visible in the lymph nodes, lymphatics, liver, and spleen. 74

Figure 19: Quantification of ^{19}F signal at each time point. Significance between groups A&B at the same time point is donated with (#). Within the same group, over time is donated (†) between the previous time point and (‡) for between two time points. On day 0, both group A and B signal is in strong agreement with each other and with the expected number of implanted hMSC (1x10^{6}). Overtime, in group A ^{19}F signal decreased at each subsequent time point. This is likely due to cell death and ^{19}F agent clearance by the immune system. In group B, following i.v. iron administration there is a significant decrease in ^{19}F signal (day 2) compared to the previous time point and the Group A mice at the same time point. After this there is no significant change in ^{19}F signal in group B at any other time point. 75

Figure 20: A sham model of Group B was produced by performing an intramuscular injection containing only saline on day 0, followed by intravenous iron on day 1. On day 2, no proton signal voids were detectable within the muscle. Signal voids were detectable within the bone marrow, lymph nodes, and liver, indicating the iron injection was successful. These regions are marked by white arrows. 76

Figure 21: Inflammation was assessed by performing an intramuscular injection containing unlabeled hMSC on day 0, followed by i.v. ^{19}F agent on day 1 [Group D]. A representative ^{19}F/^{1}H overlaid image from day 2 shows a similar inflammation pattern within the muscle [white arrow] as observed with iron oxide (A). On day 2 a mean of 2.5±1.3x10^{18} ^{19}F spins was detected at the transplant site. ^{19}F signal was also detected at the lymph node [yellow arrow]. Unlike Group B, the ^{19}F-labeled macrophages can be quantified over time (B). The relative signal normalized to day 2 within each mouse provides a measure of change in inflammation over time. No significant differences were observed at any time point. 77

Figure 22: Fluorescence microscopy showing the intramuscular injection track on day 2 (A-D) and day 14 (E-H). Macrophages were stained with a green fluorescent lectin+ marker. At the early time point on day 2, macrophages are visible both within and surrounding the stem cell track (A). By endpoint on day 14, macrophages are only found within the transplant track (E). Scale bars denote 300 µm. The red fluorescent ^{19}F agent is visible within the stem cell track from the same tissue sections. More red fluorescence is visible on day 2 (B) then on day 14 (F), in agreement with MRI signal. Cell nuclei were detected with blue Hoeschst staining (C,G). Merged fluorescent images show some bystander labeling of macrophages, appearing as yellow. On day 2, there are few bystander labeled macrophages, as indicated by the separation between red and green fluorescent markers (H). However, by day 14 the majority of ^{19}F agent is contained within macrophages (H). This is highlighted within the magnified inset in the lower left corner (width 150µm). 78

Figure 23: Signal void is visible in the axial proton images of the muscle after stem cell transplant on day 2 (A). The transplant site is denoted by the white arrow. No signal void is visible in the opposite, untreated, hindlimb muscle. Histology reveals the presence of iron within the muscle tissue on both day 2 (B) and day 14 (D). Scale bars denote 300µm. The accompanying stem cell track is outlined by the red fluorescent ^{19}F agent (C,E). More iron is found within the stem cell track at endpoint compared to day 2; often colocalized with the ^{19}F agent. suggesting it is contained within bystander labeled immune cells.............................. 79

Figure 24: MRI provides excellent soft tissue contrast and lymph node detection. Imaging protocol has been developed for a clinical 3T GE MRI (A). ^{19}F imaging is performed with a small dual-tuned surface coil placed on the patients upper thigh, centered on the injection point (B). A coronal orientation MRI with the body coil reveals the lymph nodes as dark spheres [blue arrow] within the fat of the upper thigh (C). The orange dashed line indicates the location of the axial MRI slice (D). In the axial image, the nodes were measured to be approximately 1.5cm below the skin (D).. 95

Figure 25: An array of phantoms containing 0.0001%-1% TFA in 1mL and 15mL tubes imaged with both the large and small surface coils (A). In the sagittal proton image of this phantom, the blue arrows indicate tubes that were detectable with both coils, but only the small surface coil displayed sufficient sensitivity to detect those marked by the red arrows. The lowest concentration detected, 0.001% represents the signal on the same order of magnitude of a million PBMC. Using the smaller coil did result in a significant increase in signal drop off with depth compared to the larger coil (B). Cell pellet phantoms created by centrifuging 1x10^{6}, 5x10^{6} and 10x10^{6} Cell Sense-labeled PBMC and overlaying with 1% agarose in an eppendorf tube (C). PBMC phantoms were placed on a saline bag and scanned at 3T and all 3 phantoms described in (C) were detected using ^{19}F cellular MRI (D), with a hot-iron colour scale used for ^{19}F MRI. 96

Figure 26: Human PBMC can be detected under clinical conditions following injection into a ham shank. Cells were administered interdermally in 4 doses [yellow arrows], 20x10^{6} (A), 10.5x10^{6} (not shown), 4.5x10^{6} (B) and 1.5x10^{6}. Only the smallest dose (1.5x10^{6}) was undetectable with our imaging parameters. An additional 4.5x10^{6} dose was administered subcutaneously [blue arrow], which is visible at 1.2cm depth as measured with MRI. Images were performed alongside a pair of reference tubes (R) of known ^{19}F concentration allowing for signal quantification. The surface coil was placed directly on the ham shank, with the reference tubes taped inside the coil elements (C). A representative human ^{1}H image taken with the same parameters closely resembles the ham images in both tissue appearance and subcutaneous fat disposition (D). 97

Figure 27: Comparison of signal produced by 20 million PBMC from two different donors. Two doses of 15x10^{6} PBMC were prepared from different sources. In the first, a high labeling efficiency (1.2x10^{11} ^{19}F/cell) was observed producing a strong signal in the ham shank (A). The second source had a low labeling efficiency (4.2x10^{10} ^{19}F/cell), resulting in a low observed signal (B). 98

List of Appendices

Appendix A: Permissions 112

Appendix B: Curriculum Vitae 113

List of Abbreviations

^{19}F – fluorine-19, natural isotope of fluorine

^{1}H – hydrogen-1, proton

PFC – Perfluorocarbon

Gd - Gadolinium

MRI – Magnetic Resonance Imaging

MPI – Magnetic Particle Imaging

BLI – Bioluminescence Imaging

SPECT – Single Photon Emission Computed Tomography

PET – Positron Emission Tomography

MSC – Mesenchymal Stromal/stem Cell

PBMC – Peripheral Blood Mononuclear Cells

T – Tesla

SPIO – Super Paramagnetic Iron Oxide

PPB – Perl’s Prussian Blue

SE – Spin Echo

GE – Gradient Echo

bSSFP – balanced Steady-State Free Precession

ip – Intraperitoneal injection

iv – Intravenous injection

im – Intramuscular injection

Chapter 1

1 Introduction*

This thesis develops and advances magnetic resonance imaging (MRI) techniques for non-invasive, in vivo tracking of cellular therapeutics. Research was performed with imaging phantoms and animal models. This introductory chapter discusses cell therapy, cellular imaging techniques, and cellular MRI to provide background and motivation for the research presented in this thesis.

1.1 Cellular Therapy

Cell therapy involves the administration of healthy cells into a patient in order to treat a disease or condition. Therapeutic cells from the patient can be specialized and expanded *in vitro*, then re-administered to the most favourable location in the patient. Pre-clinical experiments have shown that cellular therapy has the potential to revolutionize numerous fields within modern medicine; with applications ranging from regenerative medicine to immunotherapy.

1.1.1 Regenerative Medicine

Stem cell transplants are of particular interest for treating a variety of chronic disorders. Defined by the cell potency, “true” stem cells are pluripotent allowing for differentiation into any cell type. Multipotent stem cells, also known as progenitor cells, have the potential to differentiate into multiple cell types, but are limited compared to pluripotent cells. Mesenchymal stem cells (MSC) were first defined in 1991 by A.I. Caplan. to denote the

---

*This chapter contains sections which have been previously published. Section 1.3.1, and 1.4 contain exerts from: Fox MS, Gaudet JM, and PJ Foster (2015) “Fluorine-19 MRI contrast agents for cell tracking and lung imaging,” *Magnetic Resonance Insights* 8(S1):1-15. Copyright is held by the authors. Section 1.3, 1.3.2, and 1.3.3 contains exerts from: Makela AV & Murrell DH, Parkins KM, Kara J, Gaudet JM and PJ Foster (2016)

“Cellular Imaging with MRI,” *Topics in Magnetic Resonance Imaging* 25(5): 177-186. Sections are reproduced with permission (see Appendix A).

stromal progenitor and presumed stem cells for the skeletal tissues of bone, cartilage, muscle and fat.[1] First derived from bone marrow, MSCs are one of the most investigated stem-like cells in clinical research. With applications in generating cardiac muscle,[2,3] stroke recovery,[4,5] and osteoarthritis repair;[6] MSCs have the additional advantage of being present in adult tissue. In addition to directly replacing damaged tissues, stem cells have been shown to exert a local therapeutic effect through the release of trophic factors.[2,7,8] Studies have shown that under the right conditions MSCs can be induced to pluripotency. However, recent work has shown that individual MSCs in culture are often already pre-dispositioned to certain lineages, disputing the claim of true multipotency.[7,9] This has led to extensive debate on “how potent” an individual cell must remain to be considered a stem cell.[7,9,10] Numerous groups have advocated for new definitions of MSCs, differentiating multipotent stromal cells from bone marrow derived mesenchymal stem cells.[9,11,12] For simplicity, the term MSC as used in the remainder of this thesis refers to the encompassing broad MSC definition, without attempting to differentiate based upon the potency of the cells in culture.

Ultimately, the restorative effects of regenerative medicine relies on the arrival and survival of the cells at the targeted destination. Stem cells can be administered either systemically or at the therapeutic site.[7] In either case, the cells must adapt to the local environment following expansion and specification in culture. Studies have shown that the majority of stem cells die in the days following transplantation.[13–17] This may occur from a number of factors, such as: shear stresses encountered with needle delivery or insufficient access to nutrients. In either event, pro-inflammatory cytokines are released by dying stem cells, which in sufficient quantities is capable of trigging an influx of immune cells to the site of transplant.[18,19]

Transplant rejection is further mediated by differences in the genetic background of the stem cells and host. This can occur as a rapid acute response from the recipient’s immune system towards the major histocompatibility complex (MHC) of the donated cells,[18,19] or a long-term chronic rejection involving loss of vascularity.[19] Alternatively, in the case of tissue transplants, donor immune cells present within the transplant may attack the host tissue; a process known as graft-versus-host disease (GVHD). For human cellular transplants, ideally stem cells are collected from the individual patient themselves, preventing adaptive immune rejection and GVHD, producing an autologous transplant. However, depending on the disease/condition and previous therapeutic treatments, these autologous cells may not be suitable for administration. Isografts are a near-ideal alternative with donor cells produced by a genetically identical background, such as an identical twin. Clinically, allograft transplantations are the most common, involving non-genetically identical donors. In these cases, immunosuppressive drugs are commonly required to prevent transplant rejection. Recent work has suggested that MSCs may display immune privileged properties, potentially allowing for unassisted allogeneic donation.[7,12,20] However the degree of immune suppression has been contested with many reports suggesting it is insufficient to prevent allograft rejection.[12,16]

These models can be tested pre-clinically; with isografts produced by in-bred murine strains and allografts using cells between murine strains. In addition, xenografts can be investigated with donated cells from a different species as the host. This often results in hyper-acute rejection of the transplants,[21] although stable xenografts can be produced with severely immune-compromised mice transplanted with human stem cells.

1.1.2 Immunotherapy

In the field of cancer immunotherapy, the patient's immune system is primed to target the tumour. This can be accomplished by introducing antigen-presenting cells (APCs) which have been exposed to tumour antigen *in vitro* prior to administration. Once treatment has been delivered to the patient, the APCs must migrate to a secondary lymphoid organ in order to elicit an immune response. Here APCs interact with other cells of the adaptive immune system, such as T-cells, which ultimately proceed to target the tumour.[22–24] Unlike traditional prophylactic vaccines, these treatments are meant to be therapeutic providing alternative treatment options.

For many years, dendritic cells (DCs) have been investigated as the ideal APC for application in immunotherapy. In vivo, DCs play a pivotal role in initiating the immune response to foreign antigens. Capable of being derived from bone marrow or blood monocytes; DCs are characterized as highly MHC II expressing, with the absence of lineage markers, such as: CD14 (monocytes), CD19 (B-cells), and CD68 (macrophages).[25,26] Since the first DC clinical trial was reported in 1996 for B-cell lymohoma,[27] many patients have undergone vaccination trials for a range of cancers. Unfortunately, clinical success of DC-therapy has been limited with the majority of trials failing to show significant survivorship benefit.[22,23,28,29] It is clear that additional research is necessary to improve DC migratory efficiency and ensure immune tolerance is avoided to improve clinical outcomes.[28]

On April 29, 2010, Sipuleucel-T, a cellular vaccine treatment was approved and licenced by the US FDA for metastatic castrate-resistant prostate cancer (mCRPC). Although localized prostate cancer has a good prognosis, there are currently few treatment options following systemic spread. In multiple Phase III clinical trials, Sipuleucel-T has shown a statistically significant survivor benefit over placebo controlled groups.[24,30] Treatment involves loading autologous peripheral blood mononuclear cells (PBMC) with an antigen construct containing prostatic acid phosphatase (PAP) and granuocyte macrophage colony-stimulating factor (GM-CSF). The PBMC fraction consists of a heterogeneous mixture of cells, containing professional APCs, such as: DCs, monocytes, and B-cells; along with activated: T- and NK cells. Following *in vitro* antigen loading of the PBMC, the cells are administered intravenously back into the patient.[31] While cancer immunotherapy has only shown modest overall survival benefits in the clinic, progression-free survival was not significantly improved.[30,32] Coupled with the high cost of treatment innovative approaches, such as those presented within this thesis, are necessary to advance the clinical application of cancer immunotherapy.

1.2 Magnetic Resonance Imaging

The following sections are meant to provide a brief overview of the fundamental processes involved with generating an MR image. Additional information can be found in several textbooks, such as: “Magnetic Resonance Imaging: Physical Principles and

Sequence Design, 2^{nd} ed." by Robert Brown et al.[33] and "From Picture to Proton" by McRobbie et al.[34]

1.2.1 Nuclear Magnetic Resonance

At the single voxel level, signal in MRI is derived from the dissipation of energy from spinning nuclei within a magnetic field. All nuclei have a characteristic spin (I) value; however only those with non-zero spins (I=1/2, 1, 3/2, …) produce a nuclear magnetic resonance signal. In MRI, most nuclei of interest are spin ½. When a collection of spins are placed within an external magnetic field (B_0), these spins either align with or against the applied field. Signal in MRI is governed by the small excess proportion of these spins in the lowest energy state; or those in alignment with B_0. The energy difference between the two states is dependent on the strength of B_0, as shown in Equation 1.

$$\Delta E = \frac{\mu B_o}{I} \qquad \text{(eq.1)}$$

Where μ is the nuclei's magnetic moment (discussed further in Table 1). As the difference in energy level increases, a higher proportion of spins align with B_0. At thermal equilibrium, the ratio of spins in each population can be described with the Boltzmann distribution (Eq. 2). Here, N^+ and N^- represent the number of spins in alignment with or against B_0 respectively, k is the Boltzmann constant, and T is the temperature of the system. For this reason, imaging at higher field strengths (7T, 9.4T, 11.7T) improves signal compared to clinical magnets (1.5T, 3T).

$$N^+/_{N^-} = e^{\frac{-\Delta E}{kT}} \qquad \text{(eq.2)}$$

In addition to spin state, nuclei also present a characteristic precession about the main magnetic field. Governed by the nuclei's gyromagnetic ratio (γ) and B_0, the Larmor frequency is given by Equation 3.

$$\omega_o = \gamma B_o \qquad \text{(eq.3)}$$

Table 1: Properties of relevant nuclei

Element	Gyromagnetic Ratio (MHz/T)	Natural Abundance (%)	Magnetic moment (μ/μ_N)	Nuclear Spin
^{1}H	42.57	99.98	2.793	½
^{19}F	40.08	100	2.629	½

Energy can be provided to excite the nuclei by applying a radiofrequency (RF) pulse at the nuclei's Larmour frequency. Following excitation, the net magnetization (M) returns to the lowest energy state through the longitudinal (T_1) and transverse (T_2) relaxation time constants. T_1 relaxation involves the growth of magnetization (Fig 1A), along the direction of the B_0 field, defined as the z-axis. This occurs through the transfer of energy from the excited nuclei to the lattice. T_2 relaxation governs the exponential decay of magnetization (Fig 1B) within the xy-plane through transfer of energy between spins resulting in loss of phase coherence. The observed transverse relaxation rate ($1/T_2^*$) is accelerated due to reversible dephasing because of: off resonance effects, molecular mechanisms, and magnetic field inhomogeneities.

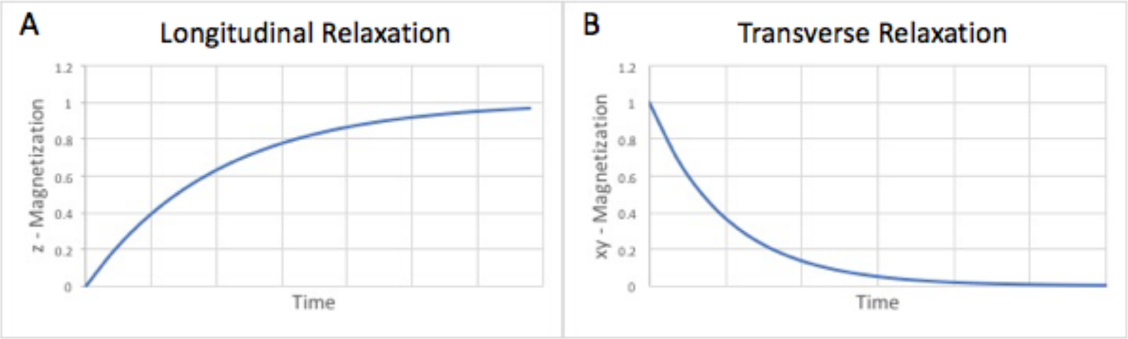

Figure 1: Graphs of Longitudinal and Transverse Relaxation rates. In both cases the y-axis is normalized to M_0, the magnetization of the sample induced by the main magnetic field.

1.2.2 Generating an Image

In MRI a magnetic field gradient along each Cartesian axis (x,y,z) is utilized to provide spatial localization of voxels. These magnetic gradients are many orders of magnitude smaller than the main magnetic field and are highly controlled. The application of a gradient influences the precession frequency of the nuclei across the gradient, resulting in a distribution of phases associated with the spatial location. Spatial information is obtained by assigning a unique initial phase and frequency to each location. This achieved by manipulating the duration and magnitude of these gradients across the field of view.

The timed RF excitation and magnetic field manipulations are defined in the MR pulse sequence. There are two categories of sequences, characterized by the method used to generate transverse magnetization coherence. In a standard spin echo (SE) sequence, spins are first excited by a 90° RF pulse. Magnetization is refocused (known as an echo) some time later by applying a second RF pulse, which reverses the direction of the spins. This reversal causes the spins to rephase and regain spin coherence at the echo time (TE). Due to the second RF pulse, SE sequences refocus all reversible signal and have the advantage of obtaining optimal signal per excitation, governed by T_2.

The second type of sequence forms an echo through inverting the applied magnetic field gradient. For gradient echo (GE) sequences, an initial RF pulse is again used to excite the spins, although the flip angle is generally <90°. After excitation, the frequency encode gradients are applied to enhance dephasing, then reversed in amplitude to form an echo at TE. However, the resulting echo does not correct for field inhomogeneities, resulting in the T_2* reductions to signal. Despite obtaining lower signal per excitation, this is offset by the capability to perform lower repetition times (TR) between excitations; which allows for more signal averaging within the same time period.

In either case, the formation of an echo induces a current in the receive coil which is translated into a digital signal and stored in an array matrix known as k-space. Data in k-space represent spatial frequencies, with each individual point containing frequency and phase information on every voxel in the corresponding image. The center of k-space contains information on low frequencies, such as crude contrast and shapes; while high frequency information is found in the periphery of k-space, providing the boundaries and details. From here the data can be extracted from k-space and an MR image formed using the Fourier transform. This acts to separate the signal into a sum of sine waves with varying frequency, phase, and amplitude.

The signal intensities of an individual image voxel are governed by three factors: the spin density, T_1, and T_2 values of the material being imaged. The spin density governs the maximum potential magnetization (M_0) providing the upper limit on the signal available to be detected. Image contrast is also influenced by the choice of pulse sequence and can be manipulated by adjusting the TR and TE of the sequence. For example, imaging with a long TE allows material with a short T_2 to relax reducing the observed signal. Meanwhile, material with a longer T_2 would appear brighter as more spins are rephased to form the echo. The manipulating the TR has a similar effect on the images by varying the magnetization excited into the xy plane.

1.2.3 Balanced Steady-State Free Precession

Balanced steady-state free precession (bSSFP) is an advanced GE pulse sequence, and is also known by the vender specific names FIESTA, TrueFISP, and Balanced FFE. Unlike with conventional sequences, magnetization is not allowed to completely return to M_o prior to re-excitation. This generates a transverse and longitudinal magnetization steady-state after successive excitations. In addition, all gradient waveforms are also balanced to a net value of zero in each TR, as shown below in Figure 2.

Due to the magnetization steady-state, contrast is dependent on the ratio between T_2/T_1. The optimal flip angle is given by Equation 4, and results in the magnetization amplitude given by Equation 5.[35]

$$\cos(\alpha) = \frac{{}^{T_1}/_{T_2} - 1}{{}^{T_1}/_{T_2} + 1} \qquad \text{(eq.4)}$$

$$M_{ss} = \frac{1}{2} M_o \sqrt{{}^{T_2}/_{T_1}} \qquad \text{(eq.5)}$$

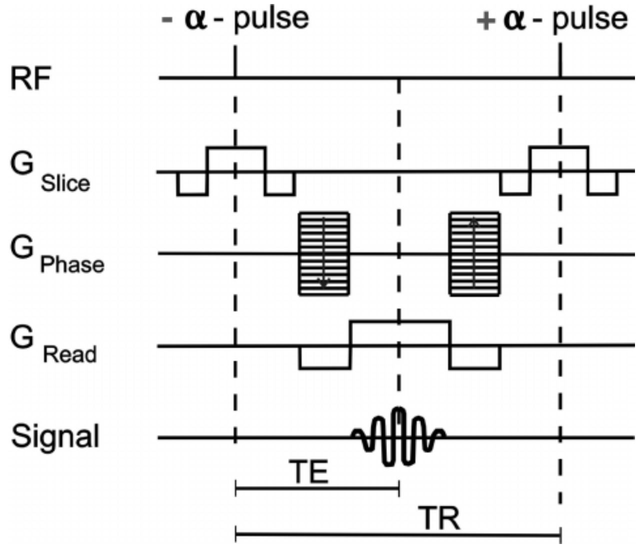

Figure 2: Balanced steady-state free precession pulse sequence diagram. The time to form an echo (TE) is commonly set to ½ the repetition time (TR). In a single sequence repetition all gradient magnitudes are balanced to produce a net of 0. Figure adapted from "Picture to Proton"[34]

bSSFP has the advantage of generating high signal-per-unit time images. This is accomplished by keeping TR extremely low ($TR<<T_1$, often <10ms), which allows for high signal averaging. However, this has the disadvantage of requiring strong gradient slew rates and increased tissue heating, measured through specific absorption rate (SAR).[35]

The pulse sequence displays a characteristic banding artifact. This occurs since the transverse magnetization approaches zero at multiples of 2π. This can be offset by a technique known as phase cycling, which varies the location of the dark bands allowing for them to be removed through signal averaging.

The high signal advantages and unique contrast generated by bSSFP have been utilized for real-time cardiac imaging,[35] angiography,[35] oncology,[36] and cellular MRI.[37,38] The lack of T_2* dependence on signal is particularly useful for controlling the size of the blooming artifact produced by superparamagnetic iron oxide (SPIO) nanoparticles.

1.2.4 Iron Oxide-Contrast Agents

In MRI, regions of interest (ROIs) can be emphasized using paramagnetic and superparamagnetic agents which influence the image contrast. Localized positive enhancements to the signal can be achieved with gadolinium or manganese agents, while negative contrast can be generated with iron oxide agents. When imaged with a MRI, SPIO particles result in a reduction in the local T_1, T_2, and T_2*. This is caused by disturbing the local magnetic susceptibility and is most pronounced in the immediate vicinity of the superparamagnetic material. With conventional sequences, the T_2 and T_2* reductions appear as a region of negative contrast on the image. The size of this region is dependent on a number of factors, such as: the pulse sequence timing, method of echo formation, and field strength;[39] with the largest effects visible in T_2*-weighted images.[33] Positive image contrast is possible with certain advanced methods such as: ultrashort echo time (UTE) imaging, with the echo formed in less than the T_2*;[40] or through inversion recovery with on-resonance water suppression.[41]

1.3 Imaging Cellular Therapeutics

While pre-clinical experiments have shown that cellular therapy can be successful, despite decades of research, cellular therapy has been unable to meet clinical expectations. One problem exists in that once these cells are re-administered to the patient it often takes months before diagnostic feedback is available. In this time, it is unknown if the cells are providing any therapeutic benefit to the patient.

Cellular imaging aims to shed light on the *in vivo* fate of these therapeutic cells. By directly and non-invasively imaging these cells, imaging provides a window through which we can confirm correct administration, observe migration, and evaluate longitudinal status of the cells. In the pre-clinical setting, imaging allows for more rapid treatment optimization in animal models, as data can be obtained throughout therapy instead of just at the endpoint. In the clinic, imaging presents an avenue to evaluate the success of therapy at multiple time points, often before symptomatic indicators are available. This provides the capability to verify both the success of delivery and evaluate treatment progression, providing the capability to intervene if necessary.

There are currently several established *in vivo* cell-tracking methods including: optical (fluorescence microscopy & bioluminescence imaging [BLI]), radioactive tracers (positron emission tomography [PET] & single-photon emission computed tomography [SPECT]), and MRI using heavy metal contrast agents (superparamagnetic iron oxide [SPIO] & paramagnetic gadolinium [Gd]). Each of these modalities has their respective advantages and disadvantages. For example, BLI signal is semi-quantitative and only produced by living cells, but is attenuated with tissue depth and requires non-native transfected cells.[42,43] By comparison, PET is highly sensitive at all depths and is clinically translatable, but the ionizing radiation can be highly toxic to sensitive therapeutic cells.[44] In addition to these methods, there are two recently developed technologies, magnetic particle imaging (MPI)[45] and fluorine-MRI (^{19}F-MRI).[46] The relative differences between some of the more common techniques are compared in Table 2. The values presented are approximate guidelines of each technique; with values being highly dependent on imaging time, protocol and equipment.

1.3.1 Cellular MRI

In comparison to other cell imaging techniques, cellular MRI has the advantage of being clinically translatable without exposure to ionizing radiation. The anatomical images provide excellent spatial resolution and soft tissue contrast. Most cellular MRI to date has been performed with SPIO. Cell tracking with iron oxide was first utilized by Bulte et al. and Yeh et al. in the early 1990s by internalizing iron oxide particles within cells and detecting the resulting negative signal contrast.[47–49] The disruption of the local magnetic field can be used to determine the spatial localization of iron oxide. In T_2-weighted images this provides cell spatial localization near that of the proton image resolution. The resulting signal void occupies a much larger spatial region than the individual cells themselves preventing the need for magnification. As previously discussed in Section 1.2.4 and in Table 2, small quantities of label can have large detectable effects on the magnetization of the surrounding spins. This has led to extremely high detection sensitivity, with single cell detection possible under certain conditions.[37,50] However, since detection of the agent relies on a change in image contrast, localization of the iron oxide is limited by low specificity. Dark regions with low proton density, such as the bone and lung, can appear similar to iron oxide signal void. In addition, *in vivo* quantification of iron containing cells is complex. The fractional signal loss produced by SPIO is only linear at very low concentrations of iron oxide, and quickly reaches a saturation point after which further signal loss does not occur.[37] This makes it extremely difficult to quantify the amount of iron present within a signal void. Nevertheless, over the years SPIO have been used to track a vast range of cells, such as: immune cells,[44,51–54] stem cells,[55–57] cancer cells,[58–60] and pancreatic islets.[61]

1.3.2 Labeling Therapeutic Cells for MRI

Cells of interest must first be labeled with an imaging agent allowing for their specific detection. These agents can be genetically engineered into the cells,[68] administered to the cells in culture prior to administration,[69] or injected intravenously to label native cells *in situ*.[14] For imaging cellular therapeutics with MRI, the most common method employed to label cells is *in vitro*. This provides the greatest control of label uptake, ensuring only the specific cells of interest are labeled.

In general, there are three classes of iron oxide agents used in imaging: 1) ultra-small superparamagnetic iron oxide nanoparticles (USPIO) [5-50nm], 2) superparamagnetic iron oxide nanoparticles (SPIO) [50-150nm], and 3) micron-sized iron oxide particles (MPIO) [1μm]. A single MPIO particle contains >5pg/Fe, an amount equivalent to 1.5 million SPIOs or 4.3 million USPIOs.[70] The iron oxide core is often surrounded by a dextran coat to prevent aggregation and enhance biocompatability.[71] Although there are no FDA approved iron oxide cell imaging agents, one agent is currently being investigated for off-label use. Ferumoxytol is an I.V. administered USPIO-sized agent used to treat iron-deficiency. Many cell types are capable of taking up nanoparticle-sized agents without intervention, and these cells can be labeled to sufficient levels for imaging (>1pg/Fe per cell) by simple co-incubation. This is particularly important when considering clinical feasibility, since transfection agents are not required. Cells mediate

Table 2: Comparison of common cell tracking techniques

	MRI - Iron oxide	**MRI - ^{19}F**	**PET - ^{18}F[62,63]**	**SPECT - ^{111}In[64,65]**	**MPI - Iron oxide[45,66]**	**BLI -luciferase[42,67]**
Sensitivity	1-10 cells (0.01ng/voxel)[37]	10,000 cells (300ng/voxel)	100-1000 cells	100-1000 cells	100 cells (5ng/voxel)	1000 cells
Cellular loading	>99% (1-10pg/cell)[37]	>99% (0.3-30pg ^{19}F/cell)	4-99%	4-25% (diluted)	>99% (1-25pg/cell)	>95%
Resolution	µm	mm	mm	mm	mm	mm
Bystander labeling	Yes	Yes	Yes	Yes	Yes	No
Quantifiable	Semi	Yes	Yes	Yes	Yes	Semi
Imaging Time	Minutes	Minutes	Seconds	Seconds	Seconds	Seconds
Longitudinal potential	Months	Months	Hours	Days	Months	Months
Total Imaging Cost	$$$	$$$$	$$$	$$$	$	$
Clinical translatability	Under evaluation	Under evaluation	Approved	Approved	No	No

nanoparticle uptake through a variety of endocytosis pathways; including: phagocytosis, clathrin-, and caveolin-mediated endocytosis.[41,72] The preferred method is dependent on cell type, as well as the size and surface coating of the agent. Following internalization, the nanoparticles are contained within vesicles in the cytoplasm. Higher label-uptake is possible with phagocytic cells, which are capable of taking up additional label through phagocytosis.[72] Following label internalization, it is also important to ensure that these agents do not induce functional or phenotypic changes in the cells that they label. Numerous studies have shown that labeling MSCs does not impact short- or long-term viability, proliferation, or differentiation into adipogenic or osteogenic lineages.[56,73] However, Rohani et al. demonstrated differences in activation and migration of DCs labeled with micron-sized iron oxide particles.[51]

1.3.3 Imaging Inflammation

Besides labeling cells in culture, phagocytic cells can also be labeled *in situ* following intravenous (i.v.) administration of an imaging agent. This is particularly useful for tracking localized inflammation, through the large influx of immune cells. In mice, the cellular imaging agent is administered through the tail vein with imaging performed 24 hours later. Most of the agent is cleared from the blood through the mononuclear phagocytic system, resulting in uptake by; Kupffer cells in the liver, monocytes in the bone marrow, and macrophages in the lymph nodes and spleen. Applications have been shown in a variety of fields, such as: myocardial infarct,[74,75] stroke,[76] transplant rejection,[13,14,53,77] tumour-associated macrophages,[78,79] and spinal cord injury.[80]

1.4 ^{19}F-MRI Cell Tracking

The first ^{19}F observations were attempted with NMR in 1942,[81] followed by MRI in the 1970s.[82] Since then, ^{19}F imaging agents have been used for a variety of purposes, such as to measure the intracellular partial pressure of oxygen[83] and as a gastrointestinal contrast agent by proton displacement.[84] Nuclear magnetic resonance signal from ^{19}F has been used to investigate lung structure and drug pharmokinetics. Unlike with iron oxide agents, nuclear magnetic resonance signal from the ^{19}F atoms are directly detected and there is no disruption to the underlying proton image contrast. Once the detection threshold has been reached, the signal produced is linearly proportional to the number of ^{19}F atoms, allowing for quantification;[85] details of which are expanded upon later in Chapter 2. A drawback of this direct detection is the relative insensitivity of the nuclear magnetic resonance signal. As discussed in Section 1.2.1, signal in MRI is governed by the surplus of spins in alignment with the main magnetic field. With standard MRI this is not a concern, due to the high abundance of ^{1}H in biological tissue. For ^{19}F-MRI, a large number of additional ^{19}F atoms must be introduced to the cell in order to produce enough NMR signal to be detectable. This requires mM concentrations (~ 10^{15} ^{19}F atoms) per voxel for imaging.[86] However, due to the near-absence of native ^{19}F-atoms in biological tissue no background signal is observed, providing excellent imaging specificity.

The first application of ^{19}F-MRI for cell tracking was demonstrated in 2005 by Ahrens et al.[46] In this study, immunotherapeutic DCs were tracked following subcutaneous injection to the draining popliteal lymph node.[46] Cells were labeled *in vitro* by co-incubation with an emulsified perflurocarbon (PFC), which was internalized through phagocytosis. Anatomical localization was achieved by overlaying the ^{19}F image onto a traditional proton MR image. In the 11 years since this first study, the field has grown at an exponential rate,[87] with significant advances in hardware,[88–90] image acquisition,[56,91,92] and data processing.[93,94] To date, most of this work has been performed at high-field strengths (>7 T), to improve sensitivity of ^{19}F-MRI. Studies have demonstrated ^{19}F can be added to cells in culture and used to track stem cells from hematopoietic,[95] neuronal,[96] and mesenchymal progenitors;[56] as well as a variety of immune cells, such as: DCs,[46,97,98] NK cells,[99] T-cells,[100] and macrophages.[77] PFC uptake has been observed in both T- and B-cells, which have been historically difficult to label with SPIO-based agents.[100]

Dendritic cells have been by far the most frequently imaged cell type with ^{19}F-MRI. Besides the natural phagocytic ability allowing for high intracellular label uptake in the range of 10^{12} ^{19}F atoms/ cell; DC do not undergo mitotic cell division preventing the diffusion of label. Finally, the known migratory pathway to the draining lymph nodes provides the perfect translation model for assessing *in vivo* functionality with imaging. Building on previous work by Dr. Ahrens, in 2010 Helfer et al. introduced the first commercial ^{19}F imaging agent by imaging the migration of DCs to the draining popliteal lymph node.[97] In this study, extensive work was performed to show that labeling did not negatively affect the expression of surface markers, DC maturation, and T-cell stimulatory function.[97] In 2011, a German group led by Dr. Waiczies showed that the labeling efficiency of DCs increased with the PFC particle size, up to a maximum of 560nm diameter.[101] Interestingly, their work showed improved T-cell activation following ^{19}F-loading of DCs;[101] suggesting heavy intracellular ^{19}F-uptake may act to induce DC maturation processes. With these promising results, the clinical feasibility of detecting DCs in vivo was first explored in 2011 by Bonetto et al.[102] In this work, they showed an intracellular uptake of 1.7×10^{13} ^{19}F/cell, the highest reported labeling efficiency to date.[102] Using a spin density weighted SE sequence on a 7T system, a minimum of 2000 cells/voxel could be detected in phantoms.[102] These results were extrapolated to provide an estimation of a minimum detection threshold of 30,000 cells/voxel on a clinical 3T MRI,[102] or around 5×10^{17} ^{19}F atoms.

Another common application of ^{19}F-MRI has been for imaging stem cell transplants. The field is well suited to ^{19}F-MRI, since large numbers of stem cells are routinely administered in translational models. Like with DCs, PFCs have been shown to not negatively influence stem cell surface markers, differentiation, or proliferation.[56,103] Using relatively simple transplantation models has allowed for groups to test and optimize more advanced 19F techniques. An example of this is in 2007, Partlow et al. demonstrated that two-colour ^{19}F-MRI could be used to distinguish separate populations of stem cells that had been labeled with different PFC agents.[95] By selectively exciting each agent individually, the different cell populations could be imaged in sequential ^{19}F scans.

Immune cells can also be labeled *in situ* by *i.v.* administration of PFC, in the same way as described in Section 1.3.3. However, with ^{19}F-MRI this allows for both the inflammatory sites to be both spatially localized and the relative level of inflammation to be compared.[74,75,104–107] In addition to the quantification potential, imaging inflammation with ^{19}F-MRI produces few anatomical image distortions compared to iron oxide. This is particularly advantageous when imaging arthritic inflammation around joints, where the negative iron contrast can be easily confused with the low proton density bone. In a study by Balducci et al., ^{19}F-MRI was used to assess longitudinal responses to an arthritis therapy.[108] Inflammation as marked by ^{19}F-signal was observed to increase in untreated controls, but ^{19}F-signal remained constant in prednisolone treated animals.[108] Unfortunately no ^{19}F clearance was observed overtime, despite the success of therapy as measured by other clinical responses.[108] This highlights one of the drawbacks of using cellular MRI for longitudinal inflammatory imaging, macrophages are known to remain in the tissue for an extended period of time after the initial inflammation subsides. In addition to imaging inflammation near bone, cardiac tissue is another region where joint ^{1}H/^{19}F MRI has an advantage over previous techniques. In 2008, Flogel et al. imaged inflammation following cardiac ischemia, showing a time dependence on the observed ^{19}F-signal between 1 and 6 days post ischemic event.[75] This differed from results observed in a similar model using SPIO, where no difference in fractional signal loss was observed after 24 hours.[13] This is likely due to the saturation of the signal loss that occurs with iron-oxide, and highlights the advantage of using ^{19}F-MRI for quantitative analysis. ^{19}F MRI has also been utilized to image acute allograft rejection following heart transplantation in mice.[107] Inflammation could be differentiated and quantified between the left and right ventricles of the heart,[107] potential allowing for targeted interventions to be performed to prevent the organ from being rejected.

1.4.1 Perflurocarbon Imaging Agents

Due to the toxicity of ionic ^{19}F atoms, imaging is predominately performed with biologically inert PFC. These agents make use of the carbon-fluorine bond, the second strongest bond in organic chemistry, which cannot be naturally broken.[109] This produces biologically safe, inert agents for imaging. In the 80's, PFCs were evaluated as a blood substitute option in patients due to the high affinity for O_2.[110] In comparison, for cell tracking applications only minuet quantities of PFC are used, with clearance through the monocyte-phagocyte system and lung exhalation.[111,112]

PFCs are generally produced by replacing hydrogen atoms on hydrocarbon chains and can be designed to be linear (perfluoropolyether [PFPE]) or cyclic (perfluoro-15-crown-5-ether [PFCE]). In either case, the ideal imaging agent possesses a high number of ^{19}F atoms with a single resonant peak and a short T_1 allowing for rapid imaging. Table 3 lists relaxation times at a variety of field strengths for commonly used ^{19}F agents in cell tracking.

Table 3: PFC relaxation rates vary with agent and field strength

Agent	**Single Peak**	**# ^{19}F Spins**	**T1 (ms)**	**T2 (ms)**
PFPE	No	28-36	3T: 470[112] 7T: 590,[113] 425[114] 9.4T: 510[113] 11.7T: 280,[115] 380[115]	3T: 250[112] 7T: 82[114] 11.7T: 153,[115] 68[115]
PFCE	Yes	20	7T: 2500,[113] 950[100] 9.4T: 580,[98] 600,[93] 1000[116] 11.7T: 800[97]	7T: 50[100] 9.4T: 536,[98] 300,[93] 350[116]

At the moment there is only a single commercial PFC designed for cell tracking. Based on a PFPE backbone, Cell Sense (CS-1000, CelSense Inc.) is produced under the Good Manufacturing Practices (GMP) required for clinical applications. As such it is the only commercially available, FDA-approved cellular MRI agent. For pre-clinical work, the agent is available in fluorescently tagged variants (CS-1000 DM-red), as well as in a form suitable for IV injection for *in situ* labeling of phagocytes (VS-1000).

1.5 Purpose of Thesis

Since 2005, numerous proof-of-concept studies have been performed with a variety of cell types in various disease models. However, until recently, this work has been restricted to a handful of laboratories with the necessary combination of expertise and equipment. The purpose of this thesis was to develop technology and implement the first ^{19}F-imaging site in Canada, capable of both pre-clinical and clinical cell tracking.

1.5.1 Hypotheses

1. Transplanted cell number and spatial location can be non-invasively monitored with longitudinal ^{19}F-MRI.
2. Differences in stem cell fate can be detected between isograft and xenograft transplantation models with ^{19}F-MRI.
3. The combination of ^{19}F-labeled stem cells and iron-labeled immune cells will allow for simultaneous MRI446 of transplant rejection.
4. Clinical cell tracking will be feasible with ^{19}F-MRI for a future cancer immunotherapy clinical trial.

In Chapter 2, the development and implementation of small animal ^{19}F-MRI is outlined for a 9.4T MRI system. This work introduces and provides additional details for the pre-clinical imaging protocols utilized by this thesis.

In Chapter 3, the stem cell fate in two models of murine transplantation were investigated with ^{19}F-MRI. Validated with histology, this work shows that ^{19}F-MRI is a powerful tool for non-invasive, longitudinal imaging. This chapter was published in PLoS ONE (Gaudet et al. *Tracking the fate of stem cell implants with fluorine-19 MRI*. PLoS ONE. 2015 10(3):e0118544)

In Chapter 4, the natural immune response to a rejected transplant was imaged with dual cellular MRI agents. Immune cells were tracked following in situ labeling with iron oxide, while stem cells were monitored with ^{19}F-MRI. This chapter was published in the journal, Magnetic Resonance in Medicine (Gaudet et al. *Application of dual ^{19}F and iron cellular MRI agents to track the infiltration of immune cells to the site of a rejected stem cell transplant*. MRM. 2016)

In Chapter 5, a ^{19}F-cell tracking imaging protocol was developed for an upcoming phase 1 clinical trial. This trial will involve the administration of APCs intradermally into the upper thigh of prostate cancer patients. Imaging was validated at 3T with a porcine tissue phantom. Sections of this chapter are under review at PLoS ONE (Fink et al. *^{19}F-perfluorocarbon-labeled human peripheral blood mononuclear cells can be detected in vivo using clinical MRI parameters in a therapeutic cell setting*.)

1.6 References

1. Caplan AI. Mesenchymal stem cells. Journal of Orthopaedic Research. 1991;9(5):641–50.
2. Psaltis P, Zannettino A. Concise review: mesenchymal stromal cells: potential for cardiovascular repair. Stem Cells. 2008:2201–2210.
3. Quevedo HC, Hatzistergos KE, Oskouei BN, Feigenbaum GS, Rodriguez JE, Valdes D, Pattany PM, Zambrano JP, Hu Q, McNiece I, et al. Allogeneic mesenchymal stem cells restore cardiac function in chronic ischemic cardiomyopathy via trilineage differentiating capacity. Proceedings of the National Academy of Sciences of the United States of America. 2009;106(33):14022–7.
4. Meirelles L da S, Nardi NB. Methodology, biology and clinical applications of mesenchymal stem cells. Frontiers in Bioscience. 2009;14(6):4281–4298.
5. Chen J, Li Y, Wang L, Zhang Z, Lu D, Lu M, Chopp M. Therapeutic benefit of intravenous administration of bone marrow stromal cells after cerebral ischemia in rats. Stroke. 2001;32(4):1005–11.
6. Nedopil A, Klenk C, Kim C, Liu S, Wendland M, Schuster T, Sennino B, Mcdonald DM, Daldrup- HE. MR signal characteristics of viable and apoptotic human mesenchymal stem cells in MASI for treatment of osteoarthritis. Investigative radiology. 2010;45(10):634–640.
7. Keating A. Mesenchymal stromal cells: new directions. Cell Stem Cell. 2012;10(6):709–16.
8. Segers VFM, Lee RT. Stem-cell therapy for cardiac disease. Nature. 2008;451(7181):937–42.
9. Bianco P. “Mesenchymal” Stem Cells. Annual Review of Cell and Developmental Biology. 2014;30(1):677–704.
10. Trivanovic D, Krstic J, Djordjevic IO, Mojsilovic S, Santibanez JF, Bugarski D, Jaukovic A. The Roles of Mesenchymal Stromal/Stem Cells in Tumor Microenvironment Associated with Inflammation. Mediators of Inflammation. 2016;2016(Article ID 7314016):14.

11. Dominici M, Le Blanc K, Mueller I, Slaper-Cortenbach I, Marini F, Krause D, Deans R, Keating A, Prockop D, Horwitz E. Minimal criteria for defining multipotent mesenchymal stromal cells. The International Society for Cellular Therapy position statement. Cytotherapy. 2006;8(4):315–317.
12. Ankrum J a, Ong JF, Karp JM. Mesenchymal stem cells: immune evasive, not immune privileged. Nature biotechnology. 2014;32(3):252–60.
13. Kanno S, Wu YJ, Lee PC, Dodd SJ, Williams M, Griffith BP, Ho C. Macrophage accumulation associated with rat cardiac allograft rejection detected by magnetic resonance imaging with ultrasmall superparamagnetic iron oxide particles. Circulation. 2001;104(8):934–938.
14. Zhang Y, Dodd SJ, Hendrich KS, Williams M, Ho C. Magnetic resonance imaging detection of rat renal transplant rejection by monitoring macrophage infiltration. Kidney International. 2000;58(3):1300–1310.
15. Gollackner B, Goh SK, Qawi I, Buhler L, Knosalla C, Daniel S, Kaczmarek E, Awwad M, Cooper DKC, Robson SC. Acute Vascular Rejection of Xenografts: Roles of Natural and Elicited Xenoreactive Antibodies in Activation of Vascular Endothelial Cells and Induction of Procoagulant Activity. Transplantation. 2004;77(11):1735–1741.
16. Griffin MD, Ryan AE, Alagesan S, Lohan P, Treacy O, Ritter T. Anti-donor immune responses elicited by allogeneic mesenchymal stem cells: what have we learned so far? Immunology and cell biology. 2013;91(1):40–51.
17. Satyananda V, Hara H, Ezzelarab MB, Phelps C, Ayares D, Cooper DKC. New concepts of immune modulation in xenotransplantation. Transplantation. 2013;96(11):937–45.
18. Magil AB. Monocytes/macrophages in renal allograft rejection. Transplantation Reviews. 2009;23(4):199–208.
19. Murphy SP, Porrett PM, Turka L a. Innate immunity in transplant tolerance and rejection. Immunological reviews. 2011;241(1):39–48.
20. Bartholomew A, Sturgeon C, Siatskas M, Ferrer K, McIntosh K, Patil S, Hardy W, Devine S, Ucker D, Deans R, et al. Mesenchymal stem cells suppress lymphocyte proliferation in vitro and prolong skin graft survival in vivo. Experimental

Hematology. 2002;30(1):42–8.

21. Auchincloss H, Sachs DH. Xenogeneic transplantation. Annual review of immunology. 1998;16:433–470.
22. Melief CJM. Cancer Immunotherapy by Dendritic Cells. Immunity. 2008;29(3):372–383.
23. Fong L, Engleman EG. Dendritic Cells in cancer immunotherapy. Annual Review of Immunology. 2000;(18):245–273.
24. Lubaroff DM. Prostate cancer vaccines in clinical trials. Expert Review of Vaccines. 2012;11(7):857–68.
25. Hart D. Dendritic Cells: Unique Leukocyte populations which control the primary immune response. Blood. 1997;90(9):3245–3287.
26. Betjes MGH, Haks MC, Tuk CW, Beelen RHJ. Monoclonal Antibody EBM11 (Anti-CD68) Discriminates between Dendritic Cells and Macrophages after Short-Term Culture. Immunobiology. 1991;183(1):79–87.
27. Hsu FJ, Fagnoni F, BENIKE C, Liles TM, Czerwinski D, Taidi B, Engleman EG, Levy R. Vaccination of patients with B-cell lymphoma using autologous antigen-pulsed dendritic cells. Nature Medicine. 1996;2(1):52–58.
28. Radford KJ, Tullett KM, Lahoud MH. Dendritic cells and cancer immunotherapy. Current opinion in immunology. 2014;27(DC):26–32.
29. Westdorp H, Bol KF, Coskunturk M, Schreibelt G, Vries IJM De, Figdor CG. Dendritic Cell-based Cancer Vaccines. In: Britten CM, Kreiter S, Diken M, Rammensee H-G, editors. Cancer Immunotherapy Meets Oncology. Cham: Springer International Publishing; 2014. p. 71–87.
30. Small EJ, Schellhammer PF, Higano CS, Redfern CH, Nemunaitis JJ, Valone FH, Verjee SS, Jones L a, Hershberg RM. Placebo-controlled phase III trial of immunologic therapy with sipuleucel-T (APC8015) in patients with metastatic, asymptomatic hormone refractory prostate cancer. Journal of clinical oncology : official journal of the American Society of Clinical Oncology. 2006;24(19):3089–94.
31. Beer TM, Bernstein GT, Corman JM, Glode LM, Hall SJ, Poll WL, Schellhammer PF, Jones L a, Xu Y, Kylstra JW, et al. Randomized trial of autologous cellular

immunotherapy with sipuleucel-T in androgen-dependent prostate cancer. Clinical cancer research : an official journal of the American Association for Cancer Research. 2011;17(13):4558–67.

32. Graff JN, Chamberlain ED. Sipuleucel-T in the treatment of prostate cancer: an evidence-based review of its place in therapy. Core Evidence. 2015;10:1–10.
33. Brown R, Cheng Y, Haacke E, Thompson M, Venkatesan R. Magnetic Resonance Imaging: Physical Principles and Sequence Design, 2nd Ed. 2nd ed. John Wiley & Sons Ltd; 2014. i-xxxii.
34. McRobbie D, Moore E, Graves M, Prince M. MRI: From Picture to Proton. Radiology. 2004;232(2):474.
35. Scheffler K, Lehnhardt S. Principles and applications of balanced SSFP techniques. European Radiology. 2003;13(11):2409–18.
36. Bhosale P, Ma J, Choi H. Utility of the FIESTA pulse sequence in body oncologic imaging: review. American Journal of Roentgenology. 2009;192(6 Suppl):S83-93.
37. Heyn C, Bowen C V, Rutt BK, Foster PJ. Detection threshold of single SPIO-labeled cells with FIESTA. Magnetic Resonance in Medicine. 2005;53(2):312–20.
38. Ribot EJ, Foster PJ. In vivo MRI discrimination between live and lysed iron-labelled cells using balanced steady state free precession. European Radiology. 2012;22(9):2027–34.
39. Joo HT, Foster P, Rosales A, Feng B, Hasilo C, Martinez V, Ramadan S, Snir J, Melling CWJ, Dhanvantari S, et al. Imaging islets labeled with magnetic nanoparticles at 1.5 Tesla. Diabetes. 2006;55(11):2931–2938.
40. Liu W, Dahnke H, Rahmer J, Jordan EK, Frank JA. Ultrashort T2* relaxometry for quantitation of highly concentrated superparamagnetic iron oxide (SPIO) nanoparticle labeled cells. Magnetic Resonance in Medicine. 2009;61(4):761–766.
41. Liu W, Frank J a. Detection and quantification of magnetically labeled cells by cellular MRI. European Journal of Radiology. 2009;70(2):258–64.
42. Love Z, Wang F, Dennis JE, Awadallah A, Salem N, Lin Y, Weisenberger A, Majewski S, Gerson S, Lee Z. Imaging of mesenchymal stem cell transplant by bioluminescence and PET. Journal of nuclear medicine : official publication,

Society of Nuclear Medicine. 2007;48(12):2011–20.

43. Tennstaedt A, Aswendt M, Adamczak J, Hoehn M. Noninvasive Multimodal Imaging of Stem Cell Transplants in the Brain Using Bioluminescence Imaging and Magnetic Resonance Imaging. 2013;(June):153–166.
44. de Vries IJM, Lesterhuis WJ, Barentsz JO, Verdijk P, van Krieken JH, Boerman OC, Oyen WJG, Bonenkamp JJ, Boezeman JB, Adema GJ, et al. Magnetic resonance tracking of dendritic cells in melanoma patients for monitoring of cellular therapy. Nature Biotechnology. 2005;23(11):1407–13.
45. Saritas EU, Goodwill PW, Croft LR, Konkle JJ, Lu K, Zheng B, Conolly SM. Magnetic particle imaging (MPI) for NMR and MRI researchers. Journal of Magnetic Resonance. 2013;229:116–126.
46. Ahrens ET, Flores R, Xu H, Morel PA. In vivo imaging platform for tracking immunotherapeutic cells. Nature biotechnology. 2005;23(8):983–7.
47. Bulte JWM, Hoekstra Y, Kamman RL, Webb AG, Briggs RW, Go KG, Hulstaert CE, Mitenyi S, T.H. T, Leij LD. Specific MR imaging of human lymphocytes by monoclonal antibody-guided dextran-magnetite particles. Magnetic Resonance in Medicine. 1992;25(1):1489157.
48. Yeh T c., Zhang W, Ildstad ST, Ho C. Intracellular labeling of t-cells with super paramagnetic contrast agents. Magnetic Resonance in Medicine. 1993;30(5):617–625.
49. Bulte JWM, Ma L, Magin RL, Kamman RL, Hulstaert CE, Go KG, The TH, de Leij L. Selective MR imaging of labeled human peripheral blood mononuclear cells by liposome mediated incorporation of dextran-magnetite particles. Magnetic Resonance in Medicne. 1993;29(1):32–37.
50. Shapiro EM, Sharer K, Skrtic S, Koretsky AP. In vivo detection of single cells by MRI. Magnetic Resonance in Medicine. 2006;55(2):242–9.
51. Rohani R, de Chickera SN, Willert C, Chen Y, Dekaban G a, Foster PJ. In vivo cellular MRI of dendritic cell migration using micrometer-sized iron oxide (MPIO) particles. Molecular imaging and biology : MIB : the official publication of the Academy of Molecular Imaging. 2011;13(4):679–94.
52. de Chickera SN, Snir J, Willert C, Rohani R, Foley R, Foster PJ, Dekaban G a.

Labelling dendritic cells with SPIO has implications for their subsequent in vivo migration as assessed with cellular MRI. Contrast media & molecular imaging. 2011;6(4):314–27.

53. Khurana a., Nejadnik H, Gawande R, Lin G, Lee S, Messing S, Castaneda R, Derugin N, Pisani L, Lue TF, et al. Intravenous Ferumoxytol Allows Noninvasive MR Imaging Monitoring of Macrophage Migration into Stem Cell Transplants. Radiology. 2012;264(3):803–811.
54. Mallett CL, McFadden C, Chen Y, Foster PJ. Migration of iron-labeled KHYG-1 natural killer cells to subcutaneous tumors in nude mice, as detected by magnetic resonance imaging. Cytotherapy. 2012;14(6):743–51.
55. Noad J, Gonzalez-Lara LE, Broughton HC, McFadden C, Chen Y, Hess D a, Foster PJ. MRI tracking of transplanted iron-labeled mesenchymal stromal cells in an immune-compromised mouse model of critical limb ischemia. NMR in Biomedicine. 2013;26(4):458–67.
56. Ribot EJ, Gaudet JM, Chen Y, Gilbert KM, Foster PJ. In vivo MR detection of fluorine-labeled human MSC using the bSSFP sequence. International Journal of Nanomedicine. 2014;9:1731–9.
57. Gonzalez-Lara LE, Xu X, Hofstetrova K, Pniak A, Chen Y, McFadden CD, Martinez-Santiesteban FM, Rutt BK, Brown A, Foster PJ. The use of cellular magnetic resonance imaging to track the fate of iron-labeled multipotent stromal cells after direct transplantation in a mouse model of spinal cord injury. Molecular Imaging and Biology. 2011;13(4):702–11.
58. Heyn C, Ronald J a, Ramadan SS, Snir J, Barry AM, MacKenzie LT, Mikulis DJ, Palmieri D, Bronder JL, Steeg PS, et al. In vivo MRI of cancer cell fate at the single-cell level in a mouse model of breast cancer metastasis to the brain. Magnetic resonance in medicine : official journal of the Society of Magnetic Resonance in Medicine / Society of Magnetic Resonance in Medicine. 2006;56(5):1001–10.
59. Ribot EJ, Martinez-Santiesteban FM, Simedrea C, Steeg PS, Chambers AF, Rutt BK, Foster PJ. In vivo single scan detection of both iron-labeled cells and breast cancer metastases in the mouse brain using balanced steady-state free precession

imaging at 1.5 T. Journal of Magnetic Resonance Imaging. 2011;34(1):231–8.

60. Economopoulos V, Chen Y, McFadden CD, Foster PJ. MRI Detection of Nonproliferative Tumor Cells in Lymph Node Metastases Using Iron Oxide Particles in a Mouse Model of Breast Cancer. Translational Oncology. 2013;6(3):347–354.
61. Toso C, Vallee JP, Morel P, Ris F, Demuylder-Mischler S, Lepetit-Coiffe M, Marangon N, Saudek F, James Shapiro AM, Bosco D, et al. Clinical magnetic resonance imaging of pancreatic islet grafts after iron nanoparticle labeling. American Journal of Transplantation. 2008;8(3):701–706.
62. Wolfs E, Struys T, Notelaers T, Roberts SJ, Sohni A, Bormans G, Van Laere K, Luyten FP, Gheysens O, Lambrichts I, et al. 18F-FDG labeling of mesenchymal stem cells and multipotent adult progenitor cells for PET imaging: effects on ultrastructure and differentiation capacity. Journal of Nuclear Medicine. 2013;54(3):447–54.
63. Stojanov K, De Vries EFJ, Hoekstra D, Van Waarde A, Dierckx RAJO, Zuhorn IS. [18F]FDG labeling of neural stem cells for in vivo cell tracking with positron emission tomography: Inhibition of tracer release by phloretin. Molecular Imaging. 2012;11(1):1–12.
64. de Vries IJM, Lesterhuis WJ, Barentsz JO, Verdijk P, van Krieken JH, Boerman OC, Oyen WJG, Bonenkamp JJ, Boezeman JB, Adema GJ, et al. Magnetic resonance tracking of dendritic cells in melanoma patients for monitoring of cellular therapy. Nature biotechnology. 2005;23(11):1407–13.
65. Muja N, Bulte JWM. Magnetic resonance imaging of cells in experimental disease models. Progress in nuclear magnetic resonance spectroscopy. 2009;55(1):61–77.
66. Zheng B, Vazin T, Goodwill PW, Conway A, Verma A, Ulku Saritas E, Schaffer D, Conolly SM. Magnetic Particle Imaging tracks the long-term fate of in vivo neural cell implants with high image contrast. Scientific Reports. 2015;5(August):14055.
67. Hundt W, Schink C, Steinbach S, O’Connell-Rodwell CE, Mayer D, Burbelko M, Kießling A, Guccione S. Use of in vivo bioluminescence and MRI to determine hyperthermia-induced changes in luciferase activity under the control of an hsp70 promoter. NMR in Biomedicine. 2012;25(12):1378–91.

68. Deans AE, Wadghiri YZ, Bernas LM, Yu X, Rutt BK, Turnbull DH. Cellular MRI contrast via coexpression of transferrin receptor and ferritin. Magnetic Resonance in Medicine. 2006;56(1):51–59.
69. Bulte JW, Douglas T, Witwer B, Zhang SC, Strable E, Lewis BK, Zywicke H, Miller B, van Gelderen P, Moskowitz BM, et al. Magnetodendrimers allow endosomal magnetic labeling and in vivo tracking of stem cells. Nature Biotechnology. 2001;19(12):1141–7.
70. Shapiro EM, Koretsky AP. Micron-sized iron oxide particles (MPIOs) for Cellular Imaging: More bang for the buck. In: Bulte JWM, Modo MM., editors. Nanoparticles in Biomedical Imaging. Vol. 102. Springer New York; 2008. p. 141–161.
71. Korchinski DJ, Taha M, Yang R, Nathoo N, Dunn JF. Iron Oxide as an MRI Contrast Agent for Cell Tracking. Magnetic resonance insights. 2015;8(Suppl 1):15–29.
72. Conner SD, Schmid SL. Regulated portals of enrty into the cell. Nature. 2003;422(March):37–43.
73. Amsalem Y, Mardor Y, Feinberg MS, Landa N, Miller L, Daniels D, Ocherashvilli A, Holbova R, Yosef O, Barbash IM, et al. Iron-oxide labeling and outcome of transplanted mesenchymal stem cells in the infarcted myocardium. Circulation. 2007;116(11 SUPPL. 1):38–46.
74. Bonner F, Merx MW, Klingel K, Begovatz P, Flogel U, Sager M, Temme S, Jacoby C, Salehi Ravesh M, Grapentin C, et al. Monocyte imaging after myocardial infarction with 19F MRI at 3 T: a pilot study in explanted porcine hearts. European Heart Journal - Cardiovascular Imaging. 2015:1–9.
75. Flögel U, Ding Z, Hardung H, Jander S, Reichmann G, Jacoby C, Schubert R, Schrader J. In vivo monitoring of inflammation after cardiac and cerebral ischemia by fluorine magnetic resonance imaging. Circulation. 2008;118(2):140–8.
76. Deddens LH, Van Tilborg G a F, Mulder WJM, De Vries HE, Dijkhuizen RM. Imaging neuroinflammation after stroke: current status of cellular and molecular MRI strategies. Cerebrovascular diseases (Basel, Switzerland). 2012;33(4):392–402.

77. Wu Y, Ye Q, Eytan DF, Liu L, Rosario BL, Hitchens TK, Yeh F-C, van Rooijen N, Ho C. MRI Investigation of Macrophjages in acute cardiac allograft rejection after heart transplantation. Circulation: Cardiovascular Imaging. 2011;72(2):181–204.
78. Daldrup-Link HE, Golovko D, Ruffell B, DeNardo DG, Castaneda R, Ansari C, Rao J, Tikhomirov GA, Wendland MF, Corot C, et al. MRI of tumor-associated macrophages with clinically applicable iron oxide nanoparticles. Clinical Cancer Research. 2011;17(17):5695–5704.
79. Shih Y-YI, Hsu Y-H, Duong TQ, Lin S-S, Chow K-PN, Chang C. Longitudinal study of tumor-associated macrophages during tumor expansion using MRI. NMR in biomedicine. 2011;24(10):1353–60.
80. Dunn EA, Weaver LC, Dekaban GA, Foster PJ. Cellular imaging of inflammation after experimental spinal cord injury. Molecular Imaging. 2005;4(1):53–62.
81. Gorter C, Broer LJ. Negative result of an attempt to observe nuclear magnetic resonance in solids. Physica. 1942;9(6):591–596.
82. Holland G., Bottomley P., Hinshaw W. 19F magnetic resonance imaging. Journal of Magnetic Resonance (1969). 1977;28(1):133–136.
83. Tran HT, Guo QZ, Schumacher DJ, Burton RB, Mattrey RF. F-19 Chemical-Shift Imaging Technique to Measure Intracellular Po(2) in-Vivo Using Perflubron. Academic Radiology. 1995;2(9):756–761.
84. Anderson CM, Brown JJ, Balfe DM, Heiken JP, Borrello JA, Clouse RE, Pilgram TK. MR imaging of crohn disease: Use of perflubron as a gastrointestinal contrast agent. Journal of Magnetic Resonance Imaging. 1994;4(3):491–496.
85. Srinivas M, Morel PA, Ernst L a, Laidlaw DH, Ahrens ET. Fluorine-19 MRI for visualization and quantification of cell migration in a diabetes model. Magnetic Resonance in Medicine. 2007;58(4):725–34.
86. Colotti R, Bastiaansen JAM, Wilson A, Flögel U, Gonzales C, Schwitter J, Stuber M, van Heeswijk RB. Characterization of perfluorocarbon relaxation times and their influence on the optimization of fluorine-19 MRI at 3 Tesla. Magnetic Resonance in Medicine. 2016;[Epup ahea.
87. Fox MS, Gaudet JM, Foster PJ. Fluorine-19 MRI Contrast Agents for Cell Tracking and Lung Imaging. 2015;8:1–15.

88. Keupp J, Rahmer J, Grässlin I, Mazurkewitz PC, Schaeffter T, Lanza GM, Wickline S a, Caruthers SD. Simultaneous dual-nuclei imaging for motion corrected detection and quantification of 19F imaging agents. Magnetic resonance in medicine : official journal of the Society of Magnetic Resonance in Medicine / Society of Magnetic Resonance in Medicine. 2011;66(4):1116–22.
89. Otake Y, Soutome Y, Hirata K, Ochi H, Bito Y. Double-tuned Radiofrequency Coil for 19F and 1H Imaging. Magnetic Resonance in Medical Sciences. 2014;[Epub].
90. Ji Y, Waiczies H, Winter L, Neumanova P, Hofmann D, Rieger J, Mekle R, Waiczies S, Niendorf T. Eight-channel transceiver RF coil array tailored for 1 H/ 19 F MR of the human knee and fluorinated drugs at 7.0 T. NMR in Biomedicine. 2015;28:726–737.
91. Kampf T, Fischer a, Basse-Lüsebrink TC, Ladewig G, Breuer F, Stoll G, Jakob PM, Bauer WR. Application of compressed sensing to in vivo 3D ^{19}F CSI. Journal of magnetic resonance (San Diego, Calif. : 1997). 2010;207(2):262–73.
92. Zhong J, Mills PH, Hitchens TK, Ahrens ET. Accelerated fluorine-19 MRI cell tracking using compressed sensing. Magnetic resonance in medicine : official journal of the Society of Magnetic Resonance in Medicine / Society of Magnetic Resonance in Medicine. 2012;0:1–8.
93. Meissner M, Reisert M, Hugger T, Hennig J, von Elverfeldt D, Leupold J. Revealing signal from noisy (19) F MR images by chemical shift artifact correction. Magnetic Resonance in Medicine. 2014;0:1–9.
94. Goette MJ, Lanza GM, Caruthers SD, Wickline S a. Improved quantitative (19) F MR molecular imaging with flip angle calibration and B1 -mapping compensation. Journal of Magnetic Resonance Imaging. 2014 Nov 25:1–7.
95. Partlow KC, Chen J, Brant J a, Neubauer AM, Meyerrose TE, Creer MH, Nolta J a, Caruthers SD, Lanza GM, Wickline S a. 19F magnetic resonance imaging for stem/progenitor cell tracking with multiple unique perfluorocarbon nanobeacons. The FASEB Journal. 2007;21(8):1647–54.
96. Ruiz-Cabello J, Walczak P, Kedziorek D a, Chacko VP, Schmieder AH, Wickline S a, Lanza GM, Bulte JWM. In vivo “hot spot” MR imaging of neural stem cells using fluorinated nanoparticles. Magnetic Resonance in Medicine.

2008;60(6):1506–11.

97. Helfer BBM, Balducci A, Nelson AD, Janjic JM, Gil RR, Kalinski P, Vries IJMDE, Ahrens ET, Mailliard RB, de Vries IJM. Functional assessment of human dendritic cells labeled for in vivo (19)F magnetic resonance imaging cell tracking. Cytotherapy. 2010;12(2):238–50.
98. Bonetto F, Srinivas M, Weigelin B, Cruz LJ, Heerschap A, Friedl P, Figdor CG, Vries IJM De. A large-scale (19)F MRI-based cell migration assay to optimize cell therapy. NMR in biomedicine. 2012;25(9):1095–103.
99. Bouchlaka MN, Ludwig KD, Gordon JW, Kutz MP, Bednarz BP, Fain SB, Capitini CM. 19 F-MRI for monitoring human NK cells in vivo. OncoImmunology. 2016;5(5).
100. Srinivas M, Turner MS, Morel P a, Janjic JM, Laidlaw DH, Ahrens ET. In vivo cytometry of antigen-specific T cells using 19F MRI. Magnetic Resonance in Medicine. 2009;62:747–753.
101. Waiczies H, Lepore S, Janitzek N, Hagen U, Seifert F, Ittermann B, Purfürst B, Pezzutto A, Paul F, Niendorf T, et al. Perfluorocarbon particle size influences magnetic resonance signal and immunological properties of dendritic cells. PloS one. 2011;6(7):e21981.
102. Bonetto F, Srinivas M, Heerschap A, Mailliard R, Ahrens ET, Figdor CG, de Vries IJM, Vries IJM De. A novel (19)F agent for detection and quantification of human dendritic cells using magnetic resonance imaging. International journal of cancer. Journal international du cancer. 2011;129(2):365–73.
103. Helfer BM, Balducci A, Sadeghi Z, O'Hanlon C, Hijaz A, Flask C a, Wesa AK. (19)F MRI tracer preserves in vitro and in vivo properties of hematopoietic stem cells. Cell transplantation. 2013;22(1):87–97.
104. Ahrens ET, Young W, Xu H, Pusateri LK. Reports Rapid quantification of inflammation in tissue samples using perfluorocarbon emulsion and fluorine-19 nuclear magnetic resonance. BioTechniques Focus:Translational Tools. 2011:229–234.
105. Basse-Lusebrink TC, Weise G, Stoll G. Imaging of inflammation in the peripheral nervous system by 19 F MRI. 2011;19:3710.

106. Jacoby C, Temme S, Mayenfels F, Benoit N, Krafft MP, Schubert R, Schrader J, Flögel U. Probing different perfluorocarbons for in vivo inflammation imaging by (19) F MRI: image reconstruction, biological half-lives and sensitivity. NMR in Biomedicine. 2014;27(3):261–71.

107. Hitchens TK, Ye Q, Eytan DF, Janjic JM, Ahrens ET, Ho C. 19F MRI detection of acute allograft rejection with in vivo perfluorocarbon labeling of immune cells. Magnetic resonance in medicine. 2011;65(4):1144–53.

108. Balducci A, Helfer BM, Ahrens ET, Iii CFOH, Wesa AK. Visualizing arthritic inflammation and therapeutic response by fluorine-19 magnetic resonance imaging (19 F MRI). Journal of Inflammation. 2012;9(1):1.

109. O'Hagan D. Understanding organofluorine chemistry. An introduction to the C-F bond. Chemical Society reviews. 2008;37(2):308–19.

110. Mitsuno T, Ohyanagi H, Naito R. Clinical studies of a perfluorochemical whole blood substitute (Fluosol-DA) Summary of 186 cases. Annals of Surgery. 1982;195(1):60–9.

111. Hume DA. The mononuclear phagocyte system. Current Opinion in Immunology. 2006;18(1):49–53.

112. Ahrens ET, Helfer BM, O'Hanlon CF, Schirda C. Clinical cell therapy imaging using a perfluorocarbon tracer and fluorine-19 MRI. Magnetic Resonance in Medicine. 2014;72:1696–1701.

113. Kadayakkara DK, Damodaran K, Hitchens TK, Bulte JWM, Ahrens ET. (19)F spin-lattice relaxation of perfluoropolyethers: Dependence on temperature and magnetic field strength (7.0-14.1T). Journal of magnetic resonance (San Diego, Calif. : 1997). 2014;242C:18–22.

114. Bible E, Dell'Acqua F, Solanky B, Ahrens ET. Non-invasive imaging of transplanted human neural stem cells and ECM scaffold remodeling in the stroke-damaged rat brain by 19 F- and diffusion-MRI. Biomaterials. 2012.

115. Boehm-Sturm P, Mengler L, Wecker S, Hoehn M, Kallur T. In Vivo Tracking of Human Neural Stem Cells with 19F Magnetic Resonance Imaging. PloS ONE. 2011;6(12):e29040.

116. Dewitte H, Geers B, Liang S, Himmelreich U, Demeester J, De Smedt SC,

Lentacker I. Design and Evaluation of Theranostic Perfluorocarbon Particles for Simultaneous Antigen-loading and (19)F-MRI Tracking of Dendritic Cells. Journal of Controlled Release. 2013;169(1–2):141–149.

Chapter 2

2 Optimization of Preclinical ^{19}F-imaging Techniques

As the first ^{19}F-MRI cell tracking site in Canada, a number of parameters and protocols required development and optimization prior to beginning animal studies. This chapter provides additional details on the methods utilized in the following chapters for ^{19}F acquisition, with a focus on minimum detection limit and quantification accuracy.

2.1 Equipment

Pre-clinical imaging was performed on a 9.4T Varian/Agilent small animal scanner. The high-field system provides a number of advantages for ^{19}F detection. As discussed in Chapter 1, net magnetization increases with the field strength, so a 9.4T system provides more than 6x the signal of a clinical 1.5T MRI. In addition, the smaller bore size provides more accurate shimming and allows for stronger gradient slew rates at small animal sizes. All of these factors contribute to higher resolution and improved image quality in murine images compared to a clinical MRI system. A ^{19}F/^{1}H dual-tuned birdcage volume coil, tuned to 376. MHz and 400.2MHz respectively, was produced in house by Kyle Gilbert. The volume coil has a 2.2cm diameter and 5.1 cm length, and is shown in Figure 3A, alongside the B_1 map (Fig 3B). The relatively uniform B_1 field at the center of the coil provides more accurate cell quantification, further discussed in Section 2.3. Coil diameter was kept as small as possible for murine imaging to optimize sensitivity.

2.2 MRI Acquisition Parameters

2.2.1 Pulse Sequence

Overall, the vast majority of ^{19}F-MRI studies have employed spin echo sequences.[1] As of 2012, only a single study had utilized bSSFP for ^{19}F-cell tracking of pre-labeled cells.[2] Since then, the high signal-per-unit time advantage bSSFP provides has been used in numerous studies to investigate ^{19}F-labeled MSC,[3] NK cells,[4] stromal vascular fraction

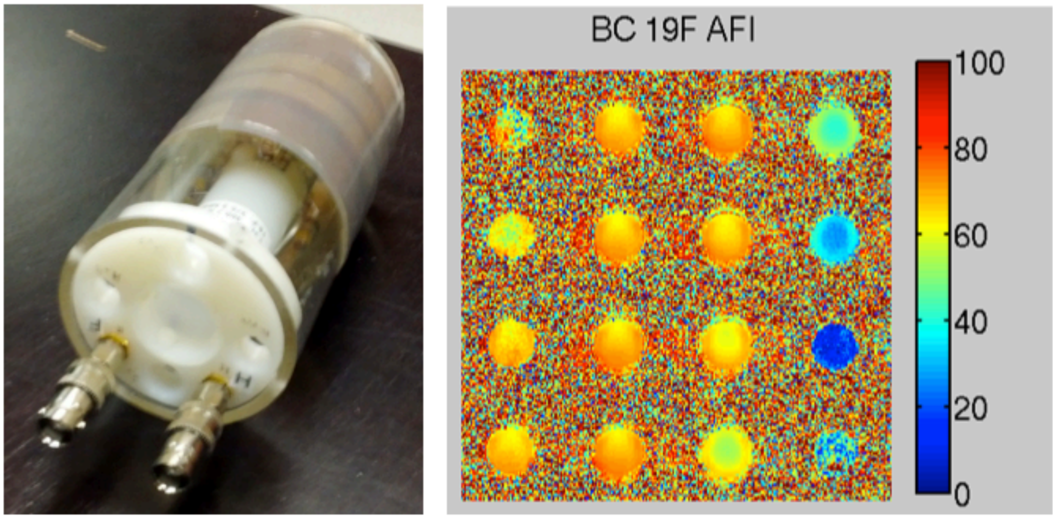

Figure 3: (A) Image of the dual tuned birdcage volume coil. The tuning frequency is controlled by driving through one of the two coaxial cable connectors. (B) The Actual Flip angle Image (AFI) shows the field uniformity in the center of the ^{19}F birdcage coil, with each circle representing a 5mm axial slice. The scale on the right indicates the actual flip angle applied to the same following application of a 90^o pulse.

cells,[5] and inflammatory cells.[6] Expanding on Section 1.3.3, bSSFP has additional advantages for multi-nuclear imaging compared to conventional sequences.[7,8] The short imaging repetition time (around 4ms) allows for 100s of imaging averages to be performed in a reasonable scan time. The high SNR produced improves detection sensitivity, but can also be traded off to allow for higher resolution, an advantage that is outlined in more detail in Section 2.2.2. When TR= 2*TE bSSFP images are not influenced by T_2*, despite being formed by a gradient echo-like sequence. This is an important factor when considering quantification accuracy, since it relies on the assumption that image contrast is constant across the image.[9,10] Finally, PFC agents tend to have relatively similar T_1 and T_2 values, providing the optimum steady state magnetization as given by Equation 4.[1,10] All of these factors, as well as the extensive literature on iron cell tracking with bSSFP,[11–15] influenced our decision to use the bSSFP sequence for this thesis. To date SSFP-based pulse sequences have shown the best ^{19}F sensitivity, with only ultra-short echo time (UTE)-SSFP producing higher signal then bSSFP.[8]

2.2.2 ^{19}F Image Resolution

In general, SNR is expected to increase with larger voxel size. This is due to the fact that with conventional proton imaging, larger voxels contain more hydrogen nuclei, generating higher signal. However, with ^{19}F-MRI cell tracking, larger voxels do not always lead to an increased SNR. This is predominately due to the fact that voxel size is already orders of magnitude larger than the area taken up by the injected cells *in vivo*. In this case, an increase in voxel size does not result in improved signal, since there are no additional ^{19}F nuclei to excite in the surrounding area. Instead, when field of view is kept constant, larger voxels tend to decrease SNR due to increased under-sampling artifact. An example of this is shown in Figure 4, where detection of 20,000 cells in 2mm^3 voxels (Fig 4A) is compared to 12mm^3 (Fig 4B). Overall though, voxel size does need to remain large compared to proton imaging to maintain sufficient ^{19}F atoms/voxel.

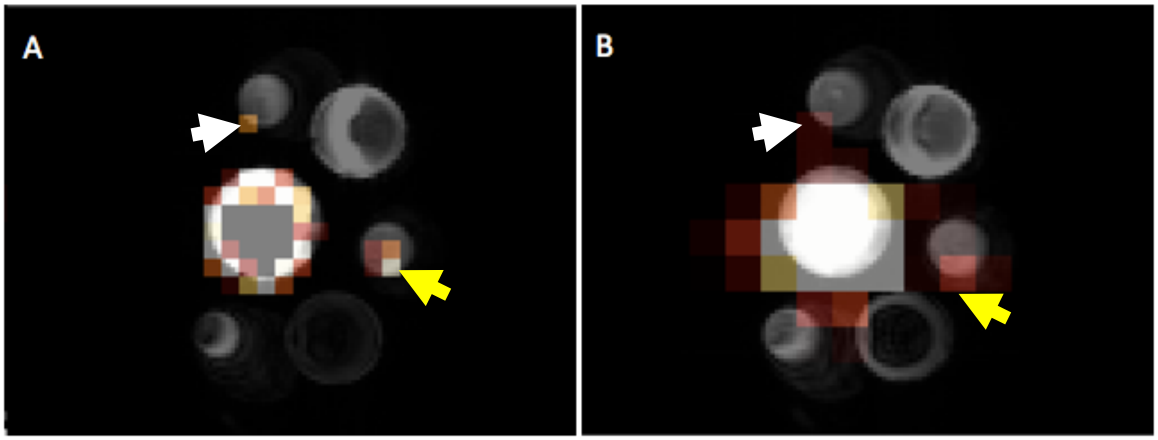

Figure 4: Cell pellets containing 20,000 (white arrow) and 60,000 (yellow arrow) cells. (A) SNR and image quality is higher, and quantification was found to be more accurate at 2mm^3 resolution, compared to (B) 12mm^3 voxels.

2.3 Quantification of Labeled Cells

2.3.1 Theory

Since signal produced by nuclear magnetic resonance is dependent on the number of nuclei per voxel, it is inherently quantitative. Non-invasive, in vivo quantification of ^{19}F-labeled cells was first described in 2010, by Srinivas et al.[16] The basic procedure is outlined in Figure 5. The first step towards quantification involves determining the intracellular ^{19}F uptake, or mean fluorine content per cell (Fc). Following *in vitro* ^{19}F-labeling of the cells, a sample containing a known number of cells is set aside for NMR analysis (process 1). Samples were analyzed at the University of Western Ontario Chemistry NMR facility with a Mercury VS 400MHz vertical bore magnet. Prior to spectroscopy, the NMR cell sample is suspended in D_2O and combined with 100µL of 0.1% trifluoracetic acid (TFA). Each TFA molecule has three identical fluorine atoms, producing a single NMR spectrum peak at -76ppm. Using this information, Fc can be determined by comparing the ratios of the NMR peak integral between TFA and the cell sample. This calculation is shown in Equations 6-8.

$$\#\,19F\ in\ TFA = \frac{(Area\ of\ TFA\ peak)}{3(moles\ of\ TFA)(N_A)} \qquad \text{(eq.6)}$$

$$Total\ \#\,19F\ in\ cells = \frac{(Area\ of\ PFC\ peak)}{(\#19F\ in\ TFA)} \qquad \text{(eq.7)}$$

$$Fc = \frac{(Total\ \#19F\ in\ cells)}{(\#\ of\ cells)} \qquad \text{(eq.8)}$$

The second process determines the number of ^{19}F atoms present at the region of interest within the animal. Imaging is performed alongside a reference tube of known concentration containing the same ^{19}F Cell Sense agent. By comparing the signal ratios of these two locations, the number of ^{19}F atoms at the ROI can be determined, as shown in Equation 8.

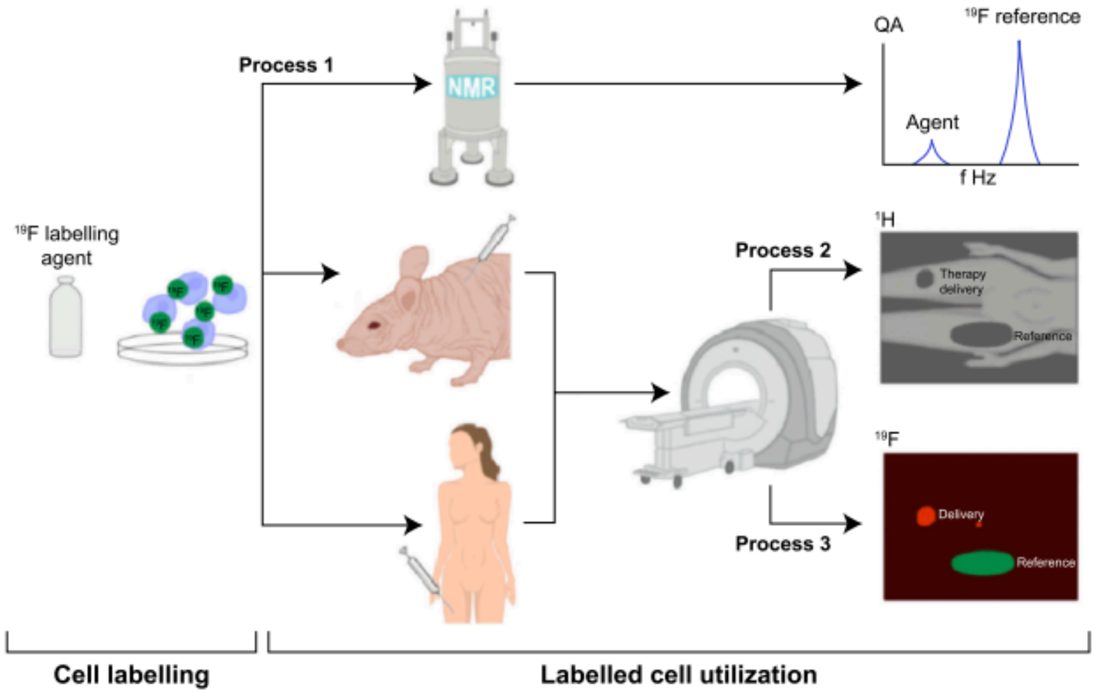
^{19}F labelling agent
Process 1
NMR
QA
^{19}F reference
Agent
f Hz
^{1}H
Process 2
Therapy delivery
Reference
^{19}F
Delivery
Reference
Process 3
Cell labelling
Labelled cell utilization

Figure 5: In vivo quantification can be performed when labeling cells in culture prior to their administration. Cells are labeled through co-incubation with a ^{19}F-agent overnight to allow for ^{19}F-spins to become internalized within cells. Labeled cells are then split into two separate pellets. The first pellet undergoes process 1, where NMR is used to determine the mean intracellular ^{19}F uptake. The second pellet is administered into the host, either a pre-clinical model or a patient. Process 2 involves conventional ^{1}H imaging of the host to provide the high resolution anatomical images. Then without moving the patient, ^{19}F imaging is performed over the same field of view in process 3. These two images can be overlaid for anatomical context of the ^{19}F signal. An external reference tube of known concentration is imaged alongside the host allowing for the signal from the labeled cells to be converted to number of ^{19}F atoms. By combining this information with the NMR data, the number of cells can be quantified

$$19F\ at\ ROI = (19F\ in\ Reference)\frac{(Signal\ ROI)}{(Signal\ at\ Reference)} \qquad \text{(eq.8)}$$

Finally, by combining Equations 7 and 8 it is possible to determine the number of labeled cells present at the ROI, Equation 9.

$$\#\ Cells\ at\ ROI = \frac{(19F\ at\ ROI)}{(Fc)} \qquad \text{(eq.9)}$$

2.3.2 Improving Quantification Accuracy

Calculations were performed using Voxeltracker software provided by CelSense Inc.[17] This imaging software simplifies the process by measuring signal and volume from hand-drawn ROIs and provides an estimation of quantification error from the image noise. Initially, quantification accuracy was poor, displayed in Figure 6 as the error multiple from the expected number of cells on a log-scale. The software automatically applies a Rician noise correction to improve accuracy. Unfortunately, this noise correction assumes the minimum noise distribution starts at 0. This assumption is often incorrect as all voxels were found to contain some noise signal, as shown in Figure 6B. By subtracting a constant signal value (x) from all voxels, the distribution can be left shifted back to the origin (Fig 6C). This step significantly improved quantification accuracy between unadjusted (Voxeltracker) and subtracted data sets, as shown by Figure 6C. Simplifying the data set by converting to 8-bit was also investigated, which inadvertently left-shifted some datasets improving accuracy. However, information lost by restricting to 256 bins hindered the robustness of the technique.

Further improvements were made to NMR accuracy by lysing cells to release the ^{19}F agent prior to NMR. Without lysis, cells would sediment towards the bottom of the NMR tube, resulting in a non-uniform suspension and reducing the accuracy of the measurement.

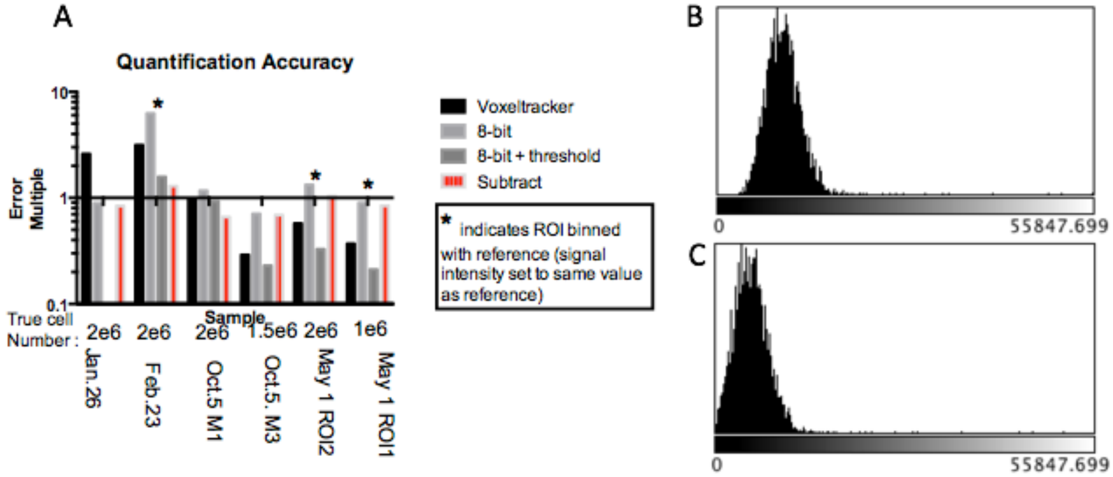

Figure 6: (A) Quantification error from six experiments is expressed as an error multiple from the true value of 1 on a logarithmic graph. The black bars indicate quantification error from raw un-adjusted data sets. (B) An image histogram of this data reveals that all voxels contain some signal value, an assumption that is not taken into account by the quantification software. (C) Improved quantification accuracy is obtained by left-shifting the histogram by subtracting a fixed value, equal to that of the lowest signal voxel, from all voxels as shown in the red bars.

Besides the methods described, ^{19}F-MRI quantification has been demonstrated numerous times in the literature with custom MATLAB scripts allowing for improved noise corrections and automated thresholding.[6,18–22] Extensive work has also been performed with MR spectroscopy to improve the accuracy and sensitivity of quantification, at the cost of image resolution.[23–27]

Ultimately, a number of factors contribute to quantification error. These include acquisition specific, such as: T_1 and T_2 differences between intracellular label and external reference tubes, error in power calibration due to the lower ^{19}F signal, B_o/B_1 field inhomogeneities; and at the cellular level, such as: uncertainty in cell number for NMR, inaccuracy in injection number, and distribution of label uptake. For longitudinal imaging, bystander labeling of native, non-targeted phagocytic cells provides the largest source of error, which is explored in more detail in chapters 3 and 4.

2.4 ^{19}F-Uptake

The labeling efficiency, or amount of ^{19}F per cell, is extremely important in determining the minimum number of detectable cells due to the fact that NMR signal is directly related to the number of nuclei within the voxel. For example, 10,000 cells containing $1\text{x}10^{12}$ ^{19}F atoms/cell produces the same signal as 1,000,000 cells containing $1\text{x}10^{10}$ ^{19}F atoms/cell. We observed intracellular uptake to be highly variable amongst cell batches, even in the controlled *in vitro* environment. The labeling variability is over orders of magnitude, as highlighted in Figure 7A, with each point indicating an experiment repetition. Uptake is influenced by the cell type, cell size, phagocytic potential, and donor health, as well as the physical and chemical properties of the ^{19}F agent itself. The Cell Sense (CS-1000) incubation concentration also influences the labeling efficiency (Fig 7B), but results in a decrease in viability at higher concentrations.

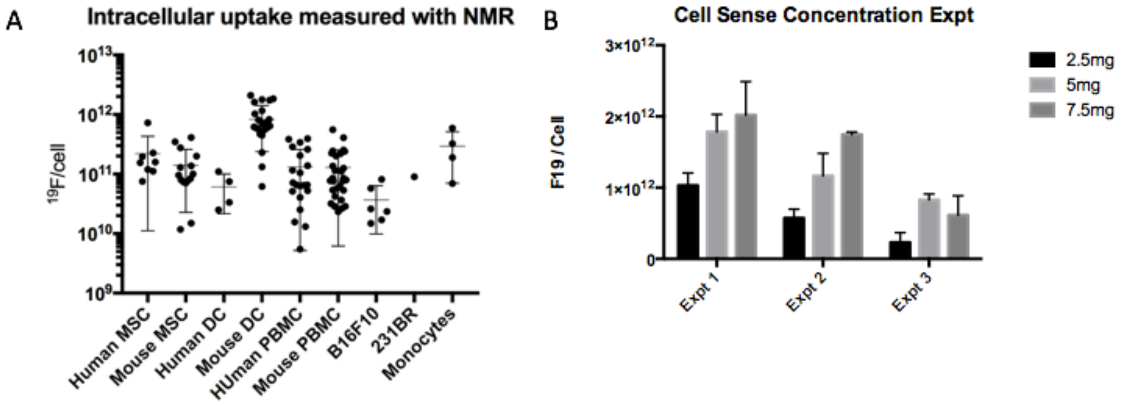

Figure 7: (A) Number of mean ^{19}F atoms per cell as measured by NMR was observed to vary by over two orders of magnitude within cell samples. Each data point represents cells prepared for a unique experiment. We found cells from older subjects tended to label less efficiently, in comparison to cells from younger subjects and culture. (B) Incubation concentration of the ^{19}F-agent Cell Sense also influenced cellular uptake. However, at 7.5mg the cell viability was observed to decrease (data not shown).

2.5 Anesthesia

In order to reduce animal motion and stress most pre-clinical imaging relies on anesthetized animals. Isoflurane is the most common veterinary anesthesia in use, due to: the high tolerance, ease of administration through inhalation, flexibility of dosage, and availability. However, due to the presence of ^{19}F atoms, this anesthetic can produce unwanted ^{19}F-MRI signal[3,28] unless appropriate precautions are taken. Figure 8 presents the chemical structure of isoflurane alongside the ^{19}F NMR spectrum from an anesthetized animal containing Cell Sense labeled cells.

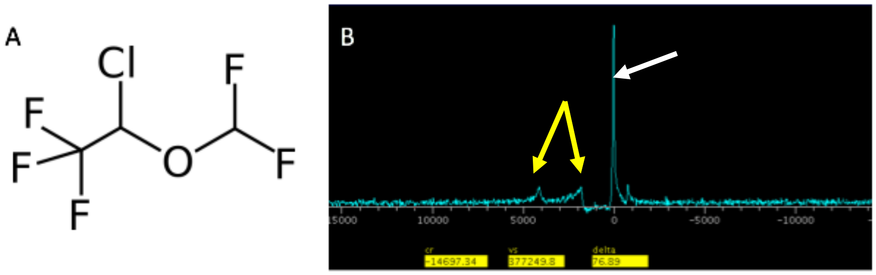

Figure 8: Each isoflurane molecule contains five ^{19}F atoms (A). They are visible in the *in vivo* ^{19}F spectrum of an anesthetized mouse (B, yellow arrow). Here the main CS-1000 peak is visible centered at 0 Hz (white arrow) [-91.5ppm], along with two isoflurane peaks [-86ppm and -81ppm].

In vivo, isoflurane accumulates in fat with a fat/blood ratio of 45.[29] This is visible in ^{19}F-MRI images of a mouse (Fig 9A), imaged alongside a reference tube containing Cell Sense. Imaging was performed centered at the Cell Sense frequency, resulting in a spatial shift in the isoflurane signal from the fat pad. Here the default truncated sinc excitation pulse was used (Fig 9B). Excitation of the isoflurane signal can be prevented with a longer, un-truncated sinc pulse (Fig 9C&D). Following fourier transform; the longer sinc pulse translates into a narrower rectangular excitation band in frequency space. When centered on the Cell Sense frequency, this band is narrow enough to not excite the nearby isoflurane peaks. We used this approach for all of our animal imaging.

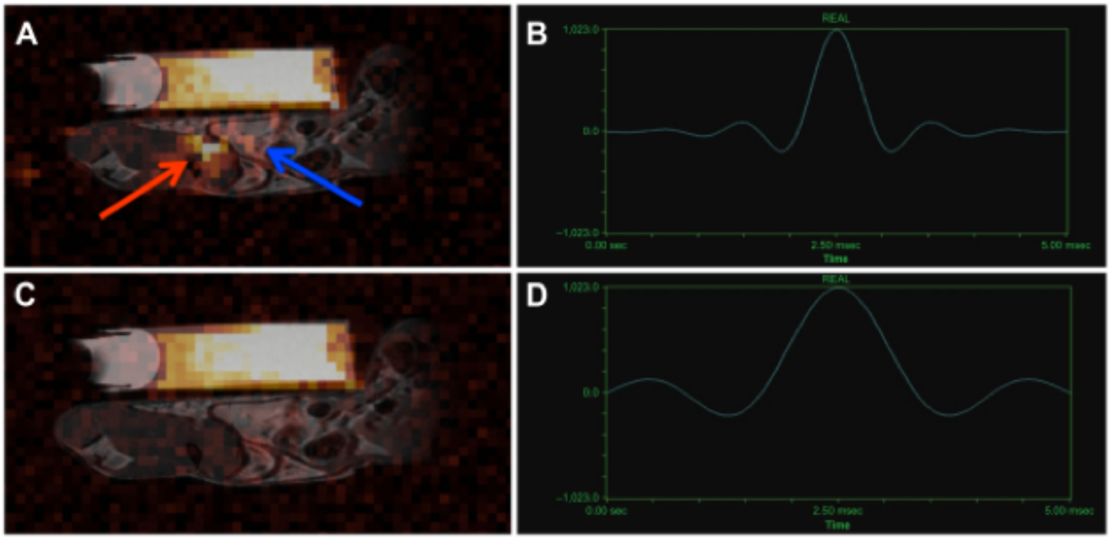

Figure 9: (A) **Isoflurane signal (red arrow) is visible within the body of the mouse. This signal is spatially offset from its true location in the fat pad (blue arrow) due to the center frequency being locked on Cell Sense. (B) The default truncated sinc pulse is narrower in temporal space then the sinc pulse (D). After fourier transform the wider sinc pulse produces a narrower rectangular shape in frequency space, preventing the excitation of isoflurane (C).**

2.6 Two-colour ^{19}F-MRI

Building on the same principle as avoiding isoflurane excitation, distinct ^{19}F peaks can be selectively excited in sequential acquisitions to provide two-colour ^{19}F-MRI. First shown in 2007 by Partlow et al., stem cells were labeled with either a PFOB or PFCE based nanoparticle.[2] This method allows for distinct cell populations to be identified and has applications in tracking multiple systems simultaneously. In Figure 10, data from a pilot experiment shows the i.v. distribution of Cell Sense (red) mapped alongside the isoflurane distribution (green). It was particularly interesting to note that this data shows that both Cell Sense and isoflurane are present in the liver. Although two-colour MRI was not utilized in this thesis, the technique has strong potential for application in the future directions of this work.

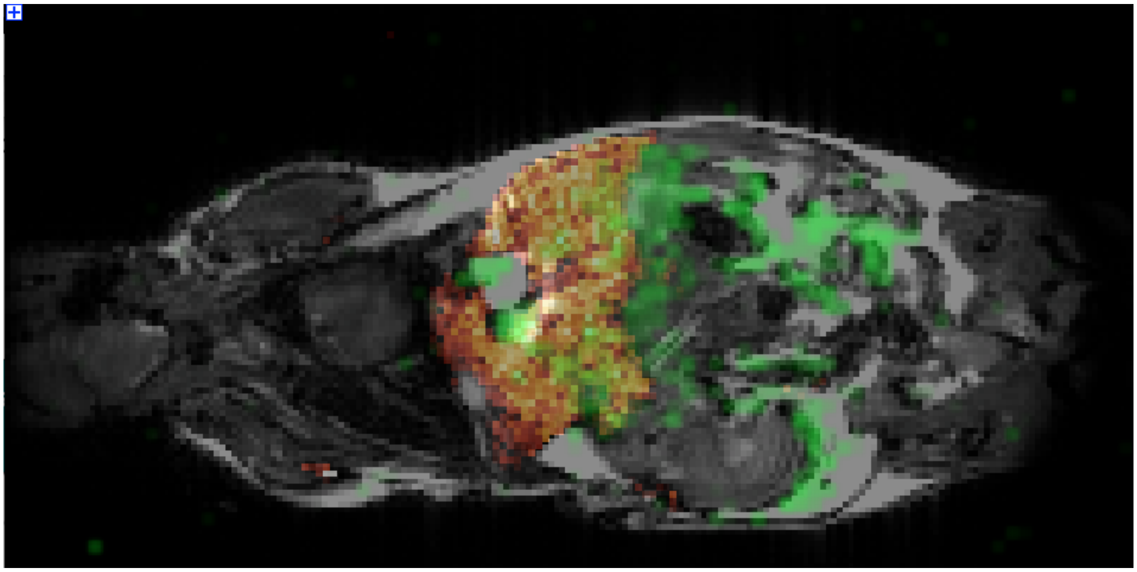

Figure 10: By employing the narrow peak selective pulses, the distribution of i.v. Cell Sense (red) can be imaged separately from isoflurane (green). The two ^{19}F images were then combined with an anatomical image.

2.7 Common Artifacts

The most common artifact observed in ^{19}F-MRI cell tracking is the point spread function (PSF) resulting from under sampled imaging. The artifact is especially prominent in ^{19}F-cell tracking due to the strong signal produced by a point source of cells, and the lack of background. PSF results in characteristic linear lines of noise in all three dimensions centered on the point source, as shown in Figure 11.

This artifact can be reduced by increasing acquisition matrix size. However, due to the relatively low number of ^{19}F atoms located within each voxel, as well as the importance of detecting all of these atoms for accurate quantification, lower resolution is preferable for ^{19}F imaging (on the order of mm^3 for pre-clinical systems). In order to keep voxel size large enough for detection, the field of view can be increased to extend beyond the animal. Unfortunately, this results in an increase of “dead-space” imaging, where no animal is present, along with the increase in imaging time associated with a larger acquisition matrix. The work presented in this thesis has attempted to balance acceptable PSF image artifact with reasonable scan time.

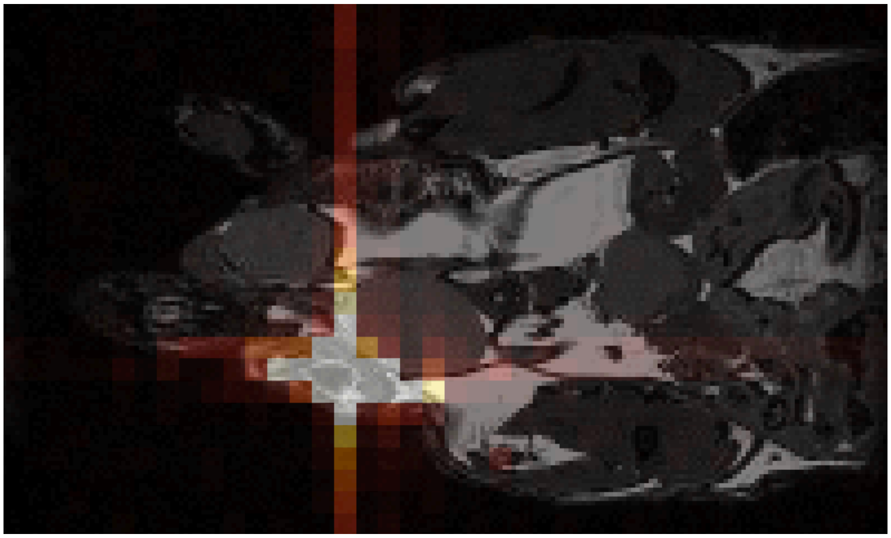

Figure 11: Point spread function artifact produced by a region of high intensity signal. The artifact complicates image analysis, particularly when comparing signal between structures in the opposite side of the animal.

Chemical shift artifacts are the second most commonly observed in images. This artifact appears as a 1-2 voxel shift in spatial location between matched proton and fluorine images. These occur when the ^{19}F imaging frequency is offset from the Cell Sense peak frequency, as shown with the isoflurane signal in Figure 8. Luckily, post-processing correction of the artifact is simple by aligning the reference tubes in the ^{19}F and ^{1}H images.

2.8 References

1. Fox MS, Gaudet JM, Foster PJ. Fluorine-19 MRI Contrast Agents for Cell Tracking and Lung Imaging. 2015;8:1–15.

2. Partlow KC, Chen J, Brant J a, Neubauer AM, Meyerrose TE, Creer MH, Nolta J a, Caruthers SD, Lanza GM, Wickline S a. 19F magnetic resonance imaging for stem/progenitor cell tracking with multiple unique perfluorocarbon nanobeacons. FASEB journal : official publication of the Federation of American Societies for Experimental Biology. 2007;21(8):1647–54.

3. Ribot EJ, Gaudet JM, Chen Y, Gilbert KM, Foster PJ. In vivo MR detection of fluorine-labeled human MSC using the bSSFP sequence. International journal of nanomedicine. 2014;9:1731–9.

4. Bouchlaka MN, Ludwig KD, Gordon JW, Kutz MP, Bednarz BP, Fain SB, Capitini CM. ^{19} F-MRI for monitoring human NK cells in vivo. OncoImmunology. 2016;(March):00–00.

5. Rose L, Kadayakkara DKK, Wang G, Bar-Shir A, Helfer BM, O'Hanlon CF, Kraitchman DL, Rodriguez RL, Bulte JWM. Fluorine-19 Labeling of Stromal Vascular Fraction Cells for Clinical Imaging Applications. Stem Cells translational medicine. 2015:1–8.

6. Goette MJ, Keupp J, Rahmer J, Lanza GM, Wickline S a, Caruthers SD. Balanced UTE-SSFP for (19) F MR imaging of complex spectra. Magnetic resonance in medicine : official journal of the Society of Magnetic Resonance in Medicine / Society of Magnetic Resonance in Medicine. 2014;0:1–7.

7. Speck O, Scheffler K, Hennig J. Fast 31P chemical shift imaging using SSFP methods. Magnetic resonance in medicine : official journal of the Society of Magnetic Resonance in Medicine / Society of Magnetic Resonance in Medicine. 2002;48(4):633–9.

8. Colotti R, Bastiaansen JAM, Wilson A, Flögel U, Gonzales C, Schwitter J, Stuber M, van Heeswijk RB. Characterization of perfluorocarbon relaxation times and their influence on the optimization of fluorine-19 MRI at 3 tesla. Magnetic Resonance in Medicine. 2016;0.

9. Nateras O. SNR using balanced steady-state free precession (b-SSFP). ric.uthscsa.edu. 2010;0(RADI 6016):0–7.

10. Scheffler K, Lehnhardt S. Principles and applications of balanced SSFP techniques. European radiology. 2003;13(11):2409–18.

11. Ribot EJ, Martinez-Santiesteban FM, Simedrea C, Steeg PS, Chambers AF, Rutt BK,

Foster PJ. In vivo single scan detection of both iron-labeled cells and breast cancer metastases in the mouse brain using balanced steady-state free precession imaging at 1.5 T. Journal of magnetic resonance imaging : JMRI. 2011;34(1):231–8.

12. Heyn C, Ronald J a, Ramadan SS, Snir J, Barry AM, MacKenzie LT, Mikulis DJ, Palmieri D, Bronder JL, Steeg PS, et al. In vivo MRI of cancer cell fate at the single-cell level in a mouse model of breast cancer metastasis to the brain. Magnetic resonance in medicine : official journal of the Society of Magnetic Resonance in Medicine / Society of Magnetic Resonance in Medicine. 2006;56(5):1001–10.

13. Heyn C, Bowen C V, Rutt BK, Foster PJ. Detection threshold of single SPIO-labeled cells with FIESTA. Magnetic resonance in medicine : official journal of the Society of Magnetic Resonance in Medicine / Society of Magnetic Resonance in Medicine. 2005;53(2):312–20.

14. Ribot EJ, Foster PJ. In vivo MRI discrimination between live and lysed iron-labelled cells using balanced steady state free precession. European radiology. 2012;22(9):2027–34.

15. Economopoulos V, Noad JC, Krishnamoorthy S, Rutt BK, Foster PJ. Comparing the MRI appearance of the lymph nodes and spleen in wild-type and immuno-deficient mouse strains. PloS one. 2011;6(11):e27508.

16. Srinivas M, Heerschap A, Ahrens ET, Figdor CG, de Vries IJM. (19)F MRI for quantitative in vivo cell tracking. Trends in biotechnology. 2010;28(7):363–70.

17. Helfer BBM, Balducci A, Nelson AD, Janjic JM, Gil RR, Kalinski P, Vries IJMDE, Ahrens ET, Mailliard RB, de Vries IJM. Functional assessment of human dendritic cells labeled for in vivo (19)F magnetic resonance imaging cell tracking. Cytotherapy. 2010;12(2):238–50.

18. Goette MJ, Lanza GM, Caruthers SD, Wickline S a. Improved quantitative (19) F MR

molecular imaging with flip angle calibration and B1 -mapping compensation. Journal of magnetic resonance imaging : JMRI. 2014 Nov 25:1–7.

19. Meissner M, Reisert M, Hugger T, Hennig J, von Elverfeldt D, Leupold J. Revealing signal from noisy (19) F MR images by chemical shift artifact correction. Magnetic resonance in medicine : official journal of the Society of Magnetic Resonance in Medicine / Society of Magnetic Resonance in Medicine. 2014;0:1–9.

20. Zhong J, Mills PH, Hitchens TK, Ahrens ET. Accelerated fluorine-19 MRI cell tracking using compressed sensing. Magnetic resonance in medicine : official journal of the Society of Magnetic Resonance in Medicine / Society of Magnetic Resonance in Medicine. 2012;0:1–8.

21. Srinivas M, Morel PA, Ernst L a, Laidlaw DH, Ahrens ET. Fluorine-19 MRI for visualization and quantification of cell migration in a diabetes model. Magnetic resonance in medicine : official journal of the Society of Magnetic Resonance in Medicine / Society of Magnetic Resonance in Medicine. 2007;58(4):725–34.

22. Basse-Lusebrink TC, Weise G, Stoll G. Imaging of inflammation in the peripheral nervous system by 19 F MRI. 2011;19:3710.

23. Zhong J, Sakaki M, Okada H, Ahrens ET. In Vivo Intracellular Oxygen Dynamics in Murine Brain Glioma and Immunotherapeutic Response of Cytotoxic T Cells Observed by Fluorine-19 Magnetic Resonance Imaging Mosley RL, editor. PLoS ONE. 2013;8(5):e59479.

24. Kampf T, Fischer a, Basse-Lüsebrink TC, Ladewig G, Breuer F, Stoll G, Jakob PM, Bauer WR. Application of compressed sensing to in vivo 3D ^{19}F CSI. Journal of magnetic resonance (San Diego, Calif. : 1997). 2010;207(2):262–73.

25. Hertlein T, Sturm V, Jakob P, Ohlsen K. 19F magnetic resonance imaging of perfluorocarbons for the evaluation of response to antibiotic therapy in a Staphylococcus aureus infection model. PloS one. 2013;8(5):e64440.

26. Hertlein T, Sturm V, Kircher S, Basse-Lüsebrink T, Haddad D, Ohlsen K, Jakob P, Basse-luesebrink T. Visualization of Abscess Formation in a Murine Thigh Infection Model of Staphylococcus aureus by 19 F- Magnetic Resonance Imaging (MRI). PloS one. 2011;6(3):e18246.

27. Weise G, Basse-Luesebrink TC, Wessig C, Jakob PM, Stoll G. In vivo imaging of inflammation in the peripheral nervous system by (19)F MRI. Experimental neurology. 2011;229(2):494–501.

28. Van Heeswijk RB, De Blois J, Kania G, Gonzales C, Blyszczuk P, Stuber M, Eriksson U, Schwitter J. Selective in vivo visualization of immune-cell infiltration in a mouse model of autoimmune myocarditis by fluorine-19 cardiac magnetic resonance. Circulation: Cardiovascular Imaging. 2013;6(2):277–284.

29. Morgan GE. Clinical Anesthesiology (5th ed.). 2013. 156 p.

Chapter 3

3 Tracking the Fate of Stem cell Implants with Fluorine-19 MRI[†]

3.1 Introduction

Stem cell therapy has the potential to play an important role in regenerative medicine. Mesenchymal stromal/stem cells (MSCs) have been extensively investigated for clinical application over the past decade.[1,2] MSCs are capable of differentiating into a variety of important tissues, such as: bone, cartilage and adipose.[3] They also display immunomodulatory properties.[4–6] Their presence in adult tissue, and ease of expansion *in vitro* has made MSCs good candidate cells for clinical translation.[7,8]

To advance stem cell therapy, there is a desire to develop tools to monitor the survival of implanted stem cells non-invasively after administration to the patient. Magnetic resonance imaging (MRI) cell tracking is an effective method to visualize and monitor cells non-invasively after implantation due to the high spatial resolution and lack of ionizing radiation.

The majority of MRI cell tracking studies have used iron oxide nanoparticles to label the cells of interest.[9–15] When imaged with MRI, the iron nanoparticles produce a dark signal void in T_2 and T_2* weighted proton images. This technique is highly sensitive, permitting the imaging of single cells.[16,17] Limitations with tracking iron-labeled cells arise from low specificity, due to other regions in the image with low signal, and from complicated *in vivo* quantification of the signal loss. Our group and others have shown that the degree of signal loss produced by iron labeled cells is only linear at low iron concentrations.[16,18] Furthermore the high sensitivity to iron can produce ambiguity due to the strong false-positive signal produced when even a small number of bystander cells become labeled inadvertantly.[19,20]

[†] This chapter was previously published and is included here with permission and minor revisions: Gaudet JM, Ribot EJ, Chen Y, Gilbert KM, and PJ Foster (2015) "Mesenchymal stem cell transplant rejection monitored with ^{19}F-MRI," *PLoS ONE* 10(3): e0118544.

As an alternative to iron-oxide cell tracking, fluorine-19 (^{19}F) MRI with perfluorocarbon (PFC) nanoemulsions has been used for cell tracking.[21] ^{19}F MRI is able to image implanted cells with high specificity due to the lack of detectable fluorine in biological tissue.[22,23] Quantification of implanted cells is possible since the ^{19}F MRI signal intensity is linearly related to the number of ^{19}F-labeled cells. Unlike PET/SPECT probes, ^{19}F does not undergo radioactive decay allowing for longitudinal studies without radiation-induced toxicity to the implanted cells or surrounding tissue. Furthermore, the first clinical application of ^{19}F-MRI cell tracking for DC immunotherapy was recently reported, showing the technique is both feasible and safe for human application.[24]

In this paper, we investigated the feasibility of quantifying MSC fate in two different immune environments. This was performed by comparing the change in ^{19}F-MRI signal strength over time using two popular transplantation models. A syngeneic transplant model, with mouse MSCs (mMSC) implanted in an immune-competent mouse host, was compared to a xenograft model produced from human MSCs (hMSC) implanted in an immune-compromised mouse. Our goals were: i) to quantify the apparent cell number non-invasively for 2.5 weeks and ii) to validate *in vivo* ^{19}F-MRI quantification results with fluorescence microscopy and immunohistochemistry.

3.2 Methods

3.2.1 MSC Culture and Labeling

hMSC came from bone marrow donated by healthy young adult volunteers after written informed consent according to a protocol approved by University Health Network Research Ethics Board (Toronto, Canada)[25]. hMSC were cultured as described by Ribot et al.[19] Briefly, hMSC were grown in low glucose Dulbecco's Modified Eagle's Medium until passage 4. mMSC initially derived from the bone marrow of C57Bl/6 mice and expressing green fluorescence protein (GFP+) were purchased from Cyagen Bioscience Inc. (Catalog # MUBMX-01101). The cells were cultured in OriCell™ Mouse MSC

Growth Medium until 90% confluent. The mMSC were passaged once before labeling and implantation.

MSC were labeled with the red fluorescent perfluoropolyether agent, Cell Sense (CS-ATM-DM Red; CelSense Inc. Pittsburg, USA)[26]. Labeling took place over 24 hours at a concentration of 2.5mg/mL. After incubation, the cells were washed 3 times with Hank's balanced salt solution (HBSS), harvested with Trypsin, spun down and counted. At this stage the cells were tested for viability using trypan blue exclusion. Intracellular ^{19}F content of cells was determined using NMR spectroscopy, as we have described previously.[19]

3.2.2 MSC Implantation

1.5×10^6 Cell Sense-labeled hMSC in 100μL of HBSS were implanted intramuscularly into the right hindlimb muscle of immune-compromised, nude mice (nu/nu, Charles River Canada) to produce a xenograft model (n=7). In a similar manner, 2.0×10^6 labeled mMSC in 100μL of HBSS were implanted into immune competent, C57Bl/6 mice (Jackson Laboratories) producing a syngeneic model (n=8). In both cases, the injections were performed under 2% isoflurane anesthesia. All experiments involving human and mouse stem cells, as well as animal use, were approved by the Western University Animal Use Committee (AUP 2009-042).

3.2.3 MRI

All images were collected using a 9.4T Varian small-animal MRI scanner. A 3D balanced steady state free precession (bSSFP) sequence was used for both proton and fluorine imaging. Cell pellets containing 2×10^5, 4×10^5, 6×10^5, 8×10^5, 1×10^6 and 2×10^6 ^{19}F-labeled MSC were imaged alongside a CS-1000 reference tube of known fluorine concentration (7.3×10^{16} ^{19}F/μL). MRI was performed using a dual-tuned birdcage volume coil (diameter 2.2cm, length 5.1cm), tuned to 400.2 MHz and 376.8 MHz for proton and fluorine imaging respectively. For proton imaging of cell pellets the scan parameters were: repetition time (TR)=3.8ms, echo time (TE)=1.9ms, receiver bandwidth (rBW)=125kHz, flip angle (FA)=30°, averages=2, resolution=$200\times200\times200\mu m^3$. For fluorine imaging the parameters were: TR=3.5ms, TE=1.8ms, rBW=25kHz, FA=70°, averages=250, resolution=1x1x2mm^3. Total protocol time for both proton and fluorine imaging was under 90 minutes. The pellets were imaged on three separate occasions to test quantification variability.

Mice containing ^{19}F-labeled MSC implantations were imaged at four time points, starting on day 0, after implantation. The scan parameters were the same for the *in vivo* mouse MRI as described above. During scanning the mice were anesthetized with 2% isoflurane, with breathing rate and temperature monitored. Due to the high sensitivity of bSSFP to off-resonance frequencies[27], a narrow 1.5kHz sinc pulse was used to excite only the ^{19}F agent.

3.2.4 Image Analysis and Quantification

Prior to image analysis, a signal correction was applied to the ^{19}F datasets by subtracting a constant value (x) from all voxels within the dataset using the image program, ImageJ.[28,29] The value of x was equal to the signal of the single voxel containing the lowest signal throughout the entire dataset. This linear translation acted to left-shift the data distribution to begin at zero. Quantification was performed using Voxel Tracker^{TM} software, as described by Srinivas et al.[30] Briefly, in the ^{19}F MR images, the signal contained within a hand drawn ROI is summed and compared to the average signal produced by the reference tube of known concentration (2.6x10^{16} ^{19}F spins/μL). This value (X) provides the total number of ^{19}F spins located at the ROI. NMR spectroscopy was then performed using a known number of the same transplanted cells, along with a second ^{19}F source containing a known number of ^{19}F spins. By comparing the relative NMR signals, the number of ^{19}F spins per cell (Y) is obtained. Division of X by Y yields the number of cells located at the ROI. Significance between time-points was assessed using a repeated measures, one-way ANOVA.

3.2.5 MSC Immunohistochemistry

Mice were sacrificed and perfused with 4% paraformaldehyde following the final imaging timepoint. In addition, one mouse from each model was sacrificed and perfused on Day 0 for comparison. The hindlimb muscle was extracted and cryoprotected with increasing concentrations of sucrose (10%, 20%, 30%) before freezing in OCT medium. Tissue was sectioned with a cryostat. Fluorescence microscopy was performed to image the red fluorescent ^{19}F-label as well as the GFP+ mMSC with a Zeiss AXIO Imager microscope (Carl Zeiss Canada Ltd). Immunohistochemistry staining was then performed on these sections. Macrophage presence was assessed using Biotin anti-mouse macrophage (F4/80) monoclonal antibody (Cedarlane Laboratories Ltd) with 3,3'-Diaminobenzidine (DAB) counterstain.

3.3 Results

In vivo results

Figure 12A shows that labeling with the ^{19}F agent did not negatively affect the mMSC cellular viability. The viability of the hMSC was slightly decreased following labeling. Previous work by our group demonstrated that the perfluorocarbon, Cell Sense, does not negatively impact differentiation of labeled hMSC into osteogenic or adipogenic lineages.[19] NMR revealed the mean cellular loading of ^{19}F varied between experiments and cell types within the range of 8.2×10^{10} to 2.4×10^{11} atoms.

Quantification of ^{19}F in cell samples

Quantification of the ^{19}F signal was tested in vitro using Cell Sense labeled mMSC pellets. Imaging was performed at 9.4T on six cell pellets ranging from 200k to 2 million cells. Figure 13 represents the average quantification and standard deviation from imaging the cell pellets on three different occasions. We observed a strong linear relationship between the MR quantification and the real cell number, with an $R^2=0.98$.

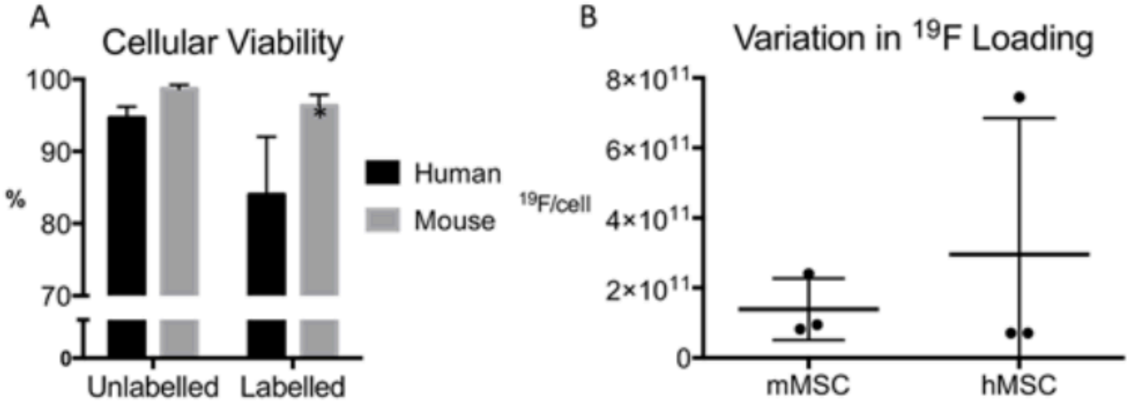

Figure 12: (A) Cellular viability was investigated before and after labeling with the ^{19}F-agent, Cell Sense. Although a statistically significant difference was observed in hMSC after labeling, the viability remained high (>80%) in all experiments. There was no significant difference in mMSC viability. (B) Mean cellular loading was determined by performing NMR spectroscopy on a known number of cells alongside a reference peak with a known number of ^{19}F atoms. We observed variation in cellular loading of both hMSC and mMSC between experimental batches. However, this variation does not affect in vivo ^{19}F quantification since each transplant was only compared to its specific cellular loading.

In vivo detection of ^{19}F MRI signal

^{19}F-MRI signal was initially detectable in all mice following intramuscular injection of 2.0×10^6 mMSC or 1.5×10^6 hMSC. On day 0 quantification of the *in vivo* signal agreed very well with the number of implanted cells (Fig. 14). Over time the signal decreased in both models. In the immune competent model (Fig. 14A), a significant difference was observed in the ^{19}F MRI signal over time [F(1.703,6.812)=39.85, $p<0.001$]. Post hoc Tukey tests showed there was a significant difference in ^{19}F signal between day 3 and day 9 ($p<0.01$), and day 9 and 16 ($p<0.05$). At 16 days post implantation only two mice had any detectable signal remaining. Signal in the immune-compromised mice (Fig. 14B) decreased more slowly [F(1.378,5.511)=30.97, $p<0.01$], with significance from day 0

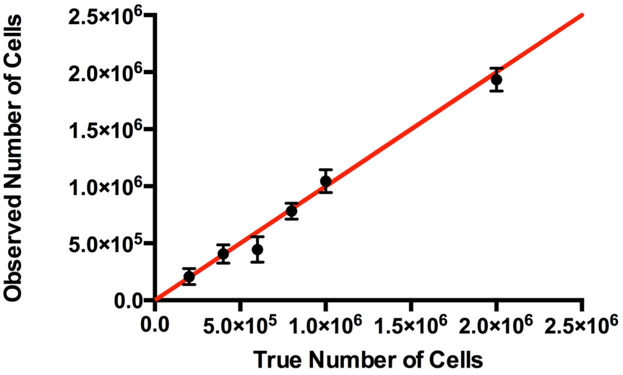

Figure 13: *in vitro* validation of ^{19}F-MRI quantification accuracy. Quantification was validated in a phantom study using cell pellets ranging from 2x10^{5} to 2x10^{6} MSC. Pellets were imaged three times, with the error bars representing the standard deviation between scans. The ^{19}F-MRI quantification is in very strong agreement with the true number of cells, and has a Pearson correlation coefficient of 0.99. The red line represents the ideal result of a 1:1 correlation.

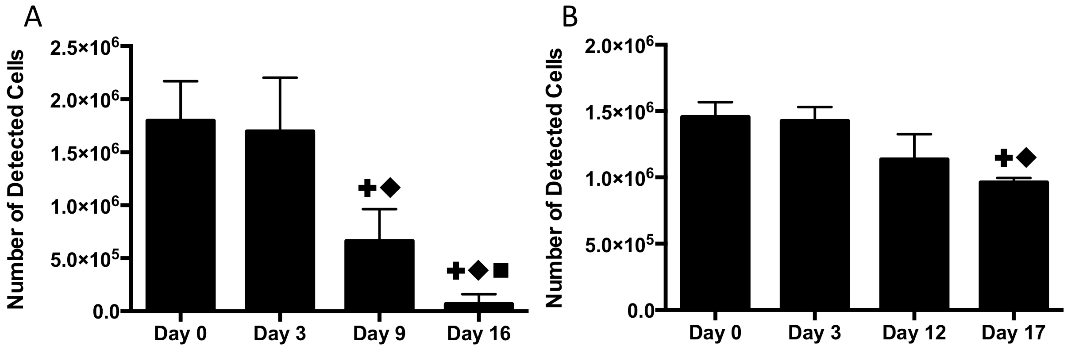

Figure 14: Comparison of ^{19}F-labeled cell detection in two transplantation models over time (A) Following implantation of 2x10^{6} mMSC, ^{19}F-MRI was used to quantify the number of cells remaining over 16 days. By day 16, only 2/7 mice had any detectable signal remaining. A significant difference from day 0 is denoted by ✚, from day 3 by ◆, and from day 9 by ■. (B) The number of detectable cells over a similar time period following a transplant of 1.5x10^{6} hMSC. ^{19}F signal was found to decrease at a slower rate, with observable signal in all mice at the endpoint. Statistical significance is denoted in the same way as A.

only detectable on day 17 ($p<0.01$). Furthermore, at this endpoint all immune-compromised mice still had detectable signal.

Representative MR image data, fluorescence microscopy, and H&E obtained on day 0 is shown in Figure 15. Overlays of the ^{19}F MRI onto the proton image at day 0 are shown in 15A and E for the immune competent and immune compromised mice, respectively. Figures 15B and F show that the red fluorescence signal from the ^{19}F labeling agent can be detected on day 0 in both models. The green fluorescence associated with the GFP+ mMSC was also visible at the site of their implantation on day 0 (Fig. 15C). Overlaying the two fluorescent images revealed co-localization, with a Pearson's correlation coefficient of 0.80, between the red fluorescent ^{19}F agent and the GFP+ mMSC in Figure 15D. The corresponding H&E stained tissue sections agree with the location of the implant within the muscle (Fig. 15G,H).

Figure 16 shows representative MR image data, H&E, F4/80 immunohistochemistry and fluorescence microscopy obtained at the experimental endpoint. By day 16 post implantation no ^{19}F-MRI signal from the mMSC was detectable in 5/7 of the immune competent mice. One of these mice is shown in Figure 16A where the only ^{19}F signal comes from the reference tube. In contrast, ^{19}F signal was still detectable in all of the immune compromised mice at day 17, with an example shown in Figure 16E. Fluorescence microscopy revealed only a small area of red fluorescence from the ^{19}F agent in the immune competent model (Fig. 16B) compared to the immune compromised (Fig. 16F). In addition, no GFP+ mMSC were detectable in *ex vivo* samples at endpoint. H&E staining of the same tissue sections showed cells at the site of the implant, which corresponded with the ^{19}F agent's red fluorescence (Fig. 16C,G). Neighboring tissue sections corresponding to high red fluorescence were stained for the presence of macrophages using F4/80. Figure 16D suggests that relatively few macrophages were detected in the immune competent model at endpoint. In contrast, the F4/80 stain revealed macrophages (Fig. 16H) in the same region as the red fluorescence from the

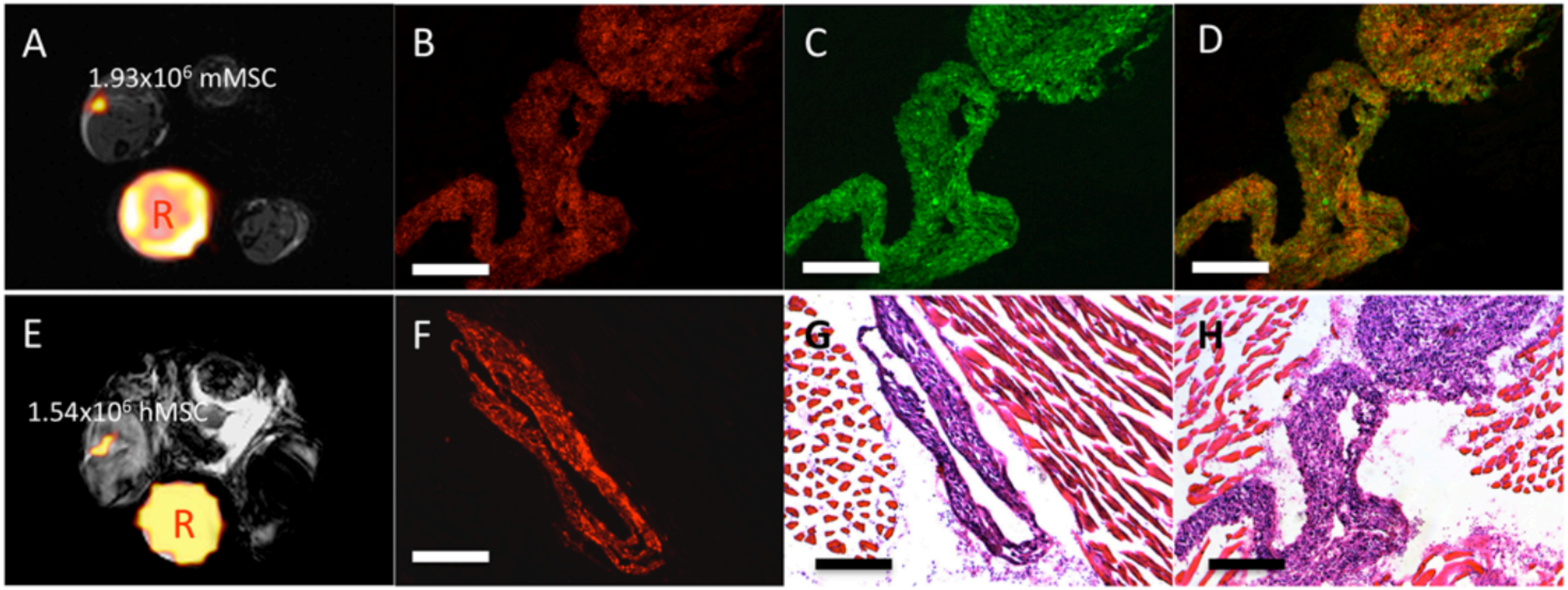

Figure 15: (A, E) Representative MRI from mice receiving either 2x10^6 mMSC or 1.5x10^6 hMSC respectively. The day 0 *in vivo* ^{19}F-MRI quantification correlates very well with the number of implanted cells. The reference tube is marked by "R". (B) The red fluorescent fluorine agent is clearly visible in the tissue of the immune competent model, (F) as well as in the immune-compromised model. (C) Furthermore, the GFP+ mMSC are observable within the tissue section. (D) Overlaying the two fluorescent images, reveals the ^{19}F agent colocalized with the GFP+ mMSC, as expected. (G, H) H&E stained tissue sections corresponding to the fluorescence microscopy clearly show the implant site of the mMSC and hMSC respectively. Scale bars in all images represent 250µm

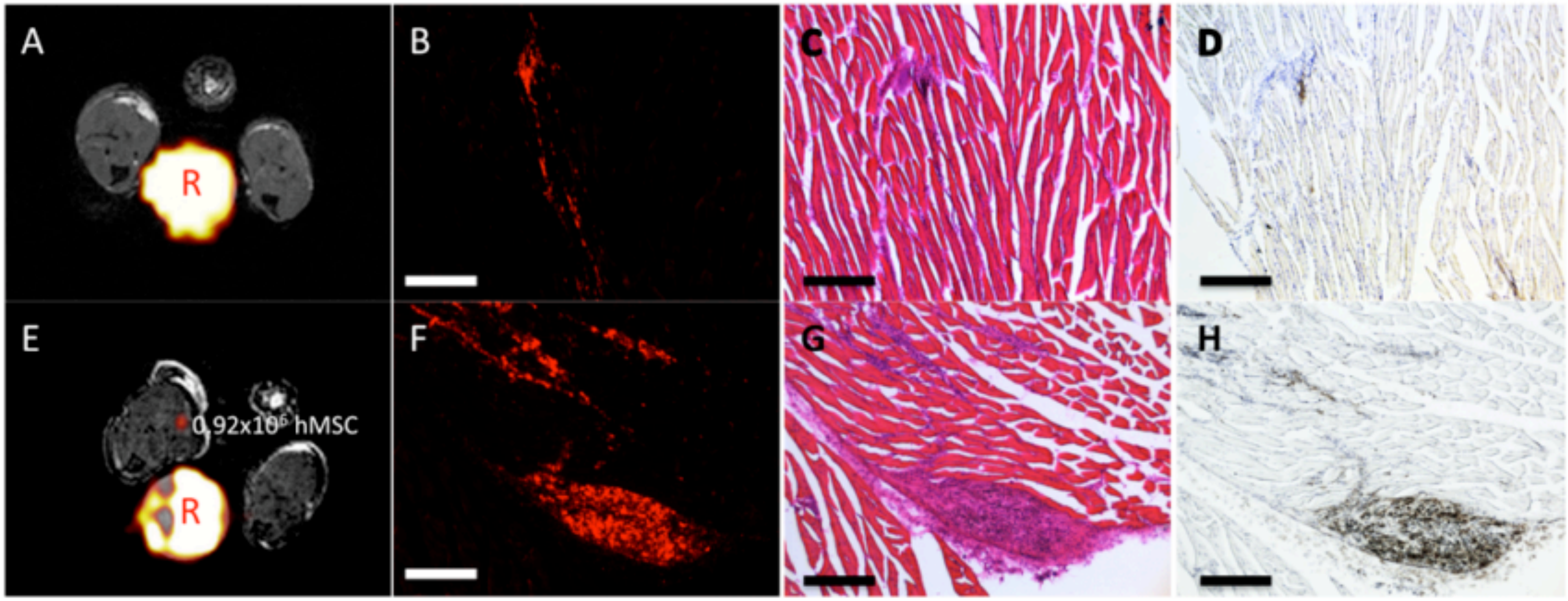

Figure 16: By day 16, 5/7 immune competent mice had no ^{19}F-MRI signal remaining (A). The reference tube is marked by "R". (B) Fluorescence microscopy of the muscle agreed with little red fluorescence. No GFP+ mMSC were detectable by fluorescence microscopy, suggesting the original mMSC are no longer present. (C) H&E staining reveals cells at the implant site which correlates with the remaining ^{19}F red fluorescence. (D) Immunohistochemistry staining of adjacent tissue sections with the anti-F4/80 antibody reveals a few macrophages at this location in the immune competent model. (E) At endpoint, all immune compromised mice had detectable ^{19}F-MRI signal remaining. (F) More red fluorescence is visible, and (G)H&E staining again correlates well with the regions of red fluorescence. (H) Macrophage staining reveals many more F4/80 positive cells at the site of implantation corresponding to the regions of red fluorescence. Scale bars represent 250µm.

^{19}F agent in the immune compromised model. The number of macrophages visually corresponded with the amount of remaining red fluorescence in both cases.

3.4 Discussion

In vivo quantification of MSC

This study demonstrates the ability to use ^{19}F-MRI cell tracking to detect and, most importantly, to measure the signal from transplanted stem cells in vivo. It is difficult to quantify cell number using other MRI cell tracking techniques. Numerous studies have previously reported on the challenges associated with quantification of signal loss due to iron-labeled cells.[19,20,31] This has, so far, narrowed the implementation of cell tracking for monitoring the fate of transplanted cells. In this study, we show excellent correlation between the number of labeled cells implanted and the number of cells counted on day 0 by ^{19}F-MRI. This capability will pave the way for MRI to be used in confirming the delivery of therapeutic cell transplants.

The importance of accurate delivery of cells to a target tissue cannot be overstated. In preclinical investigations often stem cells will be transplanted then a set time allowed to lapse before the transplanted tissue is removed and processed for microscopy, to determine whether stem cells remain in the tissue. In many cases, only a very small sample of the transplanted tissue is evaluated. In a previous study we used MRI to track iron-labeled MSC in a mouse model of spinal cord injury[32]. Our *in vivo* imaging revealed that the challenging intrathecal injections of MSC were imprecise approximately 25% of the time; injected cells were often being deposited in tissue above the cord or leaking out of the cord. The histological assessment in this study involved the analysis of 1cm of cord tissue on either side of the transplant site, six weeks after transplantation. Without MRI, a negative observation of MSC by microscopy would have been taken as failure to engraft rather than due to a missed injection. Injection confirmation with ^{19}F MRI would have the additional advantage of determining how many cells were properly injected and remain at the site.

In a first-in-man study, MRI and scintigraphy were used to assess the success of intranodal injections consisting of a 1:1 mixture of iron- or indium-labeled dendritic cell (DC) for cancer therapy in melanoma patients.[33] Despite these cell injections being performed under ultrasound guidance the MRI of iron-labeled DC revealed that in 3/8 cases DC were injected near, but not in, the target lymph nodes.[33] These findings make it clear that the outcome of this cell therapy on these patients would not be properly evaluated without knowledge of proper delivery of DC to the nodes. For DC therapy knowledge of the number of cells delivered to a lymph node is especially critical since DC migration to nodes correlates with effective stimulation of T cells. ^{19}F-MRI therefore presents a promising solution to the clinical problem of verifying both the location and number of cells within the region of interest immediately following administration of treatment.

In these experiments the hMSC and the mMSC were both capable of taking up sufficient ^{19}F label for in vivo detection, without decreasing viability below 80%. We observed some variation in the number of ^{19}F atoms loaded per cell between experiments, although the average loading was not significantly different for mouse versus human MSC. The cell size is one of the more important factors influencing the labeling with Cell Sense and mouse and human MSC are approximately 30 microns in diameter. The fact that it is possible to obtain robust measurements of the number of cells detected by MRI, despite inter-experiment variation in the number of ^{19}F atoms per cell, is another positive feature of this type of cell tracking. The variation in ^{19}F/cell between batches is not a confounding factor in the ^{19}F-MRI quantification since the mean cellular loading is determined for each transplantation. This is particularly important when considering clinical translation, since ^{19}F uptake is expected to vary between cell donors.

Monitoring the fate of MSC over time

This study also revealed some interesting information about tracking cell fate over time with ^{19}F MRI. We studied the fate of MSC in two different models: mMSC implanted into healthy wild type C57Bl/6 mice (immune competent model) and hMSC implanted into healthy nude mice (immune compromised model). We believe the MSC and ^{19}F-label, underwent clearance from the sites of implantation in muscle at different rates, which is not unexpected since the two different mouse strains have very different immune systems.

In the immune competent model, 5/7 mice had no MRI detectable ^{19}F signal remaining at the site of injection by the endpoint. The other 2 mice had just 4% and 10% of the original signal remaining. There were no GFP+ cells detected by fluorescence microscopy but there was some red fluorescence, indicating that some of the ^{19}F label persisted at the site but that it was not within GFP+ mMSC. The small amount of residual red fluorescent signal corresponded with F4/80 staining suggesting that some transfer of ^{19}F label from mMSC to macrophages has occurred. The decline in the signal is likely the result of several different things happening at the transplant site. First, many MSC will die early after their direct transplantation into a tissue. Second, the label may be diluted by MSC proliferation, or degradation of the label within MSC. Third, MSC may have migrated away from the implant site; although we did not detect ^{19}F signal in other nearby locations.

The fact that for 5/7 mice no endpoint MRI signal was detected, even though red fluorescence was still observed in the tissues (as for the example shown in Fig 16A-D) is most likely because the number of cells containing the red fluorescent ^{19}F label is very small. This small amount of ^{19}F signal is below the *in vivo* detection limits of the MRI protocols used in this study.

In the immune compromised model the ^{19}F signal persisted in all mice until the experimental endpoint. Much more red fluorescence was observed in these tissues at the implant site and this corresponded well with F4/80 staining, again suggesting that the persistent ^{19}F signal was related to transfer of label from hMSC to macrophages. A limitation of this study was that our hMSC were not also GFP+. This would have allowed us to say with more confidence that the ^{19}F label was associated with macrophages and not the implanted hMSC. Clearance of label and macrophages may have been slower in these mice because of the inhibited immune system and lack of rejection response.

Our observation of bystander cell uptake of ^{19}F cell label is supported by a study by Boehm-Sturm et al.[34] In their study in vivo imaging of the location, density, and survival of neural stem cells implanted in the brain in a stroke model was performed using ^{19}F MRI in combination with bioluminescence imaging. The signal from ^{19}F labeled stem cells persisted for more than 4 weeks after implantation while, over the same time period, the bioluminescence declined, indicating stem cell death. Immunohistochemistry staining also revealed the presence of microglia/macrophages at the site of implantation.

Terrovitis et al. looked at the retention of iron labeled stem cells implanted into immune competent rats.[20] Either rat or human cardiac-derived stem cells were injected intramyocardially. In both cases MRI signal loss due to iron was detected for 3 weeks post cell injection and correlated with the presence of iron containing macrophages in histology. Although the area of signal void decreased over time, substantial signal void persisted at the injection site in all mice. Since proton MRI is sensitive to even small numbers of iron-labeled cells this form of cell tracking is most susceptible to the misinterpretation of cell fate. Previous studies performed in our lab using iron labeled syngeneic MSC also revealed the persistence of an iron signal void past 21 days in immune competent mice.[14]

3.5 Conclusions

In summary, ^{19}F MRI can be used to provide immediate assessment of implanted cells with excellent correlation between implanted cell number and *in vivo* quantification. Over time, as the cells are cleared from the transplantation site, transfer of the ^{19}F label to bystander cells may confuse interpretation of the change in ^{19}F signal. With the first-in-man studies of ^{19}F MRI recently completed, this result will be particularly relevant when translating this technique into the clinic.[24]

3.6 References

1. Chagastelles PC, Nardi NB, Camassola M. Biology and applications of mesenchymal stem cells. Science progress. 2010;93(2):113–127.

2. Meirelles L da S, Nardi NB. Methodology, biology and clinical applications of mesenchymal stem cells. Frontiers in Bioscience. 2009;14(6):4281–4298.

3. Pittenger MF. Multilineage Potential of Adult Human Mesenchymal Stem Cells. Science. 1999;284(5411):143–147.

4. Keating A. Mesenchymal stromal cells: new directions. Cell Stem Cell. 2012;10(6):709–16.

5. Nauta AJ, Westerhuis G, Kruisselbrink AB, Lurvink EG a, Willemze R, Fibbe WE. Donor-derived mesenchymal stem cells are immunogenic in an allogeneic host and stimulate donor graft rejection in a nonmyeloablative setting. Blood. 2006;108(6):2114–20.

6. Le Blanc K, Ringdén O. Immunomodulation by mesenchymal stem cells and clinical experience. Journal of internal medicine. 2007;262(5):509–25.

7. Caplan AI. Mesenchymal stem cells. Journal of Orthopaedic Research. 1991;9(5):641–50.

8. Psaltis P, Zannettino A. Concise review: mesenchymal stromal cells: potential for cardiovascular repair. Stem Cells. 2008:2201–2210.

9. Addicott B, Willman M, Rodriguez J, Padgett K, Han D, Berman D, Hare JM, Kenyon NS. Mesenchymal stem cell labeling and in vitro MR characterization at 1.5 T of new SPIO contrast agent: Molday ION Rhodamine-B^{TM}. Contrast media & molecular imaging. 2010;6(1):7–18.

10. Hill JM, Dick AJ, Raman VK, Richard B, Yu Z, Hinds KA, Pessanha BSS, Mcveigh ER, Lederman RJ. Serial cardiac magnetic resonance imaging of injected mesenchymal stem cells. 2006;108(8):1009–1014.

11. Xu C, Miranda-Nieves D, Ankrum J a, Matthiesen ME, Phillips J a, Roes I, Wojtkiewicz GR, Juneja V, Kultima JR, Zhao W, et al. Tracking mesenchymal stem cells with iron oxide nanoparticle loaded poly(lactide-co-glycolide)

microparticles. Nano letters. 2012;12(8):4131–9.

12. Reddy AM, Kwak BK, Shim HJ, Ahn C, Lee HS, Suh YJ, Park ES. In vivo tracking of mesenchymal stem cells labeled with a novel chitosan-coated superparamagnetic iron oxide nanoparticles using 3.0T MRI. Journal of Korean medical science. 2010;25(2):211–9.

13. Li X-X, Li K-A, Qin J-B, Ye K-C, Yang X-R, Li W-M, Xie Q-S, Jiang M-E, Zhang G-X, Lu X-W. In vivo MRI tracking of iron oxide nanoparticle-labeled human mesenchymal stem cells in limb ischemia. International journal of nanomedicine. 2013;8:1063–73.

14. Noad J, Gonzalez-Lara LE, Broughton HC, McFadden C, Chen Y, Hess D a, Foster PJ. MRI tracking of transplanted iron-labeled mesenchymal stromal cells in an immune-compromised mouse model of critical limb ischemia. NMR in Biomedicine. 2013;26(4):458–67.

15. Mathiasen AB, Hansen L, Friis T, Thomsen C, Bhakoo K, Kastrup J. Optimal Labeling Dose , Labeling Time, and Magnetic Resonance Imaging Detection Limits of Ultrasmall Superparamagnetic Iron-Oxide Nanoparticle Labeled Mesenchymal Stromal Cells. Stem cells international. 2013;2013.

16. Heyn C, Bowen C V, Rutt BK, Foster PJ. Detection threshold of single SPIO-labeled cells with FIESTA. Magnetic Resonance in Medicine. 2005;53(2):312–20.

17. Shapiro EM, Sharer K, Skrtic S, Koretsky AP. In vivo detection of single cells by MRI. Magnetic Resonance in Medicine. 2006;55(2):242–9.

18. Bonetto F, Srinivas M, Heerschap A, Mailliard R, Ahrens ET, Figdor CG, de Vries IJM, Vries IJM De. A novel (19)F agent for detection and quantification of human dendritic cells using magnetic resonance imaging. International journal of cancer. Journal international du cancer. 2011;129(2):365–73.

19. Ribot EJ, Gaudet JM, Chen Y, Gilbert KM, Foster PJ. In vivo MR detection of fluorine-labeled human MSC using the bSSFP sequence. International Journal of

Nanomedicine. 2014;9:1731–9.

20. Terrovitis J, Stuber M, Youssef A, Preece S, Leppo M, Kizana E, Schär M, Gerstenblith G, Weiss RG, Marbán E, et al. Magnetic resonance imaging overestimates ferumoxide-labeled stem cell survival after transplantation in the heart. Circulation. 2008;117(12):1555–62.

21. Ahrens ET, Flores R, Xu H, Morel PA. In vivo imaging platform for tracking immunotherapeutic cells. Nature biotechnology. 2005;23(8):983–7.

22. Morawski AM, Winter PM, Yu X, Fuhrhop RW, Scott MJ, Hockett F, Robertson JD, Gaffney PJ, Lanza GM, Wickline S a. Quantitative "magnetic resonance immunohistochemistry" with ligand-targeted (19)F nanoparticles. Magnetic resonance in medicine : official journal of the Society of Magnetic Resonance in Medicine / Society of Magnetic Resonance in Medicine. 2004;52(6):1255–62.

23. Ruiz-Cabello J, Walczak P, Kedziorek D a, Chacko VP, Schmieder AH, Wickline S a, Lanza GM, Bulte JWM. In vivo "hot spot" MR imaging of neural stem cells using fluorinated nanoparticles. Magnetic Resonance in Medicine. 2008;60(6):1506–11.

24. Ahrens ET, Helfer BM, O'Hanlon CF, Schirda C. Clinical cell therapy imaging using a perfluorocarbon tracer and fluorine-19 MRI. Magnetic Resonance in Medicine. 2014;72:1696–1701.

25. Dayan V, Yannarelli G, Billia F, Filomeno P, Wang X-H, Davies JE, Keating A. Mesenchymal stromal cells mediate a switch to alternatively activated monocytes/macrophages after acute myocardial infarction. Basic research in cardiology. 2011;106(6):1299–310.

26. Helfer BBM, Balducci A, Nelson AD, Janjic JM, Gil RR, Kalinski P, Vries IJMDE, Ahrens ET, Mailliard RB, de Vries IJM. Functional assessment of human dendritic cells labeled for in vivo (19)F magnetic resonance imaging cell tracking. Cytotherapy. 2010;12(2):238–50.

27. Scheffler K, Lehnhardt S. Principles and applications of balanced SSFP techniques. European Radiology. 2003;13(11):2409–18.

28. Abràmoff MD, Magalhães PJ, Ram SJ. Image processing with imageJ. Biophotonics International. 2004;11(7):36–41.

29. Schneider C a, Rasband WS, Eliceiri KW. NIH Image to ImageJ: 25 years of image analysis. Nature Methods. 2012;9(7):671–675.

30. Srinivas M, Morel PA, Ernst L a, Laidlaw DH, Ahrens ET. Fluorine-19 MRI for visualization and quantification of cell migration in a diabetes model. Magnetic Resonance in Medicine. 2007;58(4):725–34.

31. Frangioni J V, Hajjar RJ. In vivo tracking of stem cells for clinical trials in cardiovascular disease. Circulation. 2004;110(21):3378–83.

32. Gonzalez-Lara LE, Xu X, Hofstetrova K, Pniak A, Chen Y, McFadden CD, Martinez-Santiesteban FM, Rutt BK, Brown A, Foster PJ. The use of cellular magnetic resonance imaging to track the fate of iron-labeled multipotent stromal cells after direct transplantation in a mouse model of spinal cord injury. Molecular Imaging and Biology. 2011;13(4):702–11.

33. de Vries IJM, Lesterhuis WJ, Barentsz JO, Verdijk P, van Krieken JH, Boerman OC, Oyen WJG, Bonenkamp JJ, Boezeman JB, Adema GJ, et al. Magnetic resonance tracking of dendritic cells in melanoma patients for monitoring of cellular therapy. Nature Biotechnology. 2005;23(11):1407–13.

34. Boehm-Sturm P, Aswendt M, Minassian A, Michalk S, Mengler L, Adamczak J, Mezzanotte L, Löwik C, Hoehn M. A multi-modality platform to image stem cell graft survival in the naïve and stroke-damaged mouse brain. Biomaterials. 2014;35(7):2218–26.

Chapter 4

4 Application of Dual ^{19}F- and Iron-Cellular MRI Agents to Track the Infiltration of Immune Cells to the Site of a Rejected Stem Cell Transplant[‡]

4.1 Introduction

Cellular magnetic resonance imaging (MRI) has proven to be an effective technique for non-invasive tracking of cellular therapeutics. The absence of signal attenuation with tissue depth and the lack of ionizing radiation allows for long-term monitoring without risk to the patient or therapeutic cells. MRI cell tracking relies on pre-labeling cells with a non-invasive imaging agent to render them MRI detectable. To date, most cellular MRI has been performed with one of two labeling agents. The first, and most common, is superparamagnetic iron oxide (SPIO) nanoparticles. Iron-labeled cells are indirectly detected as a region of signal void. When subjected to an external magnetic field, SPIOs change the net local magnetization. This acts to increase the R2* relaxation rates of the surrounding nuclear spins. In the MR image, this results in signal loss or regions of hypointensity. Iron-based cell tracking has the advantage of being highly sensitive, due to the large magnetic field inhomogeneity effect produced by SPIO which is indirectly detected through the abundant water proton signal; a so-called blooming artifact. Single cell imaging has previously been demonstrated with iron agents[1,2]. The technique is limited by the challenges associated with quantifying signal loss, due to the non-linear relationship with iron concentration[3]. This makes it difficult to quantify cell number and track changes in cell number over time.

[‡] This chapter was previously published and is included here with permission: Gaudet JM, Hamilton AM, Chen Y, Fox MS, and PJ Foster (2016) “Application of dual ^{19}F and iron cellular MRI agents to track the infiltration of immune cells to a site of a rejected stem cell transplant” *Journal of Magnetic Resonance in Medicine.* Early view online

Over the past decade, fluorine-19 (^{19}F) based cell tracking techniques have become of increased interest[4]. Utilizing the MRI sensitive ^{19}F nuclei, this method involves the direct measurement of signal from ^{19}F spins and has no effect on proton contrast. Since biological tissue has negligible levels of ^{19}F, no background signal is present and the ^{19}F signal is inherently quantitative. However, the relative insensitivity of the nuclear magnetic resonance signal means that thousands of cells per voxel are required for detection. The minimum number of cells required for detection varies between cell types depending on intracellular ^{19}F uptake; which ranges between $10^{10\text{-}13}$ ^{19}F/cell.

A major focus of MRI cell tracking has been on understanding the *in vivo* behaviour of transplanted stem cells[5,6]. Prior to implantation, stem cells are labeled with an MR imaging agent in culture. Iron and ^{19}F-based agents have both been utilized to investigate the location, migration and survival of stem cells [7–10]. With applications in neural, bone, cardiac, and cartilage reconstruction, stem cells have a high potential for therapeutic application. In addition to cell restoration, recent studies have highlighted the important role stem cells play in promoting growth within the local microenvironment through the secretion of trophic factors[11–13]. Unfortunately, this therapeutic potential is often limited due to stem cell death. In the days following administration, many stem cells undergo apoptosis due to the stresses of administration and inadequate access to nutrients[12,14–17]. Cytokines released by the apoptotic stem cells attract macrophages to the implant site, triggering an immune response by the host[18–20]. The immune cell infiltration occurs rapidly, often within the first week after transplant[21].

A number of studies have now demonstrated that tracking iron-labeled stem cells with MRI cannot be used to reveal graft rejection *in vivo*[8,22–28]. This is because it is not possible to reliably distinguish between live and dead iron-labeled cells in MRI. Bernau et al. shows that the death of iron-labeled human neural progenitor cells transplanted into the rat brain could be identified *in vivo* by bioluminescence imaging (BLI) but not by MRI; the BLI signal decreased below a detectable level with cell death while the MRI signal remained the same due to transfer of the iron label to bystander macrophages[26].

Another cellular MRI strategy for detecting rejection has been to image the immune cells that infiltrate a failed graft. Here, iron particles are administered i.v. and engulfed by cells of the reticuloendothelial system. MRI is typically performed one day later to visualize the accumulation of iron-labeled cells, mainly macrophages and monocytes, at the site of the transplantation. A significant decrease in the MR signal intensity indicates rejection has occurred. This approach was first used to detect acute rejection in a model of rat renal transplantation in 2000[29]. Since then, numerous studies have investigated the application of i.v. iron for detecting organ and stem cell rejection[29–32]. The potential for clinical translation of this technique has been recently demonstrated with the clinical i.v. administration of an ultra-small SPIO (USPIO), ferumoxytol[33,34]. ^{19}F agents have been used in a similar manner within pre-clinical models for imaging inflammation[35–38].

The purpose of this study was to investigate the use of ^{19}F- and iron-based cellular MRI techniques in concert to simultaneously monitor transplanted stem cells and infiltrating macrophages. Human mesenchymal stem cells (hMSC) were labeled with a ^{19}F agent prior to intramuscular implantation into the mouse hind-limb and macrophage infiltration resulting from rejection of the transplant was visualized by *in situ* labeling with i.v. administered USPIO nanoparticles.

4.2 Methods

4.2.1 hMSC Culture and Labeling

hMSC were collected from the bone marrow of healthy, young adult volunteers donated with written informed consent according to a protocol approved by University Health Network Research Ethics Board (Toronto, Canada)[39]. The cells were cultured in low-glucose DMEM with 10% (Thermo Fisher Scientific Corp, Waltham, MA, USA) until 90% confluent.

hMSC were labeled with the red fluorescent perfluoropolyether agent, Cell Sense (CS-1000-ATM:DM Red, CelSense Inc., Pittsburgh, USA)[40]. Labeling took place over 24 hours at a concentration of 2.5mg/mL. After incubation, the cells were repeatedly washed with Hank's balanced salt solution (HBSS) before and after TrypLE™ dissociation. The viability of the isolated cells was tested by trypan blue exclusion. Intracellular ^{19}F content of cells (F_c) was determined using NMR spectroscopy, as we have described previously[28].

4.2.2 hMSC Implantation

$1x10^6$ Cell Sense labeled hMSC in 50µL of HBSS were implanted intramuscularly into the right hindlimb muscle of 14 immune competent, C57Bl/6 mice (Jackson Laboratories, USA), as shown in figure 17. This model was utilized to promote a strong immune response against the human cells by the host. The injections were performed under 2% isoflurane in 100% oxygen anesthesia. 24 hours after hMSC implantation, the mice were randomly assigned to one of two groups. Group A (n=7) received no further treatment. Group B (n=7) received 0.5mmol/kg of the ferumoxytol Feraheme (AMAG Pharmaceuticals, Waltham, USA) i.v. via tail vein 24 hours after the hMSC implantation. Two additional groups of 3 mice were used for controls. Group C (n=3), received 50µL HBSS on Day 0 instead of hMSC, followed by 0.5mmol/kg of Feraheme i.v. 24 hours later. Group D (n=3) received $1x10^6$ unlabeled hMSC, followed 24 hours later by 200uL of i.v. ^{19}F agent (VS-1000, CelSense Inc., Pittsburgh, USA). All experiments involving human stem cells, as well as animal use, were approved by the Western University Animal Use Committee.

4.2.3 MRI

All images were collected using a 9.4T Varian small-animal MRI scanner. A 3D-balanced steady state free precession (bSSFP) sequence was used for both ^1H and ^{19}F imaging. Animals were imaged alongside an agarose diluted Cell Sense reference tube of known ^{19}F concentration ($3.33x10^{16}$ $^{19}F/\mu L$). MRI was performed using a dual-tuned birdcage volume coil (diameter 2.2cm, length 5.1cm), tuned to 400.2 MHz and 376.8 MHz for ^1H and ^{19}F imaging, respectively. For ^1H imaging the scan parameters

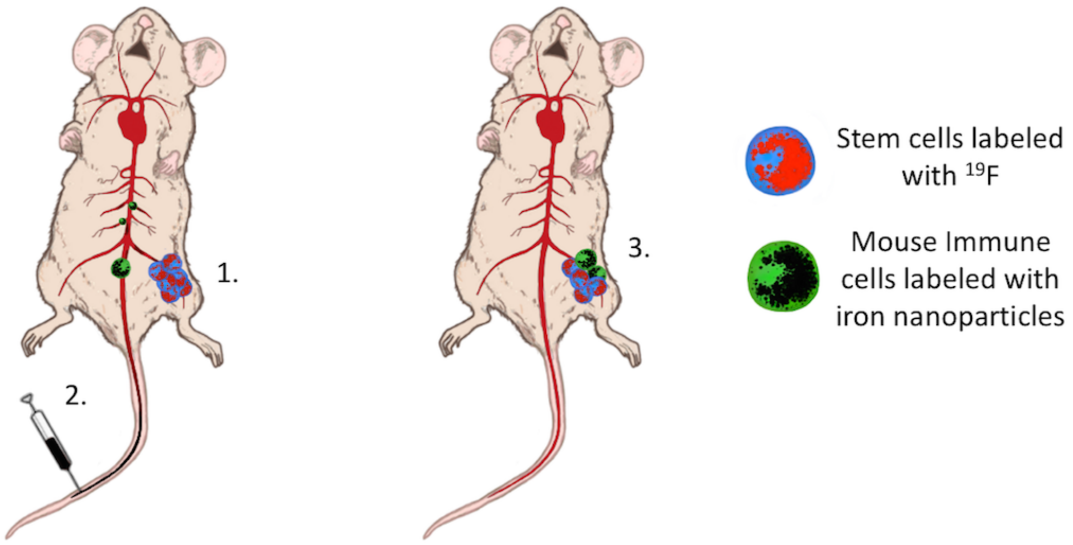
1.
2.
3.
Stem cells labeled with ^{19}F
Mouse Immune cells labeled with iron nanoparticles

Figure 17: Human MSC were labeled with a ^{19}F agent prior to being implanted into the mouse hindlimb muscle. Quantification of the ^{19}F signal performed at this timepoint shows a strong correspondence with the expected number of cells. 2) One day after implantation, iron nanoparticles were administered i.v. These nanoparticles are scavenged from the bloodstream by macrophages and monocytes, rendering them MRI detectable. 3) Two days after implantation, iron labeled macrophages have migrated to the site of implant. The labeled macrophages are visible in MR images as signal voids at the site. ^{19}F-MRI signal is also significantly decreased as the iron quenches the signal.

were: repetition time (TR)=5.0ms, echo time (TE)=2.5ms, receiver bandwidth (rBW)=78kHz, flip angle (FA)=30°, phase cycles (PC)=4, averages=3, resolution=200x200x200µm^3. For ^{19}F imaging the parameters were: TR=5.5ms, TE=2.8ms, rBW=25kHz, FA=70°, PC=4 averages=30, resolution=0.5x0.5x1mm^3. Imaging parameters were chosen based upon optimization work performed in previous studies[27,28]. Total protocol time for both ^{1}H and ^{19}F imaging was under 60 minutes.

Mice were imaged immediately following hMSC implantation (day 0) and on days 2, 6, 10, and 14. During scanning the mice were anesthetized with 2% isoflurane in 100% oxygen, with breathing rate and temperature monitored. A 1ms Gaussian shaped excitation pulse was used to prevent detection of ^{19}F signal from the isoflurane anesthetic, as described in more detail previously[27].

4.2.4 Image Analysis and Quantification

Prior to image analysis a signal correction was applied to the ^{19}F datasets by subtracting the value of the voxel containing the lowest signal in the dataset using ImageJ software[41,42]. ^{19}F signal quantification was performed using Voxel Tracker^{TM} software. The total signal contained within a hand drawn ROI produced by the ^{19}F labeled cells was compared to the average signal produced by the reference tube of known concentration (3.33×10^{16} ^{19}F spins/μL). This information was used alongside F_c measured with NMR, to quantify the apparent number of cells located at the ROI, as described by Srinivas et al[43]. Significance between time-points was assessed using a repeated measures, one-way ANOVA using GraphPad Prism 6 software (GraphPad, San Diego, CA, USA).

4.2.5 Immunohistochemistry

Mice were sacrificed and perfusion fixed with 4% paraformaldehyde (PFA) following the final imaging timepoint on day 14. In addition, two mice from group A and B were sacrificed and perfused; 24 hours following i.v. iron injection (day 2) for comparison. Tissue was cryoprotected with increasing concentrations of sucrose (10%, 20%, 30%) before freezing in OCT medium, and sectioned at 12μm thickness. A DAB-enhanced Prussian Blue stain was used to detect iron. Prussian Blue staining was performed with the slides were placed in 4% potassium ferrocyanide (Fisher Scientific, Waltham, MA) and 4% hydrochloric acid. After washing, DAB- intensification was performed 3,3'-diaminobenzidine tetrahydrochloride (DAB; Sigma Aldrich, St Louis, MO) staining. Lectin immunofluorescence was then performed on the iron-stained sections to identify macrophages. First, sections were incubated with biotinylated isolectin B4 (Sigma Aldrich) and Triton X-100 overnight. Sections were then incubated in the dark with streptavidin conjugated with fluor 488 (1:500; ThermoFisher Scientific). Finally, tissue was counterstained with Hoechst stain for detection of cell nuclei. Fluorescence microscopy was performed to image the red fluorescent ^{19}F-label as well as the green fluorescent lectin label with a Zeiss AXIO Imager microscope (Carl Zeiss Canada Ltd). Slides were assessed through visual inspection.

4.3 Results

hMSC labeling with ^{19}F

NMR revealed the cellular loading, F_c, varied between study replications within the range of 8.2×10^{10} to 2.4×10^{11} ^{19}F atoms/cell. This large variability in labeling efficiency between replications has been previously observed in numerous studies with human cells[28,44]. Previous work by our group demonstrated that labeling hMSC with Cell Sense, does not negatively impact viability or differentiation into osteogenic or adipogenic lineages[27,28].

In vivo detection of ^{19}F-labeled hMSC

On the day of implantation (day 0) the ^{19}F-labeled hMSC were visible in all mice in Groups A and B (Figure 18). In Group A, the mice that received only ^{19}F labeled hMSC, the ^{19}F signal gradually decreased between days 0 and 14 post implantation (Figure 18A-E). This result is expected as the implanted hMSC die, and the ^{19}F label is dispersed. At the endpoint, the average ^{19}F signal was 22±11% of the initial value. One mouse within this group had no detectable signal in the final imaging session.

In Group B, the mice that received i.v. Feraheme 24 hours after the hMSC implantation, a large region of signal void was visible at the implant site in day 2 proton images (Figure 18G, day 2). Coincident with this was a significant decrease in the detected ^{19}F signal compared to the day 0 signal from the same group. This is due to quenching of the ^{19}F signal by the spin dephasing produced by nearby iron nanoparticles. Between days 2 and 14 the ^{19}F signal remained lower in Group B for each time point compared to Group A and the region of signal void persisted in the proton images. Signal loss was also observed in the lymph nodes, spleen and liver following i.v. Feraheme administration, resulting from the uptake of iron nanoparticles by macrophages of the reticuloendothelial system.

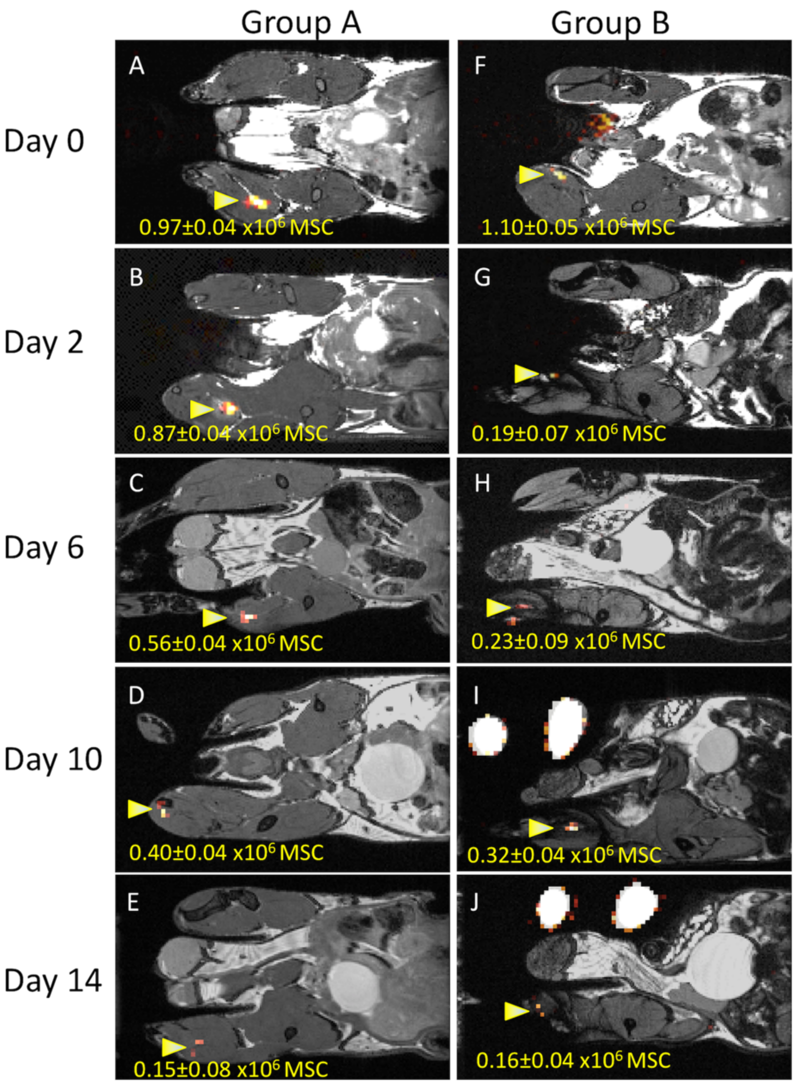
Group A
Group B
Day 0
Day 2
Day 6
Day 10
Day 14
A
$0.97\pm0.04 \times 10^6$ MSC
F
$1.10\pm0.05 \times 10^6$ MSC
B
$0.87\pm0.04 \times 10^6$ MSC
G
$0.19\pm0.07 \times 10^6$ MSC
C
$0.56\pm0.04 \times 10^6$ MSC
H
$0.23\pm0.09 \times 10^6$ MSC
D
$0.40\pm0.04 \times 10^6$ MSC
I
$0.32\pm0.04 \times 10^6$ MSC
E
$0.15\pm0.08 \times 10^6$ MSC
J
$0.16\pm0.04 \times 10^6$ MSC

Figure 18: Representative images at each time point from Group A and B. Images were produced by overlaying ^{19}F signal onto proton images for anatomical context. Mice were imaged over 14 days following intramuscular injection of ^{19}F agent labeled hMSC on Day 0 (A,F). Detected ^{19}F signal from the hMSC implant is denoted by a yellow arrow in each image. Quantification of the apparent number of hMSC from ^{19}F signal was calculated using reference tubes of known ^{19}F concentration. The reference tube is visible in panels I & J, and partially visible in panel F. Mice in group A (A-E), received no further treatment besides imaging. Group B mice (F-J) received i.v. iron on Day 1 following fluorine-labelled stem cell transplant. The i.v. iron is taken up by macrophages and monocytes in the bloodstream. On Day 2 (G), a large region of signal void is visible at the implant site. The presence of signal void indicates iron labeled immune cells have migrated to the implant site. This signal void region persists at each time point until endpoint on day 14 (G-J). No signal loss was observed in the muscle of the untreated leg. In addition to the implant site; voids were also visible in the lymph nodes, lymphatics, liver, and spleen.

Quantification of the ^{19}F signal for Groups A and B is shown in Figure 19. For both Groups A and B we present the apparent number of hMSC, determined as described in the methodology. On day 0 the mean values for cell number were 0.99±0.08 x10^6 and 1.08±0.08 x10^6 for Groups A and B, which agree strongly with the number of cells implanted (i.e., 1x10^6 cells). In Group A, the apparent cell number decreased between days 0 and 14 post implantation. Significant differences in the mean apparent cell number were observed between days 0 and 6, days 2 and 10, and days 6 and 14. This quantification indicates that over time the ^{19}F labeled hMSC diminish in number, most likely due to cell death and clearance.

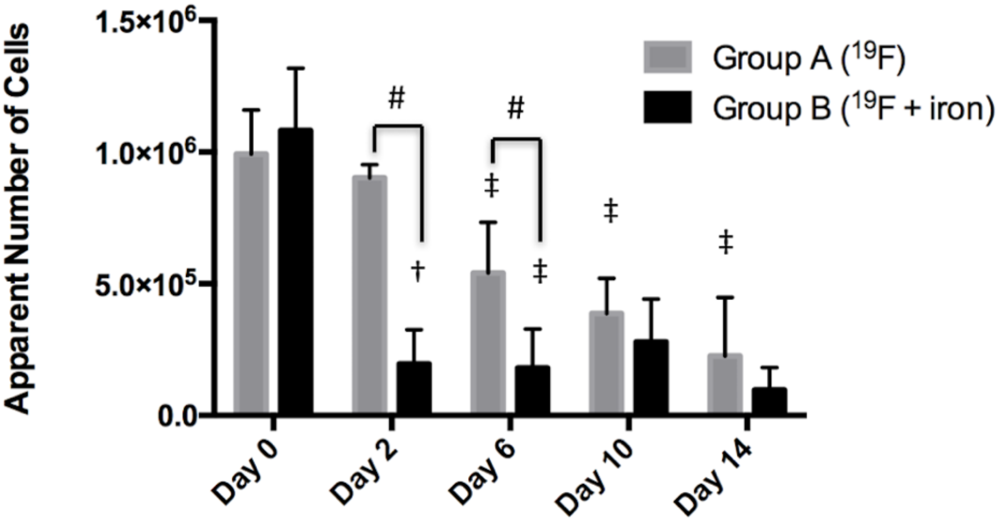

Figure 19: Quantification of ^{19}F signal at each time point. Significance between groups A&B at the same time point is donated with (#). Within the same group, over time is donated (†) between the previous time point and (‡) for between two time points. On day 0, both group A and B signal is in strong agreement with each other and with the expected number of implanted hMSC (1x10^6). Overtime, in group A ^{19}F signal decreased at each subsequent time point. This is likely due to cell death and ^{19}F agent clearance by the immune system. In group B, following i.v. iron administration there is a significant decrease in ^{19}F signal (day 2) compared to the previous time point and the Group A mice at the same time point. After this there is no significant change in ^{19}F signal in group B at any other time point.

For Group B, the mean apparent cell number sharply declined between days 0 and 2. This significant decrease reflects the presence of iron-positive macrophages, which has quenched the ^{19}F signal from the labeled hMSC[45]. Between days 2 and 14 there was no significant change in apparent cell number, suggesting that the iron-labeled macrophages persist at the implant site. When comparing between Groups A and B a significant signal difference was observed on days 2 and 6. Control mice, which received HBSS instead of hMSC, followed by i.v. Feraheme (Group C), did not have any signal voids within the muscle at any time point (Figure 20). For Group D mice, which received unlabeled hMSC on day 0 and i.v. ^{19}F agent on day 1, the ^{19}F signal was detected at the site of the cell implant in images acquired on day 2 and did not change significantly for the duration of the experiment (Figure 21).

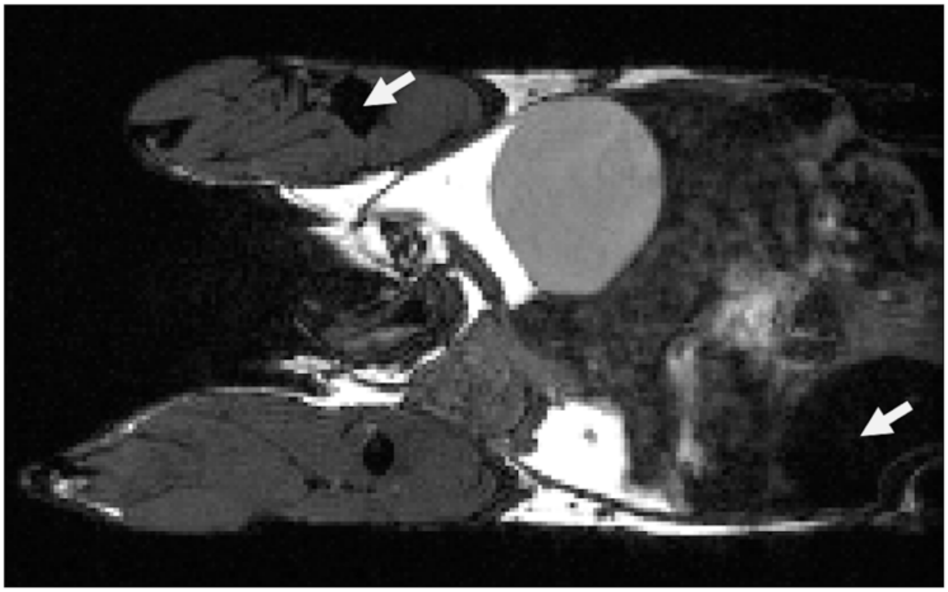

Figure 20: A sham model of Group B was produced by performing an intramuscular injection containing only saline on day 0, followed by intravenous iron on day 1. On day 2, no proton signal voids were detectable within the muscle. Signal voids were detectable within the bone marrow, lymph nodes, and liver, indicating the iron injection was successful. These regions are marked by white arrows.

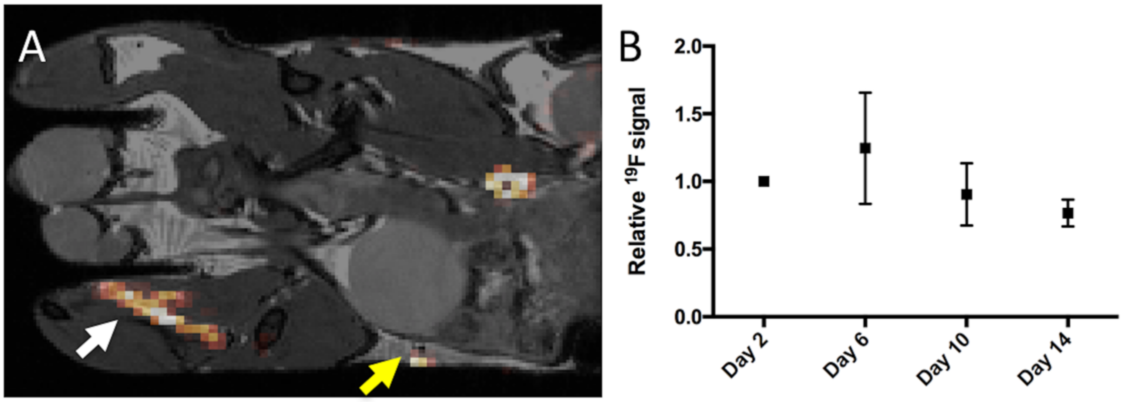

Figure 21: Inflammation was assessed by performing an intramuscular injection containing unlabeled hMSC on day 0, followed by i.v. ^{19}F agent on day 1 [Group D]. A representative ^{19}F/^{1}H overlaid image from day 2 shows a similar inflammation pattern within the muscle [white arrow] as observed with iron oxide (A). On day 2 a mean of $2.5\pm1.3\times10^{18}$ ^{19}F spins was detected at the transplant site. ^{19}F signal was also detected at the lymph node [yellow arrow]. Unlike Group B, the ^{19}F-labeled macrophages can be quantified over time (B). The relative signal normalized to day 2 within each mouse provides a measure of change in inflammation over time. No significant differences were observed at any time point.

Microscopy and Immunohistochemistry

Macrophages in the muscle tissue were identified through low magnification (10x) fluorescence microscopy of lectin immunohistochemistry-stained sections (Fig 22A&E). In mice euthanized on day 2, macrophages were localized within and surrounding the site of hMSC implantation, which was visible by the red fluorescence associated with the ^{19}F agent (Fig 22B). An overlay of the green, red, and blue (Hoescht) images revealed that there were macrophages within the hMSC tract that appear to be associated with the ^{19}F agent and other macrophages which were not. This is evident in the inset of Figure 22D where yellow suggests the co-localization of the fluorescence from the green macrophages and red ^{19}F agent. In mice euthanized on day 14, macrophages distribution appeared different compared to day 2 with green fluorescent signal predominately visible within the stem cell tract (Fig 22E). This was coincident with a visible decrease in the area of red fluorescence (Fig 22B), which agreed with the finding of decreased

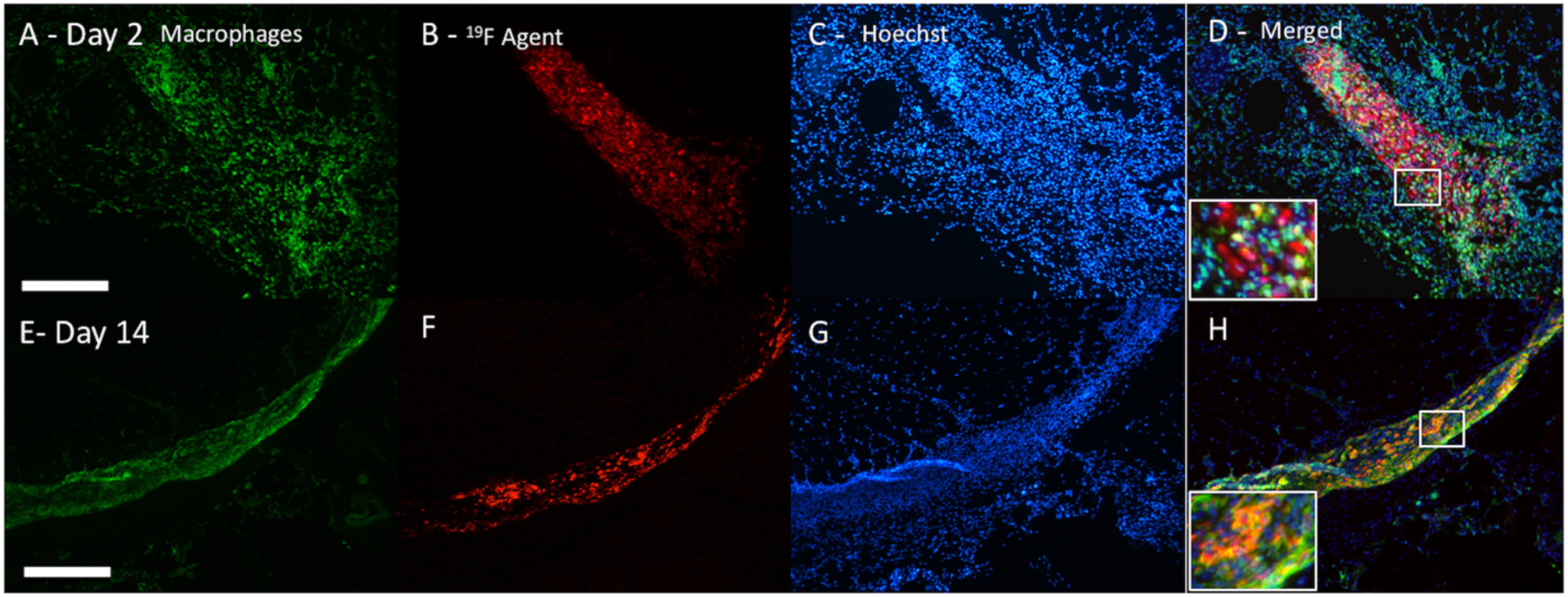

Figure 22: Fluorescence microscopy showing the intramuscular injection track on day 2 (A-D) and day 14 (E-H). Macrophages were stained with a green fluorescent lectin+ marker. At the early time point on day 2, macrophages are visible both within and surrounding the stem cell track (A). By endpoint on day 14, macrophages are only found within the transplant track (E). Scale bars denote 300 µm. The red fluorescent ^{19}F agent is visible within the stem cell track from the same tissue sections. More red fluorescence is visible on day 2 (B) then on day 14 (F), in agreement with MRI signal. Cell nuclei were detected with blue Hoeschst staining (C,G). Merged fluorescent images show some bystander labeling of macrophages, appearing as yellow. On day 2, there are few bystander labeled macrophages, as indicated by the separation between red and green fluorescent markers (H). However, by day 14 the majority of ^{19}F agent is contained within macrophages (H). This is highlighted within the magnified inset in the lower left corner (width 150µm).

^{19}F signal by MRI. The overlay (Fig 22H) suggests that 14 days after hMSC implantation the majority of the macrophages are restricted to the implant site, and are co-localized with the ^{19}F-labeled hMSC.

Tissue sections for mice in Group B are shown in Figure 23, alongside a representative proton image obtained on day 2. A large region of signal loss is visible in the muscle tissue (arrow). Iron stained cells appear dark brown within the muscle tissue sections on both day 2 (Fig 23B) and day 14 (Fig 23D). More iron-labeled cells were detected at day 14 compared to day 2. The corresponding red fluorescence images of these sections (Fig 23C&E) show the ^{19}F agent and the stem cell tract. The iron was often colocalized with the ^{19}F signal, especially at day 14, suggesting that macrophages have taken up dead ^{19}F labeled hMSC and have become co-labeled with iron and ^{19}F.

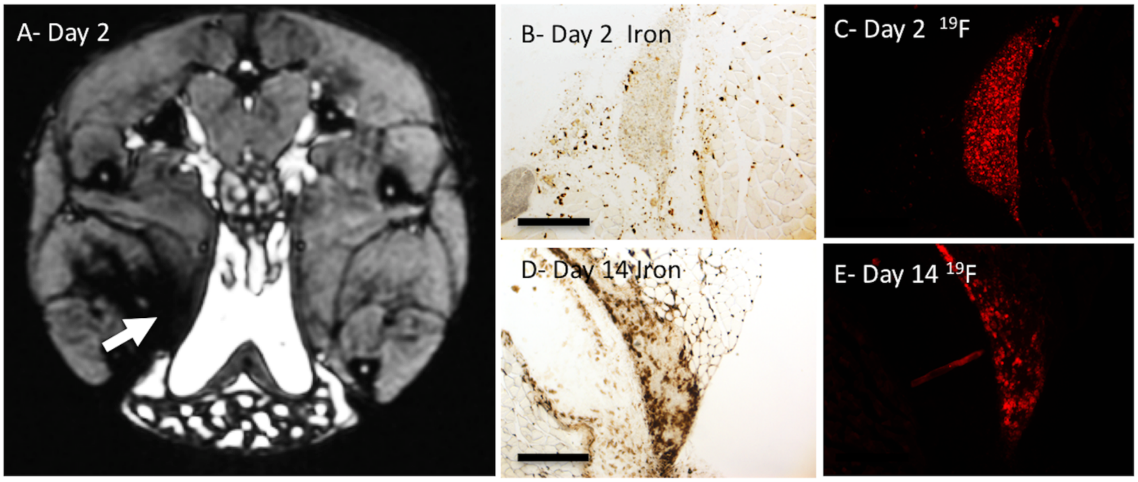

Figure 23: Signal void is visible in the axial proton images of the muscle after stem cell transplant on day 2 (A). The transplant site is denoted by the white arrow. No signal void is visible in the opposite, untreated, hindlimb muscle. Histology reveals the presence of iron within the muscle tissue on both day 2 (B) and day 14 (D). Scale bars denote 300µm. The accompanying stem cell track is outlined by the red fluorescent ^{19}F agent (C,E). More iron is found within the stem cell track at endpoint compared to day 2; often colocalized with the ^{19}F agent. suggesting it is contained within bystander labeled immune cells.

4.4 Discussion

In this study, the use of two different cellular MRI agents for tracking distinct cell populations was investigated. Pre-labeling of hMSC with a ^{19}F-agent provided specific and quantifiable information through the direct detection of the ^{19}F spins. Intravenous administration of USPIO allowed for the in vivo detection of hMSC rejection through the tracking of infiltrating of iron-labeled macrophages which were visualized in proton images as signal loss, and which impacted the ^{19}F signal from hMSC through ^{19}F signal quenching.

In agreement with previous studies[27], we have shown an excellent correlation between the number of transplanted cells and the ^{19}F-MRI quantification on day 0 following pre-labeling of stem cells with ^{19}F. This highlights an advantage of ^{19}F-MRI, that cellular delivery to the target can be confirmed through localization and quantification of ^{19}F-labeled stem cells soon after transplant. In a previous study, stem cell survival and label retention was demonstrated immediately following transplantation into a murine host[27]. The change in ^{19}F-signal over time also provides longitudinal information on the status of therapy. A reduction in ^{19}F-signal at the injection site suggests stem cells are either migrating away from, or dying, at the therapeutic site. Due to the immune competent xenograft model investigated, this decrease is likely predominately due to stem cell death and label clearance, as opposed to stem cell migration away from the injection tract[46]. As transplanted cells die the ^{19}F signal will be reduced as the label is cleared from the local tissue. In this study, a decrease in ^{19}F signal was observed for all Group A mice by MRI and fluorescence microscopy over the 14 days. Microscopy and immunohistochemistry indicated that macrophages are present at the transplant site in Group A mice as early as day 2 and that the majority are ^{19}F positive at the endpoint on day 14, in a process known as bystander labeling. The steady decrease in ^{19}F signal over time measured by MRI in Group A suggests that ^{19}F labeled macrophages must be leaving the site. By day 14 since most macrophages are ^{19}F positive, stem cell survival at our endpoint is being overestimated by ^{19}F MRI.

In Group B, the observation of signal voids in proton images in the muscle after i.v.

USPIO is consistent with the infiltration and accumulation of iron-labeled macrophages. Previous studies which used i.v. USPIO have shown similar results, and have suggested that imaging macrophages this way could be used as an early indication of transplant rejection[30]. In our study, coincident with the detection of signal loss in proton images was a significant decrease in ^{19}F-MRI signal from the stem cells. This is the result of quenching of the ^{19}F signal by USPIO-labeled cells. After the large reduction in the ^{19}F signal on day 2, post i.v. USPIO, the ^{19}F signal did not change any further (day 2 to day 14). This observation differed from the steady signal decline observed within Group A, and is likely due to the inability to accurately quantify ^{19}F signal following the influx of iron oxide to the site of transplant. In the presence of iron oxide, the ^{19}F signal is not linearly related to the concentration of ^{19}F spins and localized changes in relaxation rates render signal comparison to the external ^{19}F reference tube invalid. Longitudinal changes in ^{19}F signal are further complicated due to the saturation of signal quenching in the presence of large quantities of iron oxide, which may mask changes in iron-labeled cells over time[3]. Nevertheless, the significant effect on ^{19}F signal is advantageous in rapidly detecting the onset of acute inflammation.

Quenching of ^{19}F signal was first reported in a study by Hitchens et al. that explored the quenching of signal when ^{19}F-labeled cells are co-labeled with iron nanoparticles[45]. They showed that the ^{19}F T2 was significantly reduced in cells that were labeled with both iron and ^{19}F, but that iron-labeled cells mixed equally with ^{19}F-labeled cells did not impact the ^{19}F T2. To test the feasibility of detecting different ^{19}F labeled cells in vivo they used a mouse inflammation model where ^{19}F and/or USPIO was injected i.v. to label macrophages. Mice were either administered both the ^{19}F agent and USPIO i.v. at the same time or the ^{19}F agent one day and USPIO the next day to try to generate co-labeled or co-localized cell populations. More ^{19}F signal quenching was observed when both agents were administered simultaneously (co-labeled). Quenching was also observed for co-localized cells in gradient echo Fast Low Angle SHot (FLASH) images, but not in spin echo Rapid Acquisition with Relaxation Enhancement (RARE) images[45]. These important observations set the stage for the work we present here in a mouse model of stem cell transplantation and rejection.

Our *in vivo* results and supportive microscopy suggests that iron-labeled cells nearby ^{19}F-labeled cells (co-localized), and cells which are co-labeled with iron and ^{19}F, both cause quenching of the ^{19}F signal with our bSSFP imaging protocol. The bSSFP sequence is a rapid gradient echo imaging method with balanced gradient waveforms, which establishes a unique steady state[47]. bSSFP has features of both gradient and spin echo sequences and image contrast that is predominately related to T2/T1, but can be a combination with spin-density under some imaging conditions[48]. Our observation of signal quenching may also be due to the differences in spatial proximity and iron concentration present *in vivo* due to the infiltration of immune cells. Since MRI signal loss is only linearly related to iron oxide concentration at very low concentrations, the influx of additional iron oxide over time may not lead to a further decrease in signal[3]. Future work is required to better understand signal quenching with bSSFP and to determine if there is a minimum distance required to distinguish co-localized from co-labeled cells.

4.5 Conclusions

In summary, this study investigated the use of two cellular MRI approaches to track distinct cell types. Stem cells were pre-labeled and directly detected and quantified with ^{19}F-MRI over time and macrophages were labeled in situ using iron oxide nanoparticles and imaged with proton MRI to detect the infiltration of immune cells at the transplant site. To the best of our knowledge this is the first study that has used both proton and ^{19}F MRI to track two different cell types in vivo with multiple cellular MRI mechanisms.

By combining these well studied MRI cell tracking methodologies, it is possible to non-invasively verify both treatment delivery with ^{19}F-MRI and to monitor transplant rejection status with iron nanoparticles. Ultimately, through this technique it may be possible to obtain additional information on the rejection process and on the ultimate fate of transplanted stem cells.

4.6 References

1. Shapiro EM, Sharer K, Skrtic S, Koretsky AP. In vivo detection of single cells by

MRI. Magnetic Resonance in Medicine. 2006;55(2):242–9.

2. Heyn C, Ronald J a, Mackenzie LT, MacDonald IC, Chambers AF, Rutt BK, Foster PJ. In vivo magnetic resonance imaging of single cells in mouse brain with optical validation. Magnetic Resonance in Medicine. 2006;55(1):23–9.
3. Heyn C, Bowen C V, Rutt BK, Foster PJ. Detection threshold of single SPIO-labeled cells with FIESTA. Magnetic Resonance in Medicine. 2005;53(2):312–20.
4. Fox MS, Gaudet JM, Foster PJ. Fluorine-19 MRI Contrast Agents for Cell Tracking and Lung Imaging. 2015;8:1–15.
5. Bulte JWM, Walczak P, Janowski M, Krishnan KM, Arami H, Halkola A, Gleich B, Rahmer J. Quantitative "Hot Spot" Imaging of Transplanted Stem cells using Superparamagnetic Tracers and Magnetic Particle Imaging (MPI). Tomography. 2015;8(12):1699–1712.
6. Nejadnik H, Castillo R, Daldrup-Link HE. Magnetic Resonance Imaging and Tracking of Stem Cells. Methods in Molecular Biology. 2013;1(1052):167–176.
7. Xu C, Miranda-Nieves D, Ankrum J a, Matthiesen ME, Phillips J a, Roes I, Wojtkiewicz GR, Juneja V, Kultima JR, Zhao W, et al. Tracking mesenchymal stem cells with iron oxide nanoparticle loaded poly(lactide-co-glycolide) microparticles. Nano letters. 2012;12(8):4131–9.
8. Gonzalez-Lara LE, Xu X, Hofstetrova K, Pniak A, Chen Y, McFadden CD, Martinez-Santiesteban FM, Rutt BK, Brown A, Foster PJ. The use of cellular magnetic resonance imaging to track the fate of iron-labeled multipotent stromal cells after direct transplantation in a mouse model of spinal cord injury. Molecular Imaging and Biology. 2011;13(4):702–11.
9. Helfer BM, Balducci A, Sadeghi Z, O'Hanlon C, Hijaz A, Flask C a, Wesa AK. (19)F MRI tracer preserves in vitro and in vivo properties of hematopoietic stem cells. Cell transplantation. 2013;22(1):87–97.
10. Partlow KC, Chen J, Brant J a, Neubauer AM, Meyerrose TE, Creer MH, Nolta J a, Caruthers SD, Lanza GM, Wickline S a. 19F magnetic resonance imaging for stem/progenitor cell tracking with multiple unique perfluorocarbon nanobeacons.

The FASEB Journal. 2007;21(8):1647–54.

11. Psaltis P, Zannettino A. Concise review: mesenchymal stromal cells: potential for cardiovascular repair. Stem Cells. 2008:2201–2210.
12. Keating A. Mesenchymal stromal cells: new directions. Cell Stem Cell. 2012;10(6):709–16.
13. Segers VFM, Lee RT. Stem-cell therapy for cardiac disease. Nature. 2008;451(7181):937–42.
14. Boehm-Sturm P, Aswendt M, Minassian A, Michalk S, Mengler L, Adamczak J, Mezzanotte L, Löwik C, Hoehn M. A multi-modality platform to image stem cell graft survival in the naïve and stroke-damaged mouse brain. Biomaterials. 2014;35(7):2218–26.
15. Khabbal J, Kerkelä E, Mitkari B, Raki M, Nystedt J, Mikkonen V, Bergström K, Laitinen S, Korhonen M, Jolkkonen J. Differential Clearance of Rat and Human Bone Marrow-Derived Mesenchymal Stem Cells from the Brain After Intra-arterial Infusion in Rats. Cell transplantation. 2014 Mar 3.
16. Murphy SP, Porrett PM, Turka L a. Innate immunity in transplant tolerance and rejection. Immunological reviews. 2011;241(1):39–48.
17. Reagan MR, Kaplan DL. Concise review: Mesenchymal stem cell tumor-homing: detection methods in disease model systems. Stem cells (Dayton, Ohio). 2011;29(6):920–7.
18. Lauber K, Blumenthal SG, Waibel M, Wesselborg S. Clearance of Apoptotic Cells : Getting Rid of the Corpses The efficient elimination of apoptotic cells is crucial. Molecular Cell. 2004;14:277–287.
19. Wyburn KR, Jose MD, Wu H, Atkins RC, Chadban SJ. The Role of Macrophages in Allograft Rejection. Transplantation. 2005;80(12):1641–1647.
20. Auchincloss H, Sachs DH. Xenogeneic transplantation. Annual review of immunology. 1998;16:433–470.
21. Akira S, Uematsu S, Takeuchi O. Pathogen recognition and innate immunity. Cell.

2006;124(4):783–801.

22. Noad J, Gonzalez-Lara LE, Broughton HC, McFadden C, Chen Y, Hess D a, Foster PJ. MRI tracking of transplanted iron-labeled mesenchymal stromal cells in an immune-compromised mouse model of critical limb ischemia. NMR in Biomedicine. 2013;26(4):458–67.

23. Amsalem Y, Mardor Y, Feinberg MS, Landa N, Miller L, Daniels D, Ocherashvilli A, Holbova R, Yosef O, Barbash IM, et al. Iron-oxide labeling and outcome of transplanted mesenchymal stem cells in the infarcted myocardium. Circulation. 2007;116(11 SUPPL. 1):38–46.

24. Terrovitis J, Stuber M, Youssef A, Preece S, Leppo M, Kizana E, Schär M, Gerstenblith G, Weiss RG, Marbán E, et al. Magnetic resonance imaging overestimates ferumoxide-labeled stem cell survival after transplantation in the heart. Circulation. 2008;117(12):1555–62.

25. Berman SC, Galpoththawela C, Gilad AA, Bulte JWM, Walczak P. Long-term MR cell tracking of neural stem cells grafted in immunocompetent versus immunodeficient mice reveals distinct differences in contrast between live and dead cells. Magnetic Resonance in Medicine. 2011;65(2):564–574.

26. Bernau K, Lewis CM, Petelinsek AM, Reagan MS, Niles DJ, Mattis VB, Meyerand ME, Suzuki M, Svendsen CN. *In Vivo* Tracking of Human Neural Progenitor Cells in the Rat Brain Using Magnetic Resonance Imaging is Not Enhanced by Ferritin Expression. Cell Transplantation. 2015;25:575–592.

27. Gaudet JM, Ribot EJ, Chen Y, Gilbert KM, Foster PJ. Tracking the Fate of Stem Cell Implants with Fluorine-19 MRI. Plos One. 2015;10:e0118544.

28. Ribot EJ, Gaudet JM, Chen Y, Gilbert KM, Foster PJ. In vivo MR detection of fluorine-labeled human MSC using the bSSFP sequence. International Journal of Nanomedicine. 2014;9:1731–9.

29. Zhang Y, Dodd SJ, Hendrich KS, Williams M, Ho C. Magnetic resonance imaging detection of rat renal transplant rejection by monitoring macrophage infiltration. Kidney International. 2000;58(3):1300–1310.

30. Khurana a., Nejadnik H, Gawande R, Lin G, Lee S, Messing S, Castaneda R, Derugin N, Pisani L, Lue TF, et al. Intravenous Ferumoxytol Allows Noninvasive MR Imaging Monitoring of Macrophage Migration into Stem Cell Transplants. Radiology. 2012;264(3):803–811.

31. Wu Y, Ye Q, Eytan DF, Liu L, Rosario BL, Hitchens TK, Yeh F-C, van Rooijen N, Ho C. MRI Investigation of Macrophjages in acute cardiac allograft rejection after heart transplantation. Circulation: Cardiovascular Imaging. 2011;72(2):181–204.

32. Kanno S, Wu YJ, Lee PC, Dodd SJ, Williams M, Griffith BP, Ho C. Macrophage accumulation associated with rat cardiac allograft rejection detected by magnetic resonance imaging with ultrasmall superparamagnetic iron oxide particles. Circulation. 2001;104(8):934–938.

33. Iv M, Telischak N, Feng D, Holdsworth S., Yeom K., Daldrup-Link H. Clinical applications of iron oxide nanoparticles for magnetic resonance imaging of brain tumors. Nanomedicine (Lond). 2015;10(6):993–1018.

34. Vasanawala SS, Nguyen K-L, Hope MD, Bridges MD, Hope TA, Reeder SB, Bashir MR. Safety and technique of ferumoxytol administration for MRI. Magnetic Resonance in Medicine. 2016;75(5):2107–2111.

35. Hitchens TK, Ye Q, Eytan DF, Janjic JM, Ahrens ET, Ho C. 19F MRI detection of acute allograft rejection with in vivo perfluorocarbon labeling of immune cells. Magnetic resonance in medicine. 2011;65(4):1144–53.

36. Ahrens ET, Young W, Xu H, Pusateri LK. Reports Rapid quantification of inflammation in tissue samples using perfluorocarbon emulsion and fluorine-19 nuclear magnetic resonance. BioTechniques Focus:Translational Tools. 2011:229–234.

37. Weise G, Basse-Luesebrink TC, Wessig C, Jakob PM, Stoll G. In vivo imaging of inflammation in the peripheral nervous system by (19)F MRI. Experimental neurology. 2011;229(2):494–501.

38. Jacoby C, Temme S, Mayenfels F, Benoit N, Krafft MP, Schubert R, Schrader J, Flögel U. Probing different perfluorocarbons for in vivo inflammation imaging by

(19) F MRI: image reconstruction, biological half-lives and sensitivity. NMR in Biomedicine. 2014;27(3):261–71.

39. Dayan V, Yannarelli G, Billia F, Filomeno P, Wang X-H, Davies JE, Keating A. Mesenchymal stromal cells mediate a switch to alternatively activated monocytes/macrophages after acute myocardial infarction. Basic research in cardiology. 2011;106(6):1299–310.

40. Helfer BBM, Balducci A, Nelson AD, Janjic JM, Gil RR, Kalinski P, Vries IJMDE, Ahrens ET, Mailliard RB, de Vries IJM. Functional assessment of human dendritic cells labeled for in vivo (19)F magnetic resonance imaging cell tracking. Cytotherapy. 2010;12(2):238–50.

41. Abràmoff MD, Magalhães PJ, Ram SJ. Image processing with imageJ. Biophotonics International. 2004;11(7):36–41.

42. Schneider C a, Rasband WS, Eliceiri KW. NIH Image to ImageJ: 25 years of image analysis. Nature Methods. 2012;9(7):671–675.

43. Srinivas M, Morel PA, Ernst L a, Laidlaw DH, Ahrens ET. Fluorine-19 MRI for visualization and quantification of cell migration in a diabetes model. Magnetic Resonance in Medicine. 2007;58(4):725–34.

44. Boehm-Sturm P, Mengler L, Wecker S, Hoehn M, Kallur T. In Vivo Tracking of Human Neural Stem Cells with 19F Magnetic Resonance Imaging. PloS ONE. 2011;6(12):e29040.

45. Hitchens TK, Liu L, Foley LM, Simplaceanu V, Ahrens ET, Ho C. Combining Perfluorocarbon and Superparamagnetic Iron-Oxide Cell Labeling for Improved and Expanded Applications of Cellular MRI. Magnetic Resonance in Medicine. 2015;73(1):367–375.

46. Eggenhofer E, Luk F, Dahlke MH, Hoogduijn MJ. The life and fate of mesenchymal stem cells. Frontiers in Immunology. 2014;5(MAY):1–6.

47. Scheffler K, Lehnhardt S. Principles and applications of balanced SSFP techniques. European Radiology. 2003;13(11):2409–18.

48. Huang TY, Huang IJ, Chen CY, Scheffler K, Chung HW, Cheng HC. Are trueFISP

images T2/T1-weighted? Magnetic Resonance in Medicine. 2002;48(4):684–688.

Chapter 5

5 Translation of High-field Fluorine-19 Cell Tracking into the Clinical Realm

5.1 Introduction

Application of non-invasive, non-toxic, *in vivo* imaging is essential to the future of improving cellular therapy. By developing cellular MRI, it might one day be possible to rapidly determine if a patient will respond to treatment through diagnostic imaging, without waiting for symptomatic signs. Clinical trial outcomes could be improved by separating non-responders from those with an unsuccessful cell injection.

The first clinical application of MRI cell tracking was in verifying DC administration for melanoma immunotherapy[1]. Dendritic cells are ideally suited for cell tracking translation due to their clinical relevance and reliance on migration to the lymph node. In 2005, de Vries et al. tracked mixed SPIO- and ^{111}In-labeled DC injected intranodally under ultrasound guidance.[1] In this study, MRI was found to be at least as sensitive as scintigraphic images, with significant improvements in spatial localization. MRI also showed that a large percentage of guided injections had missed their target injection site, highlighting the application of cellular MRI in verifying treatment delivery. Since 2005, iron-based cellular MRI has been used clinically to track a variety of cell types, in addition to dendritic cells,[2] such as: neural stem cells,[3,4] hematopoietic stem cells,[5] and pancreatic islet grafts.[6] Yet despite the large potential, wide-spread clinical use of iron oxide based cellular MRI has not been achieved. This is largely due to the unavailability of a commercial, FDA approved imaging agent. In 2008, Feridex™ an iron-based MRI reticuloendothelial system contrast agent, was taken off market. Up until this point Feridex had been used off-label in the majority of cell tracking trials.

In 2014, the first ^{19}F-MRI clinical cell tracking trial was performed using a commercial perfluorocarbon imaging agent, Cell Sense, to track the administration of DC in patients with colorectal cancer.[7] Dr. Ahrens' group observed an average of $3.9\text{x}10^{12}$ ^{19}F/cell, with no decrease in cell viability or changes to phenotype. A Fast Low Angle SHot (FLASH) imaging sequence was used on a Siemens 3T clinical MRI system with a ^{19}F-scan time of 9.5 minutes. Patients received either a low dose (1x10^{6} DC, N=2) or a high dose (1x10^{7} DC, N=3) and imaging was performed twice, 4 and 24 hours after administration. ^{19}F signal was only detected at the injection site in high dosage patients. Quantification of signal at the injection site showed that the ^{19}F-MRI signal decreased by approximately 50% between the two imaging time points. This suggested that DC migrated from the initial site. However, no signal was observed in the nearby lymph nodes, likely due to the limited sensitivity. Recently a ^{19}F clinical protocol for imaging Stromal Vascular Fraction (SVF) cells was published.[8] With applications in breast reconstruction, the SVF is comprised of a heterogeneous mixture of cells, with a large percentage of adipose derived stem cells. Extensive work was performed to show no phenotypic changes from labeling. Preferential ^{19}F uptake was observed within some cells, with an average overall cellular loading of 2.8±2x10^{12} ^{19}F/cell. Dr. Bulte's group was able to show a detection limit of 2x10^{6} SVF cells implanted 5mm below the surface of the phantom, however no signal was observed from a similar injection 1cm deep.

In this study, we sought to develop the first clinical ^{19}F-cell tracking imaging protocol in Canada for imaging peripheral blood mononuclear cells (PBMC). Used in the first FDA approved anticancer vaccine, sipuleucel-T cell therapy targets castration resistant prostate cancer. Autologous PBMC are collected and incubated with a fusion protein containing prostatic acid phosphatase (PAP) antigen linked to granulocyte-macrophage colony-stimulating factor (GM-CSF), prior to administration back into the patient.[9] Success of therapy relies on the migration of these PBMC to secondary lymphoid organs such as the inguinal lymph nodes in the upper thigh.[10] In this work we present an imaging pipeline allowing for treatment to be first developed and optimized in pre-clinical models, then translated to a clinical protocol. Migration of ^{19}F-labeled PBMC to the draining lymph node was demonstrated in mice to show that treatment could be developed and optimized in high throughput pre-clinical models. PBMC were imaged with a clinical protocol following injection into a ham shank phantom to simulate the human thigh.

5.2 Methods

5.2.1 Labeling of PBMC with Cell Sense

Blood from C57Bl/6 mice was collected by venous puncture, according to animal use protocols approved by Western University Animal Use Committee. Human peripheral blood mononuclear cells (hPBMCs) were collected from two healthy volunteers who had consented to a protocol approved by the University of Western Ontario Research Ethics Board (London, ON, Canada). Approximately 100 - 160 mL of blood was drawn following hospital procedure. In both cases, PBMCs were isolated from the blood using gradient centrifugation via a Ficoll overlay. PBMC were washed in HBSS and re-suspended in AIM-V® Medium CTS at $5x10^6$ cells/mL in 1 well of a 12 well plate (Falcon, Mississauga, Canada). Cells were labeled with 5mg/mL of Cell Sense (CS-1000), overnight prior to administration. Following labeling, an aliquot of cells was set aside in each experimental repetition of determination of intracellular ^{19}F content.

5.2.2 Pre-clinical MRI of PBMC Migration

Male nu/nu mice (8-10 weeks) (n=20) were purchased from Charles River Laboratories Inc. (Saint Constant, Canada) and housed at Robarts Research Institute at Western University (London, Canada) in a pathogen-free barrier facility. Animal use guidelines were followed for all experiments conducted and pre-approved by the Animal Use Subcommittee at Western University. In each mouse, the right lymph node was pre-treated with the pro-inflammatory agent IL-1β prior to PBMC administration. This agent is expected to increase lymphatic drainage to the node, potential promoting the number of PBMC which arrive. $5\text{-}6x10^6$ ^{19}F-labeled mPBMC were injected into each of the right and left footpads, 48 hours prior to imaging. In 10 animals, mPBMC were matured with GM-CSF, prior to administration but after ^{19}F-labeling. By maturing the PBMC, they are more likely to migrate to the draining lymph node and stimulate the immune system. This produced four treatment models in the mice; 1) Untreated PMBC, 2) GM-CSF+ matured PBMC, 3) IL-1β treated lymph nodes, and 4) GM-CSF+ PBMC & IL-1β treated LN. The frequency of signal detection and quantity of migrating cells to the lymph node were compared between the four treatments.

Murine imaging was performed with a 9.4T Varian small-animal MRI scanner. A 3D-balanced steady state free precession (bSSFP) sequence was used for both ^{1}H and ^{19}F imaging. Animals were imaged alongside an agarose diluted Cell Sense reference tube of known ^{19}F concentration (3.33x10^{16} ^{19}F/µL). Mice were anesthetized with 2% isoflurane, with breathing rate and temperature monitored throughout the scan. MRI was performed using a dual-tuned birdcage volume coil (diameter 2.2cm, length 5.1cm), tuned to 400.2 MHz and 376.8 MHz for ^{1}H and ^{19}F imaging respectively. For ^{1}H imaging the scan parameters were: repetition time (TR)=5.0ms, echo time (TE)=2.5ms, receiver bandwidth (rBW)=78kHz, flip angle (FA)=30°, phase cycles (PC)=4, averages=3, resolution=200x200x200µm^{3}. For ^{19}F imaging the parameters were: TR=4.0ms, TE=1.9ms, rBW=25kHz, FA=70°, PC=4, averages=250, resolution=1x1x1mm^{3}. Total protocol time for both ^{1}H and ^{19}F imaging was under 90 minutes.

5.2.3 Clinical MRI Protocol

Samples were imaged with a GE MR750, 3 Tesla (T) MRI scanner equipped with a multinuclear pre-amplifier. Imaging was performed with two dual ^{1}H/^{19}F-tuned switchable surface coils manufactured by Clinical MR solutions. Detection sensitivity between a large coil (25.4cm x 17.8cm) was compared to a small coil (4.3cm x 4.3cm) with two arrays of trifluoroacetic acid (TFA) samples ranging from 0.0001%-1% with a volume of 1mL and 15mL. Based on these results, the small coil was used for all further experiments. Image acquisition was further optimized with hPBMC cell pellets containing 1-10x10^{6} cells. A 2D fast gradient echo (Fast GRE) sequence was used for ^{1}H imaging with the following scan parameters: TE = 2.6ms, TR = 100ms, field of view (FOV) = 15cm x 15cm x 5cm, Image Matrix = 256x256, Slice thickness = 5mm, rBW = 83kHz, and FA = 20°. Following ^{1}H imaging, the coil was switched to ^{19}F-mode and the same FOV was scanned. ^{19}F images were obtained with a broad-banded 3D balanced Steady State Free Precession (bSSFP) based on the GE FIESTA-C sequence. The scan parameters were: TE= 2.2ms, TR= 4.4ms, FOV= 15cm x 15cm x 5cm, Image matrix = 46x46, Slice thickness = 5mm, rBW= 10kHz, and FA= 70°. ^{19}F imaging time was 15 minutes, with a total protocol time under 30 minutes. Clinical proof-of-concept imaging was performed with a ham shank phantom. PBMC from a healthy volunteer were labeled with Cell Sense (5mg/mL) for 48 hours. Realistic mock injections consisting of 1, 4.5, 10.5, and 20 x10^6 PBMC were performed by injecting ^{19}F-labeled cells into the ham shank at two depths. A shallow intradermal injection was performed at approximately 3mm depth along with a subcutaneous injection at 1cm depth. The study was repeated with PBMC from a second volunteer.

5.2.4 Cellular Loading Efficiency and Signal Quantification

The mean intracellular ^{19}F content of the PBMC mixture was determined by Nuclear Magnetic Resonance (NMR) spectroscopy. First, a known number of cells were fixed, then lysed through repeated cycles of sonication and freeze-thaw in solution containing 100μL 5% Triton X-100. After lysing, 300μL of D_20 and 100μL of 0.1% TFA were added to the solution. The TFA provides a reference peak for quantifying the number of ^{19}F spins/ cell, since NMR signal is linearly dependent on the number of ^{19}F atoms present.

For *in vivo* MRI signal quantification, the number of PBMC was determined with Voxel Tracker^{TM} software. Prior to analysis, a signal correction was applied to the ^{19}F datasets by subtracting the signal value of the voxel containing the lowest signal in the dataset. Once the correction was applied, the total ^{19}F-labeled cell signal contained within a hand-drawn ROI was compared to the average signal produced by a reference tube of known concentration (3.33x10^{16} ^{19}F spins/μL). This information was used alongside the ^{19}F/cell, measured with NMR, to quantify the apparent number of cells located at the ROI.

5.3 Results

Pre-clinical imaging of mPBMC

For pre-clinical experiments either naïve PBMCs or GM-CSF exposed matured PBMCs were injected into the footpad. In all cases ^{19}F-signal was observed in both footpads of the mice. The number of detected mPBMC in the draining popliteal LN is outlined in Table 4. When signal was detected, there was no significant difference in the number of migrating PBMC under any condition. There is no difference in the frequency of ^{19}F signal detection based on either cell maturation with GM-CSF (Table 4, column 1), node pre-treatment with IL-1β (Table 4, column 2), or treatment with both GM-CSF and IL-1β (Table 4, column 3). However, there was a significant difference in detection frequency when compared to the untreated controls (Table 4, column 4).

Table 4: Summary of pre-clinical mPBMC migration to popliteal lymph nodes

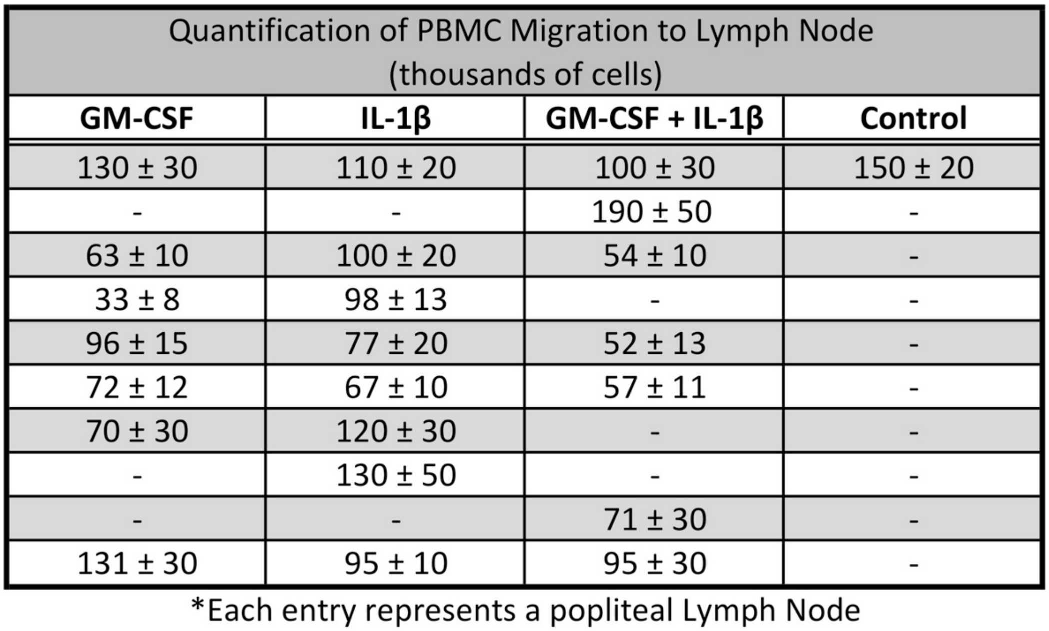

Quantification of PBMC Migration to Lymph Node
(thousands of cells)

GM-CSF	IL-1β	GM-CSF + IL-1β	Control
130 ± 30	110 ± 20	100 ± 30	150 ± 20
-	-	190 ± 50	-
63 ± 10	100 ± 20	54 ± 10	-
33 ± 8	98 ± 13	-	-
96 ± 15	77 ± 20	52 ± 13	-
72 ± 12	67 ± 10	57 ± 11	-
70 ± 30	120 ± 30	-	-
-	130 ± 50	-	-
-	-	71 ± 30	-
131 ± 30	95 ± 10	95 ± 30	-

*Each entry represents a popliteal Lymph Node

Imaging of hPBMC under clinical conditions

Imaging translation was performed with a clinical-strength 3T GE MRI (Fig 24A), with a custom-designed 4.3cm dual-tuned $^{19}F/^{1}H$ surface coil (Fig 24B). Using the 7-channel GE body coil, human inguinal lymph nodes could be detected as dark spheres within the bright fat pad in the upper thigh (Fig 24C/D). 12 nodes were detected with an average volume of 390±290mm^3 and an average depth of 1.5±0.3cm. In a clinical trial, these high quality body coil images could be used to localize the target imaging area. Prior to image optimization, the difference in detection sensitivity between the large and small coils was estimated with an array of TFA phantoms. Here, the small surface coil displayed a higher sensitivity, by almost two orders of magnitude (Fig 25A). However, the effective imaging depth was significantly decreased, limiting the small coil to superficial imaging sites. ^{19}F imaging parameters were optimized on the small coil using a series human PBMC cell pellet phantoms ranging from 1-10 x10^6 cells (Fig 25C).

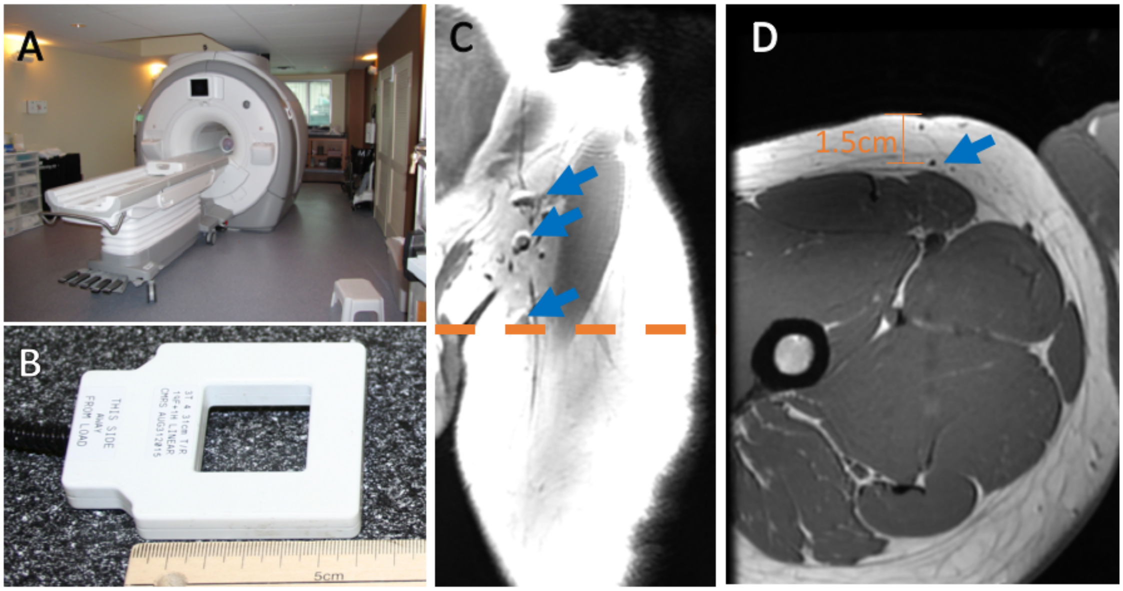

Figure 24: MRI provides excellent soft tissue contrast and lymph node detection. Imaging protocol has been developed for a clinical 3T GE MRI (A). ^{19}F imaging is performed with a small dual-tuned surface coil placed on the patients upper thigh, centered on the injection point (B). A coronal orientation MRI with the body coil reveals the lymph nodes as dark spheres [blue arrow] within the fat of the upper thigh (C). The orange dashed line indicates the location of the axial MRI slice (D). In the axial image, the nodes were measured to be approximately 1.5cm below the skin (D).

The pelleted cells were contained within individual Eppendorf tubes with 1% agarose poured on top to hold them in place. Under optimum labeling conditions, with $4.2\text{x}10^{11}$ ^{19}F/cell, as few as $1\text{x}10^{6}$ PBMC could be detected (Fig 25D).

As a proof-of-concept, human PBMC were administered into a ham shank prior to imaging with the dual-tuned surface coil (Fig 26). The ham shank Human PBMC were ^{19}F-labeled (mean $1.2\text{x}10^{11}$ ^{19}F/cell) and administered intradermally in 4 doses: 1.5, 4.5, 10.5 and 20 $\text{x}10^{6}$ cells (Fig 26A/B). With PBMC from the first donor, all injections were detectable and quantifiable with the exception of the lowest $1.5\text{x}10^{6}$ PBMC dose. In addition, a subcutaneous injection of $4.5\text{x}10^{6}$ PBMC was placed below the intradermal dose. This site was also visible 1.2cm below the surface (Fig 26B). The ^{19}F/^{1}H dual-tuned coil was placed on the surface above the target location, as shown (Fig 26C). ^{1}H images of the ham shank provided a realistic tissue model, as shown by the images of the human thigh with the same coil (Fig 26D).

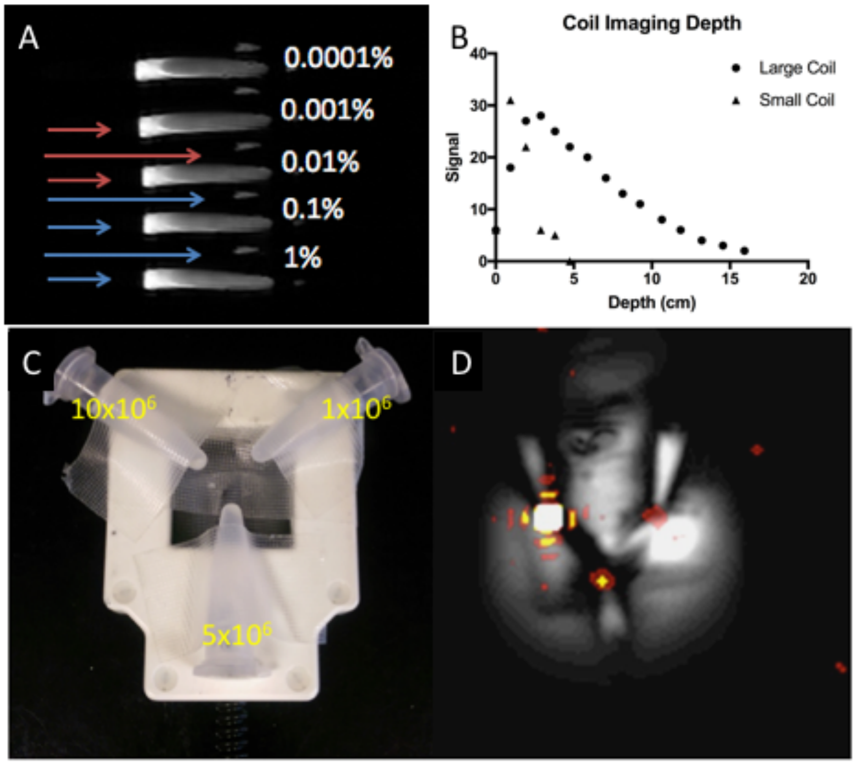

Figure 25: An array of phantoms containing 0.0001%-1% TFA in 1mL and 15mL tubes imaged with both the large and small surface coils (A). In the sagittal proton image of this phantom, the blue arrows indicate tubes that were detectable with both coils, but only the small surface coil displayed sufficient sensitivity to detect those marked by the red arrows. The lowest concentration detected, 0.001% represents the signal on the same order of magnitude of a million PBMC. Using the smaller coil did result in a significant increase in signal drop off with depth compared to the larger coil (B). Cell pellet phantoms created by centrifuging 1x10^6, 5x10^6 and 10x10^6 Cell Sense-labeled PBMC and overlaying with 1% agarose in an eppendorf tube (C). PBMC phantoms were placed on a saline bag and scanned at 3T and all 3 phantoms described in (C) were detected using ^{19}F cellular MRI (D), with a hot-iron colour scale used for ^{19}F MRI.

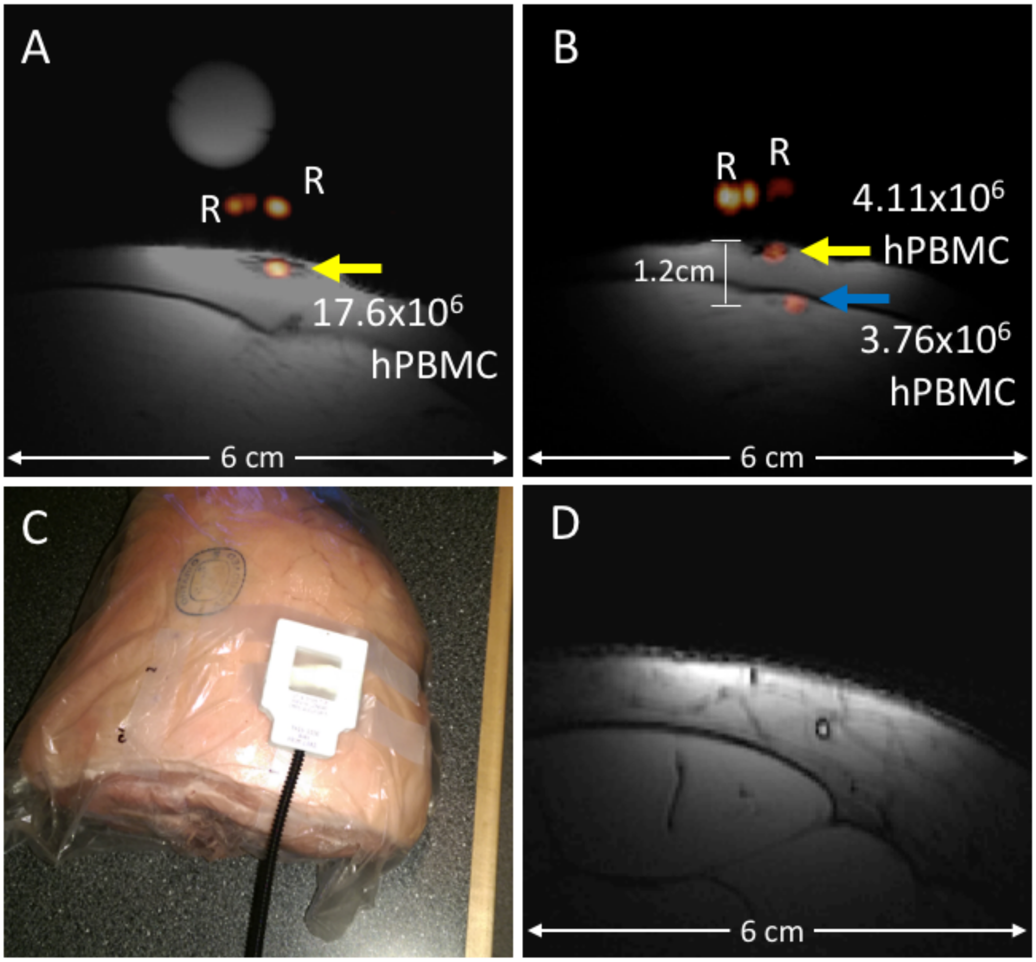

Figure 26: Human PBMC can be detected under clinical conditions following injection into a ham shank. Cells were administered interdermally in 4 doses [yellow arrows], 20x10^6 (A), 10.5x10^6 (not shown), 4.5x10^6 (B) and 1.5x10^6. Only the smallest dose (1.5x10^6) was undetectable with our imaging parameters. An additional 4.5x10^6 dose was administered subcutaneously [blue arrow], which is visible at 1.2cm depth as measured with MRI. Images were performed alongside a pair of reference tubes (R) of known ^{19}F concentration allowing for signal quantification. The surface coil was placed directly on the ham shank, with the reference tubes taped inside the coil elements (C). A representative human ^{1}H image taken with the same parameters closely resembles the ham images in both tissue appearance and subcutaneous fat disposition (D).

When the experiment was repeated with PBMC from a different source labeling efficiency was observed to be much lower ($4.2x10^{10}$ ^{19}F/cell). A comparison of the $20x10^6$ PBMC dose is shown in Figure 27, where the images have been set to the same window and level. Under these conditions, only the $20x10^6$ PBMC dose was detectable (Fig 27B).

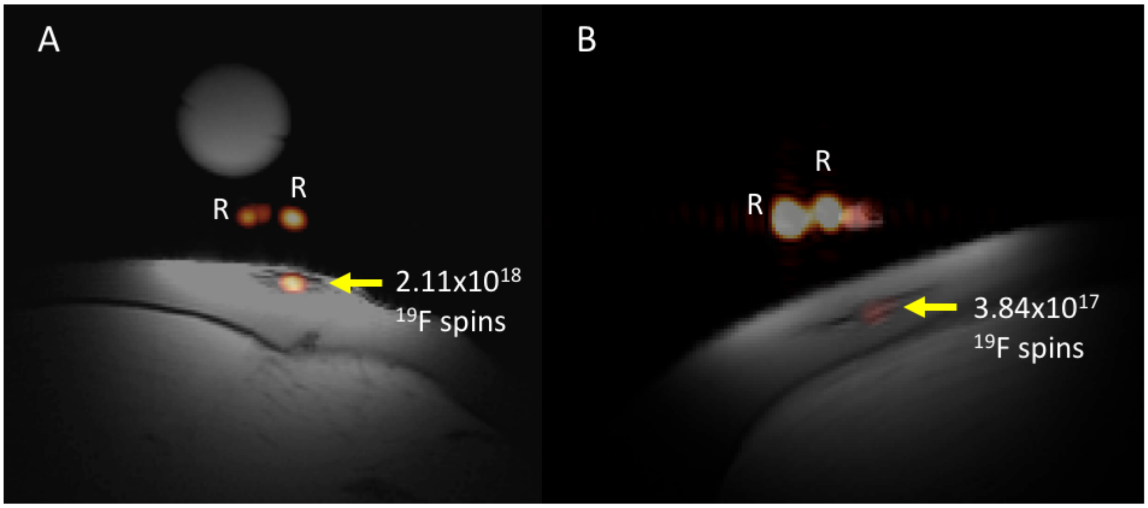

Figure 27: Comparison of signal produced by 20 million PBMC from two different donors. Two doses of $15x10^6$ PBMC were prepared from different sources. In the first, a high labeling efficiency ($1.2x10^{11}$ ^{19}F/cell) was observed producing a strong signal in the ham shank (A). The second source had a low labeling efficiency ($4.2x10^{10}$ ^{19}F/cell), resulting in a low observed signal (B).

5.4 Discussion

To our knowledge, this is the first study conducted where a primary PBMC and ^{19}F cellular MRI were used to track and quantify *in vivo* migration in a mouse model. The high throughput of small animal models allows for rapid testing and optimization of treatment. Our data showed that pretreatment with either GM-CSF or IL-1β enhanced migration to the draining LN. It is likely that some PBMC migration occurred to all of the nodes; but in some cases the signal was insufficient to reach the detection threshold necessary for ^{19}F-MRI. This is particularly relevant to the untreated control group where signal was only detected in a single node. Since treatment efficacy has been linked to the number of PBMC which ultimately reach the nodes,[11,12] improving migration efficiency and consistency is of the utmost importance to improving clinical outcomes.

The translational potential of ^{19}F-MRI was investigated with a clinical 3T MRI. At 3T, Cell Sense has been shown to have a T1 of 423ms and a T2 of 155ms, producing an ideal bSSFP flip angle of 62°,[13] which is in agreement with our observed optimal angle of 70°. It is interesting to note that sensitivity improved with higher resolution images (data not shown), in agreement with observations made at high-field and discussed in Section 2.2.2. For development of the clinical protocol, a ham shank phantom was used as a mock human leg due to the tissue similarities. The largest factor governing successful detection of PBMC was found to be the number of ^{19}F/cell. Mean intracellular loading of PBMC ranged from 10^{10} – 10^{11} between patients, representing an order of magnitude difference in cell detection threshold (10^7 vs 10^6 PBMC, respectively). Similar differences in intracellular uptake were also observed by Dr. Ahrens et al. when labeling DC with ^{19}F.[7] While in the development stages of clinical ^{19}F-MRI, it may be necessary to pre-screen patients on the basis of intracellular loading. In comparison to other clinical ^{19}F studies, PBMC were observed to label on average an order of magnitude lower than DC (3.9×10^{12} ^{19}F/cell)[7] and stromal vascular fraction cells ($2.8\pm2\times10^{12}$ ^{19}F/cell);[8] which translates into a proportional decrease in signal. Yet, despite this inherent disability, the minimum number of detectable cells was similar compared to previous studies (DC: ~5×10^6, SVF: 2×10^6, PBMC: 4.5×10^6). The clinical protocol and hardware presented in this work for imaging the ham shank represents a 10x improvement in sensitivity compared to previous studies (table 5).

This improvement in detection sensitivity is largely due to the small size of the surface coil used, as well as the higher number of imaging averages. We presented a significant improvement in detection sensitivity by using a small 4.3cm x 4.3 cm compared to a much larger 25.4cm x 17.8cm surface coil. However, this came along with a significant decrease in imaging depth; limiting the application to surface injections and superficial targets. Total imaging time was contained within the self-imposed clinical limit of 30minutes. However, despite these improvements sensitivity still represents the largest

Table 5: Overview of clinical ^{19}F cell tracking protocols published to date

Cell Type	Pulse Sequence & Imaging Time	Year	Reported Detection limit (^{19}F spins)
Dendritic Cell[7]	FLASH – 9.5min	2014	$\sim 1.85 \times 10^{19}$
Stromal Vascular Fraction[8]	bSSFP – 3.5min	2015	5.6×10^{18}
PBMC	bSSFP – 15min	2016	3.8×10^{17}

limitation of clinical ^{19}F-MRI. This is due to the fundamental low sensitivity of the NMR signal, where net magnetization is only increased by 1 per 20^5 spins at 1.5T. By comparison, the high sensitivity of iron-oxide based cellular MRI is due to the indirect detection of iron oxide through its influence on the highly abundant ^{1}H signal. Although magnetization increases linearly with field strength, the drive for clinical translation limits this to 3T in most situations. Several techniques, such as hyperpolarization, have been used with great success in other x-nuclei to temporarily increase magnetization. But the rapid loss of magnetization with time (order of seconds) makes this inapplicable with cell tracking. This is further complicated by the fact that only 5% of injected cells are expected to migrate to the lymph node. Based upon the sensitivity of this protocol, we can estimate that an initial subcutaneous injection of 90×10^6 PBMC would be required to detect migration of cells to a lymph node, assuming all PBMC migrated to a single node. Improvements in acquisition with different sequences, such as: ultrashort echo time (UTE)-SSFP,[14] advanced array coil configurations,[8,15] and post processing techniques, such as compressed sensing[16] will be required to increase sensitivity to the necessary levels. For now, migration of PBMC must be approximated based upon the decrease in ^{19}F signal at the injection site over time. Finally, the minimum number of detectable cells can be improved by increasing the amount of ^{19}F contained within a cell. Unfortunately, this is currently limited by phenotypic changes and decreasing viability when cells are forced to internalize more agent. The design of novel ^{19}F agents will be necessary to safely enhance uptake.

In this study, we present the highest sensitivity for ^{19}F detection reported thus far in the literature with a clinical protocol. Moreover, this is the first investigation to show quantifiable signal of ^{19}F labeled PBMC at a depth of 1.2cm using clinical ^{19}F MRI hardware and protocol, as all other studies have only detected signal of surface injected cells.[7,8] As outlined in Table 5, significant improvements in detection sensitivity have been made each year since the first clinical ^{19}F cellular MRI study. With the recent rapid expansion of the field, there is strong potential for development of the necessary technological advancements to help secure the role of ^{19}F in the clinical cell therapy realm.

5.5 References

1. de Vries IJM, Lesterhuis WJ, Barentsz JO, Verdijk P, van Krieken JH, Boerman OC, Oyen WJG, Bonenkamp JJ, Boezeman JB, Adema GJ, et al. Magnetic resonance tracking of dendritic cells in melanoma patients for monitoring of cellular therapy. Nature biotechnology. 2005;23(11):1407–13.

2. de Vries IJM, Lesterhuis WJ, Barentsz JO, Verdijk P, van Krieken JH, Boerman OC, Oyen WJG, Bonenkamp JJ, Boezeman JB, Adema GJ, et al. Magnetic resonance tracking of dendritic cells in melanoma patients for monitoring of cellular therapy. Nature biotechnology. 2005;23(11):1407–13.

3. Zhu J, Zhou L, XingWu F. Tracking neural stem cells in patients with brain trauma. The New England Journal of Medicine. 2006;355(22):2376–2378.

4. Janowski M, Walczak P, Kropiwnicki T, Jurkiewicz E, Domanska-Janik K, Bulte JWM, Lukomska B, Roszkowski M. Long-term MRI cell tracking after

intraventricular delivery in a patient with global cerebral ischemia and prospects for magnetic navigation of stem cells within the CSF. PloS one. 2014;9(2):e97631.

5. Callera F, de Melo CMTP. Magnetic resonance tracking of magnetically labeled autologous bone marrow CD34+ cells transplanted into the spinal cord via lumbar puncture technique in patients with chronic spinal cord injury: CD34+ cells' migration into the injured site. Stem cells and development. 2007;16(3):461–6.

6. Toso C, Vallee JP, Morel P, Ris F, Demuylder-Mischler S, Lepetit-Coiffe M, Marangon N, Saudek F, James Shapiro AM, Bosco D, et al. Clinical magnetic resonance imaging of pancreatic islet grafts after iron nanoparticle labeling. American Journal of Transplantation. 2008;8(3):701–706.

7. Ahrens ET, Helfer BM, O'Hanlon CF, Schirda C. Clinical cell therapy imaging using a perfluorocarbon tracer and fluorine-19 MRI. Magnetic Resonance in Medicine. 2014;0:n/a-n/a.

8. Rose L, Kadayakkara DKK, Wang G, Bar-Shir A, Helfer BM, O'Hanlon CF, Kraitchman DL, Rodriguez RL, Bulte JWM. Fluorine-19 Labeling of Stromal Vascular Fraction Cells for Clinical Imaging Applications. Stem Cells translational medicine. 2015:1–8.

9. Small EJ, Schellhammer PF, Higano CS, Redfern CH, Nemunaitis JJ, Valone FH, Verjee SS, Jones L a, Hershberg RM. Placebo-controlled phase III trial of immunologic therapy with sipuleucel-T (APC8015) in patients with metastatic, asymptomatic hormone refractory prostate cancer. Journal of clinical oncology : official journal of the American Society of Clinical Oncology. 2006;24(19):3089–94.

10. Dekaban GA, Hamilton AM, Fink CA, Au B, de Chickera SN, Ribot EJ, Foster PJ. Tracking and evaluation of dendritic cell migration by cellular magnetic resonance imaging. Wiley Interdisciplinary Reviews: Nanomedicine and

Nanobiotechnology. 2013;5(5):469–483.

11. Sabado R, Bhardwaj N. Directing dendritic cell immunotherapy towards successful cancer treatment. Immunotherapy. 2010;2(1):37–56.

12. Melief CJM. Cancer Immunotherapy by Dendritic Cells. Immunity. 2008;29(3):372–383.

13. Colotti R, Bastiaansen JAM, Wilson A, Flögel U, Gonzales C, Schwitter J, Stuber M, van Heeswijk RB. Characterization of perfluorocarbon relaxation times and their influence on the optimization of fluorine-19 MRI at 3 tesla. Magnetic Resonance in Medicine. 2016;0.

14. Goette MJ, Keupp J, Rahmer J, Lanza GM, Wickline S a, Caruthers SD. Balanced UTE-SSFP for (19) F MR imaging of complex spectra. Magnetic resonance in medicine : official journal of the Society of Magnetic Resonance in Medicine / Society of Magnetic Resonance in Medicine. 2014;0:1–7.

15. Ji Y, Waiczies H, Winter L, Neumanova P, Hofmann D, Rieger J, Mekle R, Waiczies S, Niendorf T. Eight-channel transceiver RF coil array tailored for ^{1} H/ ^{19} F MR of the human knee and fluorinated drugs at 7.0 T. NMR in Biomedicine. 2015;(April):n/a-n/a.

16. Zhong J, Mills PH, Hitchens TK, Ahrens ET. Accelerated fluorine-19 MRI cell tracking using compressed sensing. Magnetic resonance in medicine : official journal of the Society of Magnetic Resonance in Medicine / Society of Magnetic Resonance in Medicine. 2012;0:1–8.

Chapter 6

6 Summary and Future Work

This work is the first implementation of ^{19}F-MRI for cell tracking in Canada. Several advances to the field of cell tracking have been accomplished. First, Chapter 3 describes the first time the bSSFP pulse sequence was used to quantify ^{19}F-labeled MSC *in vivo.* In Chapter 4 we demonstrate the first time dual ^{19}F- and iron cellular MRI techniques were used for the simultaneous tracking of the fate of a stem cell transplant and the resulting cellular inflammatory response. Finally, in Chapter 5 we show first results of imaging of ^{19}F-labeled PBMC on a GE 3T clinical MRI system using a clinical imaging protocol. Detection sensitivity was improved upon by an order of magnitude based on previously published protocols.

6.1 Discussion and Conclusions

^{19}F-MRI is an emerging cell tracking technique, with excellent potential for clinical application. This thesis has aimed to advance the development of ^{19}F-MRI techniques and expand applications in both the pre-clinical and clinical realms. Developing a non-invasive, non-cytotoxic, and quantifiable cellular imaging technology opens numerous avenues of research in the fields of cellular therapy, inflammation, and cancer research.

6.1.1 Chapter 2 & 3 – Development of Pre-clinical ^{19}F-MRI and Tracking the Fate of Stem Cell Implants

In Chapters 2&3, pre-clinical techniques were developed for imaging and quantifying MSC. Imaging data was supported by histology and immunohistochemistry. We were the first to show accurate quantification with bSSFP and to describe techniques for avoiding isoflurane background signal. The main findings were:

1) bSSFP allows for accurate quantification of cell pellets and confirmation of administered cell dose on the day of transplant
2) ^{19}F-MRI can be used to identify differences in stem cell fate over time between transplant models. *In vivo* quantification of the ^{19}F-signal displayed clearance of the

mMSCs in the two weeks following administration in the isograft model. In the immune-compromised xenograft, signal persisted over this same time period.

3) When the natural immune system clearance is inhibited, such as in immune-compromised mice, bystander labeling of macrophages can confuse longitudinal image interpretation.

These findings demonstrate the versatility of ^{19}F-MRI for tracking cells. The techniques developed and lessons learned in this project directly influenced our imaging protocols in subsequent studies. In particular, the improvements to quantification accuracy and avoiding isoflurane signal represent significant development milestones. Finally, the technique was applied to assess the differences in stem cell fate between transplant models. Here we were able to longitudinally image changes in the number of stem cells remaining at the site of implantation. However, assessing the infiltration of immune cells to the implant site still required the use of *ex vivo* immunohistochemistry; tracking this occurrence was the primary goal of the next study.

6.1.2 Chapter 4 – Application of Dual ^{19}F- and Iron-cellular MRI Agents to Track the Infiltration of Immune Cells to the Site of a Rejected Stem Cell Transplant

In chapter 4, we built on our pre-clinical imaging by demonstrating that ^{19}F-MRI can be combined with iron oxide cell tracking techniques to provide additional information on the rejection of stem cell transplants. We were the first to combine stem cells labeled with ^{19}F *in vitro* with intravenous labeling of phagocytic immune cells *in situ*. The main findings were:

1) Following injection of IV SPIO, signal from the ^{19}F labeled stem cells dropped significantly due to iron oxide induced signal quenching. The ^{19}F-signal did not change from this point until endpoint on day 14.
2) The signal void region, indicating the presence of inflammatory cells, extended beyond the site of the stem cell transplant itself. No signal void was observed in the opposite limb which had not received a stem cell transplant, or in mice which only received a saline sham injection.

3) Following in situ labeling of immune cells with ^{19}F, no significant change in signal was observed over the 14 days. This suggests there is no change in the number of immune cells present at the transplant site following the initial influx.

These findings implement a new method for combining cellular MRI techniques to obtain additional *in vivo* information. The significant decrease in both ^{19}F and ^{1}H signal resulting from the influx of SPIO labeled immune cells provides a method to track rejection and could be used as an early indicator of graft failure, without having to wait for symptomatic analysis. Overall, this study highlights the exciting potential of combining cellular MRI techniques to advance pre-clinical research.

6.1.3 Chapter 5 – Development of a Clinical Protocol for Imaging ^{19}F-labeled PBMC

In Chapter 5, we focused on translating our knowledge of ^{19}F-MRI from the high-field, pre-clinical 9.4T MRI to a clinical 3T system. In this study, we report the first time a ^{19}F clinical cell tracking protocol has been developed for a General Electric MRI system. This is the first report of imaging the heterogeneous PBMC mixture with ^{19}F-MRI. In addition, we present the best detection sensitivity for a clinical protocol currently reported in the literature and the first time cells were detected at greater than 1cm depth in a clinical phantom. The main findings were:

1) PBMC could be imaged following administration into a ham shank with a dual-tuned surface coil and 30minute clinical protocol. Total imaging time for this protocol was kept under 30minutes for patient comfort; including patient positioning, localizers, anatomical ^{1}H, and ^{19}F scans.
2) A detection limit of 3.8×10^{17} ^{19}F atoms was measured, representing approximately 4.5×10^{6} PBMC. This is an order of magnitude higher sensitivity than previous studies had reported. In addition, cells could be detected following a surface intradermal injection, and at 1cm depth with a subcutaneous injection.
3) Intracellular uptake of the ^{19}F agent was highly variable between patients, representing more than an order of magnitude of difference in minimum number of detectable cells. Based upon these results, in the development stage of clinical ^{19}F-

MRI, it may be necessary to pre-screen patients on a basis of intracellular loading prior to study enrollment.

These findings highlight the potential for clinical application of ^{19}F-MRI cell tracking. The minimum detection limit of $4.5\text{x}10^6$ PBMC is well above clinical doses applied with sipuleucel-T therapy. In addition, by using a very small surface coil and sacrificing imaging depth we were able to improve detection sensitivity by an order of magnitude,[1] and by more than two orders over the first study published in 2014.[2] Overall this work lays the foundation necessary for approval of a ^{19}F clinical trial at Robarts Research Institute.

6.2 Limitations

Loss of Intracellular Label

Cellular ^{19}F-MRI of pre-labeled cells is limited by the inability to longitudinally determine the number of live cells, when and if bystander labeling has occurred, and the low sensitivity. From just the images, it is impossible to determine what percentage of signal is produced by viable, ^{19}F-labeled therapeutic cells. Correlating ^{19}F-signal with that produced by bioluminescence imaging (BLI) could be used to address this limitation. BLI detects ATP producing cells, expressing the luciferase gene. Signal is theoretically quantitative, but severely attenuated with tissue depth. For discerning bystander labeling, a more successful approach may lie in the combination of cellular MRI techniques, as shown by Dr. Hitchens and discussed in chapter 4.[3] It is interesting to note that in certain circumstances ^{19}F-MRI provides some advantage over SPIO when considering bystander labeling. Due to the lower sensitivity, significantly more bystander labeling is necessary at a given site before false-positive signal is detected.[4] But due to this decreased sensitivity the detection of therapeutic ^{19}F-labeled cells can be missed if they do not reach the detection threshold. This is of concern with partial volume effects where a low number of cells is separated further by different voxels.

In vivo Quantification

A large number of assumptions are made when quantifying ^{19}F-labeled cells *in vivo*. Prior to cell administration, we assume the re-suspended cells are homogeneously distributed. If the cells are not perfectly homogenous, this influences the number of cells injected, and more importantly, the number of cells set aside for NMR. Since quantification is reliant on the accuracy of the intracellular ^{19}F uptake measurement, this is a significant potential source of error. In the images, regions of interest are selected by the user by eye and quantification is performed on hand-drawn ROIs. Determination of the boundary outlining noise from signal is often not concrete, and different ROI's may be drawn by users of differing experience. Finally, quantification assumes the signal at the ROI is comparable to the signal at the reference tube to determine the number of ^{19}F atoms present. This is influenced by the different relaxation rates due to environment from the agar reference tube and the *in vivo*, intracellular agent. In addition, any changes in B_1 field homogeneity would introduce additional quantification error as ^{19}F atoms experience different flip angles. Based upon our observations, we would approximate the error from bSSFP ^{19}F quantification on any individual scan to be +/- 15%. With repeated imaging, this value has been found to converge to the expected quantification number.

Quantification of ^{19}F signal is further hindered in the presence of iron oxide, and at only "apparent" cell number can be measured due to the drastic differences in relaxation. With the bSSFP sequence, SPIO quenches both ^{1}H and ^{19}F. The degree of quenching is difficult to determine due to the complexity of the sequence. Dr. Hitchens has shown that application of a UTE sequence can be used to generate a ^{19}F image even in the presence of iron oxide.[3] However, it is not clear how the accuracy of quantification would be affected in this case.

Clinical Protocol Optimization

Finally, the clinical protocol was optimized in a cadaverous ham shank. Although similar in appearance to a human thigh in ^{1}H images, there are distinct differences between the physiology of the two. First, the skin of the ham is significantly thicker and tougher than that of a human. This may assist in holding the injected cells in a tighter pellet following interdermal injection. The lack of functioning immune system and active blood supply would also hinder the movement and clearance of PBMC. In a clinical case, it may be expected that PBMC have higher potential to disperse and migrate away from the site in the time between injection and imaging.

6.3 Future Work

Future work will focus on applying the imaging techniques developed within this thesis to pre-clinical models of disease and to the first ^{19}F-cell tracking clinical trial in Canada.

6.3.1 Application of ^{19}F-MRI to Pre-clinical Disease Models

This thesis focused on developing a ^{19}F-site and techniques for application in a variety of disease models. One such model is in correlating the presence and number of tumour associated macrophages (TAMs) with tumourgenicity. TAMs have been shown to promote metastasis and immune tolerance.[5] Building on the techniques introduced in this thesis, Ashley Makela (PhD Candidate) from Dr. Foster's lab has shown ^{19}F-MRI provides superior information over SPIO for visualizing TAMs *in vivo.* The ^{19}F-agent is administered intravenously and labels phagocytic macrophages *in situ.* Information such as the relative number of TAMs and spatial distribution throughout the tumour can be compared with this technique.

Investigating the factors involved with the migration of labeled APCs is also a promising direction for ^{19}F-MRI. Future work could explore the application of antigen-loaded APC on a tumour bearing animal. When combined with ^{19}F-MRI, the therapeutic effects could be correlated with the number of ^{19}F-labeled APCs which arrive at the draining LN. Anti-cancer treatment effects could be further optimized by adjusting the route of delivery, dosage, APC cell-type, and pre-labeling strategies. The PBMC work is being led by Corby Fink (PhD Candidate) and the DC work by Michael Smith (MSc Candidate) in Dr. Dekaban's lab.

6.3.2 Two-colour ^{19}F-MRI for Imaging Transplant Rejection

In chapter 4, the largest limitation introduced by application of iron and ^{19}F cellular MRI was the inability to quantify either the stem cell transplant or the resulting inflammation due to the negative iron contast. However, by using two spectrally different ^{19}F-agents, inflammation signal could be differentiated from stem cell signal. This would provide a significant advantage over the current technique since it would allow both processes to be quantified over time. An addition advantage could be found from the combination of two

^{19}F agents and a SPIO agent, which would allow for three distinct cell populations to be tracked simultaneously. In combination with the new imaging technology, Magnetic Particle Imaging (MPI), all three of these cell populations can be spatial located and quantified.[6]

6.3.3 Phase-I Clinical Trial Investigating Safety and Tolerability of ^{19}F-labeled Human PBMC

With the establishment of a sufficiently sensitive clinical protocol, the next step is to run a Phase I clinical trial will focus on the safety and tolerability of ^{19}F-labeled PBMC. The trial (ClinicalTrials.gov identifier: NCT02921373) is set to enroll 6 healthy and 6 prostate cancer volunteers. Autologous PBMC will be collected, separated, and labeled with ^{19}F under Good Manufacturing Practice (GMP) conditions necessary for human administration. Secondary outcomes of the trial will be to further optimize detection of the injection site, and determine if LN signal can be observed in any volunteers. The trial will be overseen by Health Canada and Western University Ethics committee.

6.4 References

1. Rose L, Kadayakkara DKK, Wang G, Bar-Shir A, Helfer BM, O'Hanlon CF, Kraitchman DL, Rodriguez RL, Bulte JWM. Fluorine-19 Labeling of Stromal Vascular Fraction Cells for Clinical Imaging Applications. Stem Cells translational medicine. 2015:1–8.

2. Ahrens ET, Helfer BM, O'Hanlon CF, Schirda C. Clinical cell therapy imaging using a perfluorocarbon tracer and fluorine-19 MRI. Magnetic Resonance in Medicine. 2014;0:n/a-n/a.

3. Hitchens TK, Liu L, Foley LM, Simplaceanu V, Ahrens ET, Ho C. Combining Perfluorocarbon and Superparamagnetic Iron-Oxide Cell Labeling for Improved and Expanded Applications of Cellular MRI. Magnetic Resonance in Medicine. 2015;73(1):367–375.

4. Ribot EJ, Gaudet JM, Chen Y, Gilbert KM, Foster PJ. In vivo MR detection of fluorine-labeled human MSC using the bSSFP sequence. International journal of

nanomedicine. 2014;9:1731–9.

5. Lewis CE, Pollard JW. Distinct role of macrophages in different tumor microenvironments. Cancer research. 2006;66(2):605–12.

6. Zheng B, Vazin T, Goodwill PW, Conway A, Verma A, Ulku Saritas E, Schaffer D, Conolly SM. Magnetic Particle Imaging tracks the long-term fate of in vivo neural cell implants with high image contrast. Scientific Reports. 2015;5(August):14055.

Appendices

Appendix A: Permissions

Copyright for the following articles are held by the authors:

MS Fox, JM Gaudet and PJ Foster (2015) *Fluorine-19 MRI Contrast Agents for Cell Tracking and Lung Imaging* published in Magnetic Resonance Insight. 8(S1):1-15.

JM Gaudet, A Hamilton, Y Chen, MS Fox, and PJ Foster (2016) *Application of dual* ^{19}*F and iron cellular MRI agents to track the infiltration of immune cells to a site of a rejected stem cell transplant* published in Journal of Magnetic Resonance in Medicine, Early view.

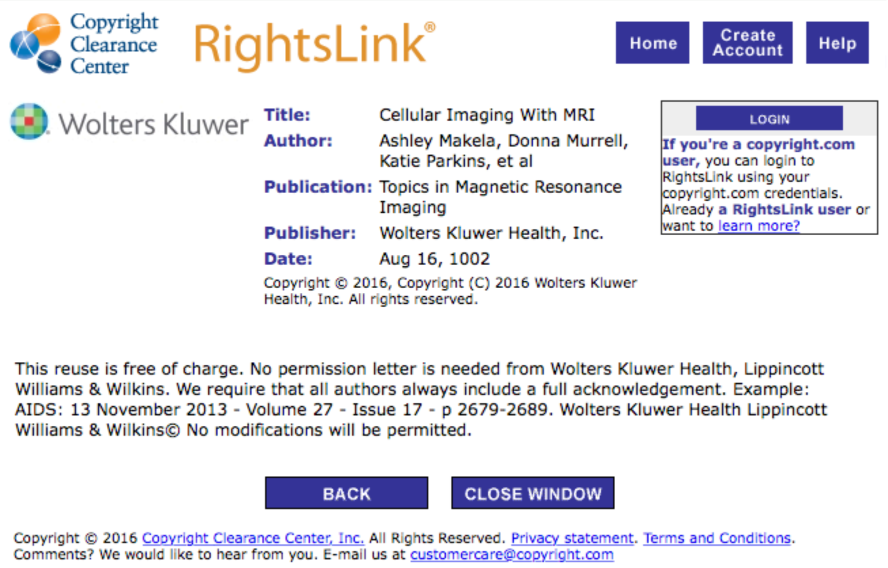

Title: Cellular Imaging With MRI
Author: Ashley Makela, Donna Murrell, Katie Parkins, et al
Publication: Topics in Magnetic Resonance Imaging
Publisher: Wolters Kluwer Health, Inc.
Date: Aug 16, 1002

Copyright © 2016, Copyright (C) 2016 Wolters Kluwer Health, Inc. All rights reserved.

If you're a copyright.com user, you can login to RightsLink using your copyright.com credentials. Already **a RightsLink user** or want to learn more?

This reuse is free of charge. No permission letter is needed from Wolters Kluwer Health, Lippincott Williams & Wilkins. We require that all authors always include a full acknowledgement. Example: AIDS: 13 November 2013 - Volume 27 - Issue 17 - p 2679-2689. Wolters Kluwer Health Lippincott Williams & Wilkins© No modifications will be permitted.

Copyright © 2016 Copyright Clearance Center, Inc. All Rights Reserved. Privacy statement. Terms and Conditions.
Comments? We would like to hear from you. E-mail us at customercare@copyright.com

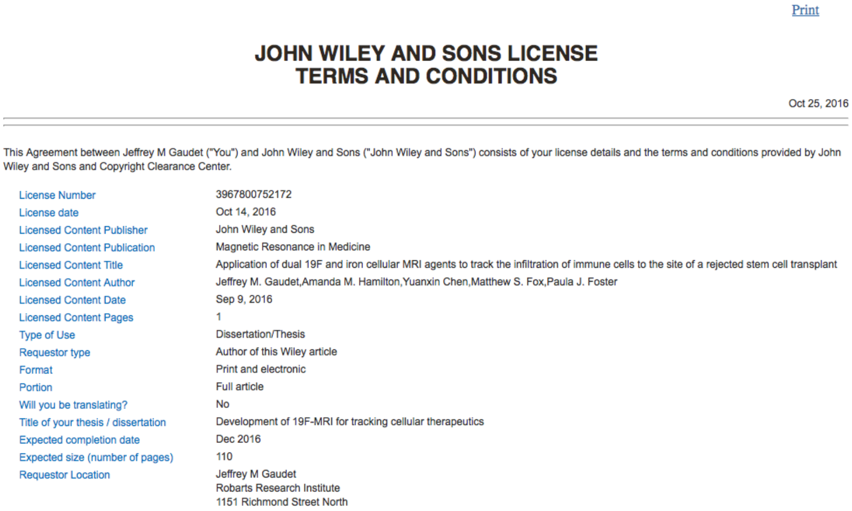

JOHN WILEY AND SONS LICENSE
TERMS AND CONDITIONS

Oct 25, 2016

This Agreement between Jeffrey M Gaudet ("You") and John Wiley and Sons ("John Wiley and Sons") consists of your license details and the terms and conditions provided by John Wiley and Sons and Copyright Clearance Center.

License Number	3967800752172
License date	Oct 14, 2016
Licensed Content Publisher	John Wiley and Sons
Licensed Content Publication	Magnetic Resonance in Medicine
Licensed Content Title	Application of dual 19F and iron cellular MRI agents to track the infiltration of immune cells to the site of a rejected stem cell transplant
Licensed Content Author	Jeffrey M. Gaudet,Amanda M. Hamilton,Yuanxin Chen,Matthew S. Fox,Paula J. Foster
Licensed Content Date	Sep 9, 2016
Licensed Content Pages	1
Type of Use	Dissertation/Thesis
Requestor type	Author of this Wiley article
Format	Print and electronic
Portion	Full article
Will you be translating?	No
Title of your thesis / dissertation	Development of 19F-MRI for tracking cellular therapeutics
Expected completion date	Dec 2016
Expected size (number of pages)	110
Requestor Location	Jeffrey M Gaudet Robarts Research Institute 1151 Richmond Street North

Appendix B: Curriculum Vitae

Name:	Jeffrey M. Gaudet
Post-secondary Education and Degrees:	University of Guelph Guelph, Ontario, Canada 2008-2012 B.Sc. Honours Biophysics
	The University of Western Ontario London, Ontario, Canada 2012-Current, Ph.D. Medical Biophysics and Molecular Imaging
Honours and Awards:	Graduate Studentship in Prostate Cancer Research Prostate Cancer Canada 2015, $40,000
	Dean's Stipend Schulich School of Medicine and Dentistry Sept. 2014 – Aug 2017, $5000/yr
	Cancer Research and Technology Transfer Studentship CIHR Strategic Training Program Sept. 2013 – Aug. 2015, $25,600/yr
	Ontario Graduate Studentship Sept. 2013 – Aug 2014, $15,000/yr
Related Work Experience	Teaching Assistant – Digital Imaging The University of Western Ontario 2016

Publications:

Fink C., **Gaudet J.M.,** Fox M.S., Bhatt S, Viswanathan S, Smith M, Chin J, Foster P.J., and Dekaban G.A. “19F-perfluorocarbon- labeled human peripheral blood mononuclear cells can be detected in vivo using clinical MRI parameters in a therapeutic setting” Submitted to: *PLoS One* on Sept. 16, 2016.

Makela A.*, **Gaudet J.M.**, Foster P.J. “Quantifying tumor assosciated macrophages in breast cancer: a comparison of iron and fluorine-based MRI cell tracking”. Submitted to Scientific Reports on Sept. 14 2016.

Gaudet J.M.*, Hamilton A., Fox M.S., Chen Y. and Foster P.J. "Combining cellular MRI approaches to simultaneously evaluate stem cell survival and immune cell infiltration" *Journal of Magnetic Resonance in Medicine* Early Access. doi: 10.1002/mrm.26400. Published: September 9, 2016

Makela A.*, Murrell D.*, Parkins K., Kara J., **Gaudet J.M.,** Foster P.J. "Cellular Imaging with MRI" *Topics in Magnetic Resonance*. 25(5): 177-186. doi:10.1097/RMR.0000000000000101. Published: June 29, 2016

Fox M.S.*, **Gaudet J.M.**, and Foster P.J. "Fluorine-19 MRI Contrast Agents for Cell Tracking and Lung Imaging." *Magnetic Resonance Insights* 8.Suppl 1 (2015): 53. Published: March 22, 2016

Scheid E.*, Major P., Bergeron A., Finn O.J., Salter R.D., Eady R., Yassine-Diab B., Favre D., Peretz Y., Landry C., Hotte S., Mukherjee S., Dekaban G.A., Fink C., Foster P.J., **Gaudet J.M.**, Gariepy J., Sekaly R., Lacombe L., Fradet Y., and Foley R. "Tn-MUC1 Dendritic Cell Vaccination: A Preclinical Study in Rhesus Macaques and Phase I/II Trial in Castrate Resistant Non-Metastatic Prostate Cancer Patients." *Cancer Immunology Research.* Accepted on June 12, 2016

Gaudet J.M.*, Ribot E.J., Chen Y., Gilbert K., and Foster P.J. "Mesenchymal stem cell transplant rejection monitored with ^{19}F-MRI.*" PLoS One*. 10(3): e0118544. doi: 10.1371/journal.pone.0118544. Published: March 13, 2015.

Ribot E.J.*, **Gaudet J.M.**, Chen Y., Gilbert K., and Foster P.J. "In vivo MR detection of fluorine-labeled human MSC using the bSSFP sequence''*. International Journal of Nanomedicine.* Published: April 24, 2014. Page 1731.

Oral Presentations: 5 (3 International)

- ISMRM 2015 - summa cum laude
- ImNO 2016 – summa cum laude
- ISMRM 2016 – summa cum laude

Poster Presentations: 12 (1 International)